SANDIA REPORT

SAND2013-10525
Unlimited Release
Printed September 2013

Enabling Secure, Scalable Microgrids with High Penetration Renewables

Oleg Wasynczuk, Lee Rashkin, Steven Pekarek

Prepared by
Sandia National Laboratories
Albuquerque, New Mexico 87185 and Livermore, California 94550

Sandia National Laboratories is a multi-program laboratory managed and operated by Sandia Corporation, a wholly owned subsidiary of Lockheed Martin Corporation, for the U.S. Department of Energy's National Nuclear Security Administration under contract DE-AC04-94AL85000.

Sandia National Laboratories

Issued by Sandia National Laboratories, operated for the United States Department of Energy by Sandia Corporation.

Printed in the United States of America. This report has been reproduced directly from the best available copy.

Available to DOE and DOE contractors from
U.S. Department of Energy
Office of Scientific and Technical Information
P.O. Box 62
Oak Ridge, TN 37831

Telephone:	(865) 576-8401
Facsimile:	(865) 576-5728
E-Mail:	reports@osti.gov
Online ordering:	http://www.osti.gov/scitech

Available to the public from
U.S. Department of Commerce
National Technical Information Service
5301 Shawnee Rd
Alexandria, VA 22312

Telephone:	(800) 553-6847
Facsimile:	(703) 605-6900
E-Mail:	orders@ntis.gov
Online order:	http://www.ntis.gov/search

SAND2013-10525
Unlimited Release
Printed September 2013

Enabling Secure, Scalable Microgrids with High Penetration Renewables

Oleg Wasynczuk
Lee Rashkin
Steven Pekarek

Department Names
Sandia National Laboratories
P.O. Box 5800
Albuquerque, New Mexico 87185

School of Electrical and Computer Engineering
Purdue University
West Lafayette, IN 47907

Under

Sandia Contract Agreement 1067259

September 2013

Final Report

Enabling Secure, Scalable Microgrids with High Penetration Renewables

Prepared by

Oleg Wasynczuk
Lee Rashkin
Steven Pekarek

School of Electrical and Computer Engineering
Purdue University
West Lafayette, IN 47907

Under

Sandia Contract Agreement 1067259

September 2013

TABLE OF CONTENTS

1 COMPARISON OF AC AND DC TECHNOLOGIES

In this section, ac and dc technologies are compared highlighting their advantages and disadvantages. Since ac and dc systems have both evolved significantly since their introduction in the mid and latter parts of the 19^{th} century, many of the early advantages of ac systems no longer exist or are of less importance today. Consequently, it is useful to provide a brief historical perspective on the evolution of both ac and dc power systems.

1.1 Early Comparison of Dc and Ac

The dc generator, or dynamo, was originally developed in the early part of the 19^{th} century and refined to the point of commercial viability in the later part of the 19^{th} century. A perspective view and an equivalent circuit of an early dynamo are shown in Figure 1-1. The stationary member or stator includes a field winding in which a dc current is injected that produces a stationary magnetic field. The rotating member or rotor consists of a cylindrically shaped magnetic material around which a number of coils are wound so as to produce currents that flow in the axial direction around the peripheral surface. As each coil rotates relative to a stationary field, a voltage is induced due to Faraday's law. The voltages induced in the rotor coils are ac; however, the terminals of each coil are connected to rotating copper segments that are a part of the commutator located at one end of the rotor. A pair of stationary graphite brushes connects the output terminals of the generator to the appropriate commutator segments. As the rotor rotates, the output terminals are connected to different segments (coils). The net effect of the commutator-brush arrangement is the rectification and addition of the individual coil voltages to form a relatively constant dc output voltage as shown in Figure 1-2.

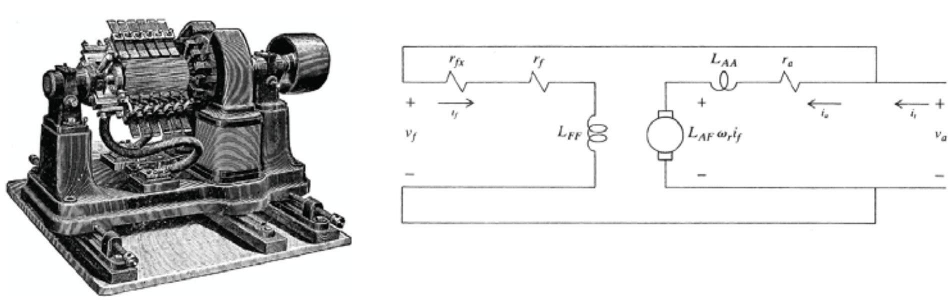

Figure 1-1 Early dc generator (dynamo) and its equivalent circuit.

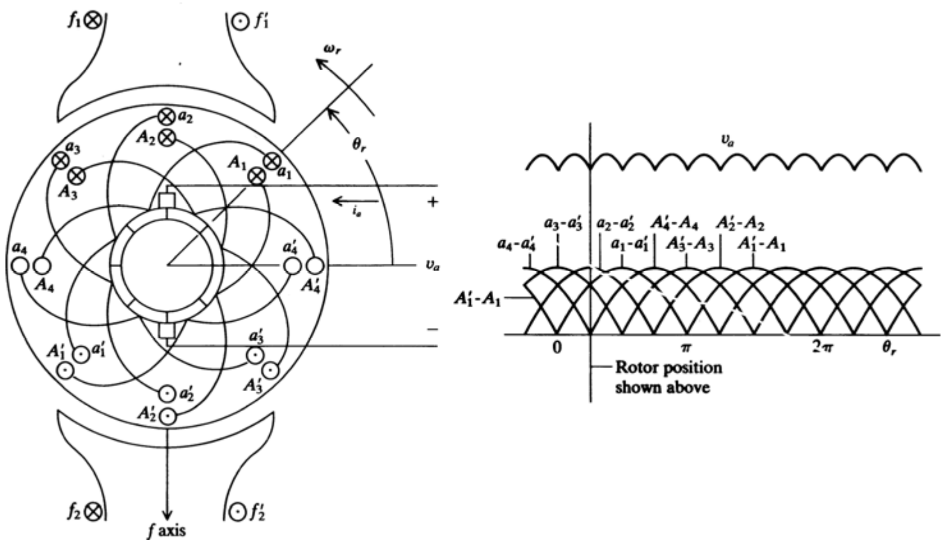

Figure 1-2 Output voltage of dc generator.

The equivalent circuit of a dc generator is shown in the right-hand side of Figure 1-1. The field winding is shown as a resistor and inductor, r_f and L_{FF}, respectively. An adjustable external resistor (rheostat) is used to control the field current. The output or armature circuit is shown on the right-hand side of the circuit. The induced voltage is proportional to the field current and rotor speed. A small armature resistance and inductance, r_a and L_{AA}, is included in the equivalent circuit to represent the coil resistances and leakage inductance. In a shunt-connected dc generator, the field winding is connected through the rheostat to the output terminals, and the rheostat is used to adjust the field current and hence output voltage.

The first power system in the US was a dc system built by T. A. Edison in 1882, known as the Pearl Street Station in New York City. Initially, there was one dc generator serving 400 lamps for 85 customers. By 1884, the Pearl Street Station served 508 customers with 10,164 lamps. The Pearl Street Station did not last very long burning down in 1890.

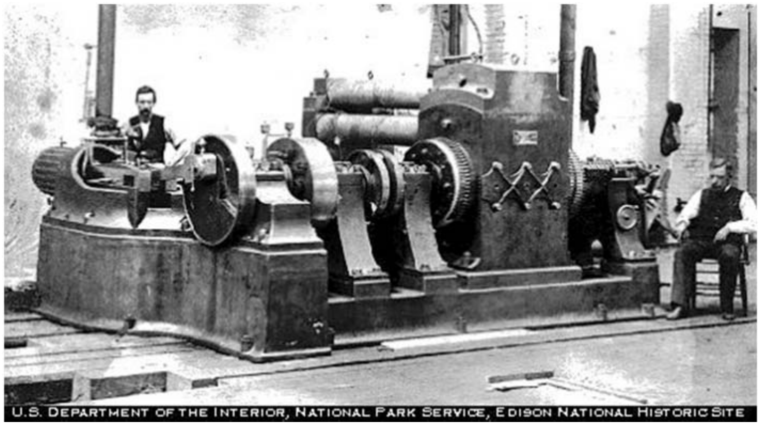

Figure 1-3 Pearl Street generating station (110-V dc).

A major disadvantage of early dc generation was that the current due to an electrical fault is limited primarily by the armature resistance r_a, which is made as small as possible to reduce steady-state losses during normal operating conditions. Therefore, the fault current may be very large (several orders of magnitude greater than rated current). This is problematic due to the large forces produced in the generator as well as in the design of protective devices (circuit breakers) needed to clear the fault in order to prevent equipment damage and/or fires.

A second disadvantage of early dc generation was that it was not practical in Edison's time to directly convert 110-V dc to a larger value for transmission over longer distances. By redesigning the original generators, Edison later increased the voltage generated at the Pearl Street Station to 220 V to reduce the amount of copper needed to transmit power underground to customers; however, at these relatively low voltages, the generating plant still had to be in close proximity to the point of consumption.

A third disadvantage of early dc generation was the fact that dc generators could not be connected in parallel since even a small difference in generated voltage would cause one generator to assume all of the load current while the other generator coasted. Last but not least, the motorized field rheostat and large field time constant resulted in a very slow control of the output dc voltage.

At about the same time that Edison built the Pearl Street Station, ac generators were developed leading to the first ac power system shown in Figure 1-4. The system was comprised of a 100-HP Westinghouse alternator that produced a single-phase 133-Hertz ac voltage at 3000 volts. The generator was driven by a six-foot Pelton wheel under a 320-foot head and provided ac electricity that was transmitted 2.6 miles to a motor-driven stamp mill. At about the same time, Nikola Tesla had proposed polyphase ac for producing rotating magnetic fields leading to improved ac generators and motors including the induction motor.

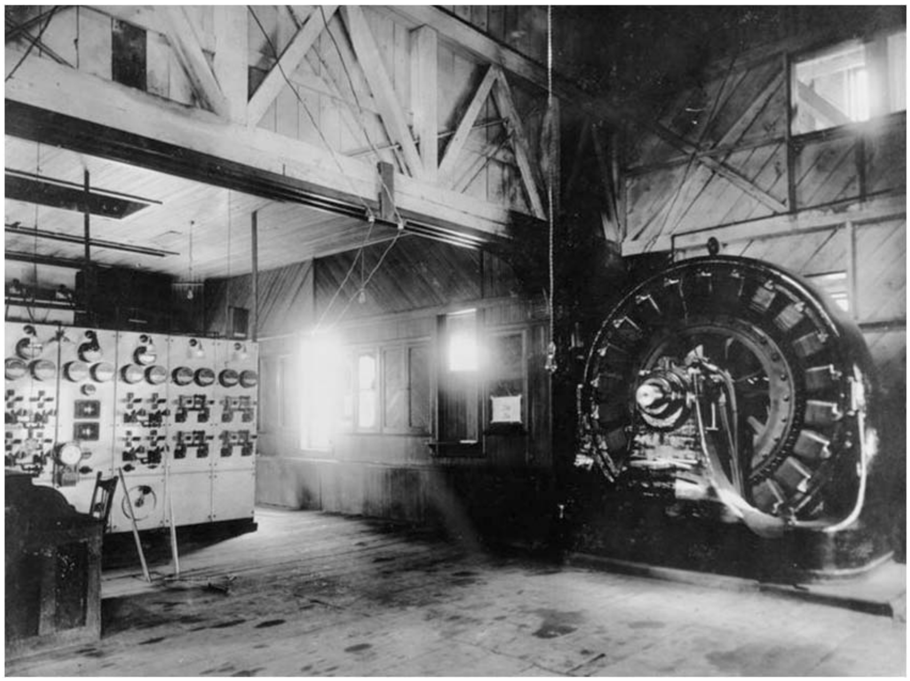

Figure 1-4 The Ames Hydroelectric Generating Plant near Ophir, Colorado (first ac power system in U.S.). 100 horsepower (75 kW) Westinghouse alternator was the largest then manufactured, generating electricity at 3000 volts, 133 Hertz, single-phase AC.

Early ac systems did not have any of the aforementioned disadvantages of dc. For example, fault currents of ac generators were (and continue to be) much smaller than those of conventional dc generators since they are limited by the subtransient, transient, or steady-state armature reactances (depending upon the time frame of interest) associated with ac generators. The steady-state fault current is typically only a few times larger than the maximum steady-state current. Moreover, whereas a reactance limits the magnitude of the fault current, it does not contribute to real losses, as does a dc resistance. Additionally, it became possible to connect ac generators in parallel since small differences in the armature reactances of paralleled ac generators does not give rise to a large difference in the current produced by each generator.

Another significant advantage of ac generation was the fact that it was possible to efficiently convert power from one ac voltage level to another using a transformer consisting primarily of copper wires and alloys of iron (magnetic steel) as shown in Figure 1-5 This allowed a significant reduction in the amount of material (copper or aluminum) needed to transmit power over long distances.

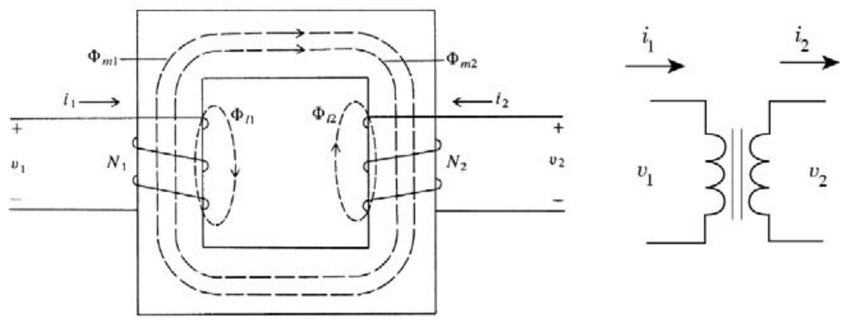

Figure 1-5 AC transformer and equivalent circuit.

Finally, an ac generator is somewhat simpler to construct since a dc voltage can be applied to the rotating field winding using a brush-slip-ring arrangement instead of the more complicated brush-commutator, i.e. the multi-segment commutator is replaced with a solid copper disc. All of the aforementioned disadvantages of dc and advantages of ac were essentially impossible for Edison to overcome during this time frame and as a result, Edison's General Electric Company soon began developing devices and components for ac power generation, distribution, and consumption.

1.2 The Reemergence of Dc

Although ac had clear and essentially insurmountable advantages over dc during the early evolutionary stages of electric power systems, subsequent developments in material science, solid-state physics, and control theory has led to new devices and approaches that has significantly altered the situation. Perhaps the most significant early contribution was the development of the mercury arc valve and its implementation in a circuit that enabled the efficient conversion of power from ac to dc and vice versa.

In a mercury arc valve, the electrodes are separated and, in its off state, the device is capable of blocking a very large voltage. However, if an arc is ignited using a low-voltage control electrode or gate, the arc produces a conductive path between the two main electrodes placing the valve in its 'on' state. If the current through the arc attempts to reverse direction, the arc is naturally extinguished causing the valve to return to its 'off' state. A photograph of an arc valve and a schematic illustrating its use in a high-voltage rectifier/inverter circuit are shown in Figure 1-6.

The first application of this technology was Asea's high voltage dc (HVDC) project in Gotland, Sweden, which in 1954 became the first modern fully commercial HVDC system. The project involved the transmission of 20 MW over a 98-km submarine cable between Västervik, Sweden and Ygne on the island of Gotland, with a voltage of 100 kV. The principal engineer was A. U. Lamm who became known as the father of HVDC. The mercury arc rectifier has since been replaced by the solid-state thyristor.

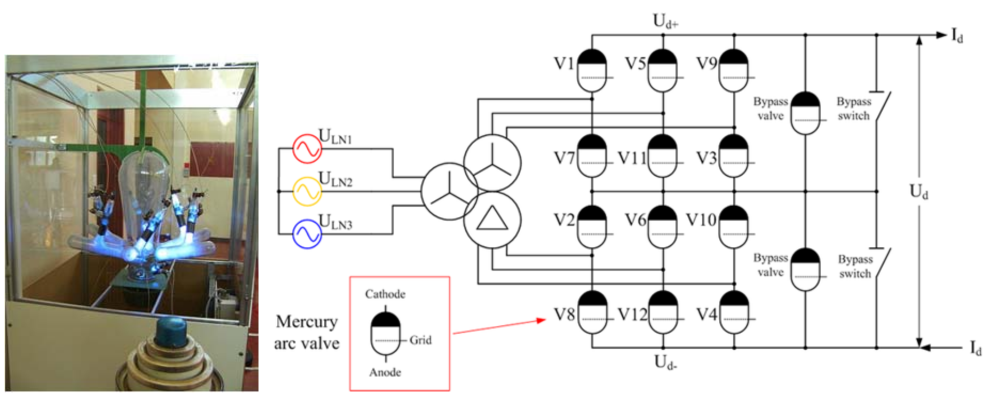

(a) (b)

Figure 1-6 (a) Mercury arc valve, (b) Arc valve rectifier circuit.

The rectifier/inverter permits the efficient conversion of power from ac to dc and vice versa. Moreover, the power flow can be rapidly and accurately controlled by delaying the triggering of the valves (arc or thyristor). The advantages of transmitting power using dc are described in the next section.

1.3 Comparison of Ac and Dc Transmission [1]

In this section, a three-wire ac line is compared to a two-wire dc line as shown in Figure 1-7. Therein, E_p is the ac phase-to-ground voltage (rms value), E_L is the ac line-to-line voltage (rms value), $V_d/2$ is the dc line-to-ground voltage and V_d is the dc line-to-line voltage. Also, I_L is the ac line current (rms value) and I_d is the dc current.

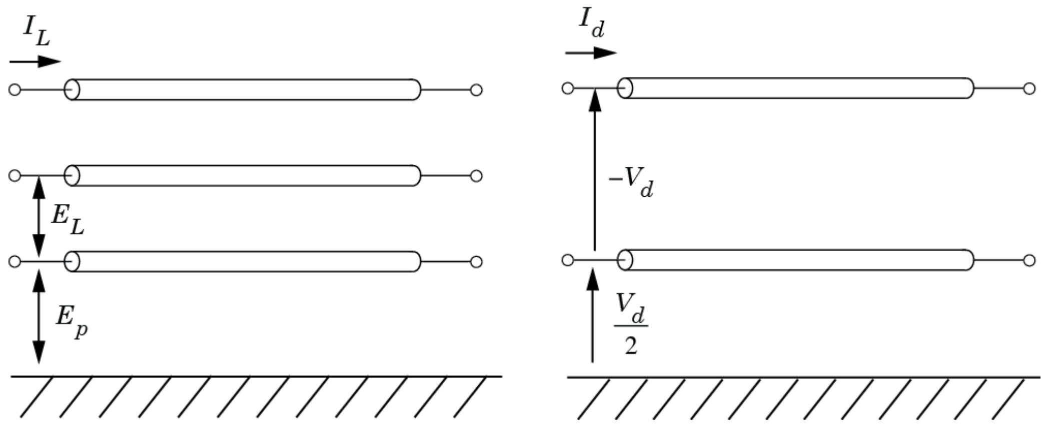

Figure 1-7 Ac and dc transmission lines.

In the initial comparison, equal conductor "temperatures" ($I_d = I_L$), resistances, and insulating levels $V_d/2 = \sqrt{2}E_p$ are assumed. That is the power losses in each conductor will be the same. The transmitted dc power may be expressed

$$P_{dc} = V_d I_d \tag{1.1}$$

The transmitted ac power may be expressed

$$P_{ac} = 3E_p I_L \cos\phi \tag{1.2}$$

where $\cos\phi$ is the power factor, which is typically somewhat less than unity. If the transmitted power is the same, $P_{dc} = P_{ac}$, then

$$\cos\phi = \frac{2\sqrt{2}}{3} \tag{1.3}$$

The total dc losses are $2I_d^2R$ while the total ac losses are $3I_L^2R$. Thus, dc losses will be 2/3 of the ac losses. Dc transmission is even more favorable if skin effect is considered (the ac resistance will be somewhat larger than the dc resistance given identical conductors).

In a second comparison, equal percent losses ($\text{dc losses}/P_{dc} = \text{ac losses}/P_{ac}$) and equal insulating levels $V_d/2 = \sqrt{2}E_p$ are assumed. Thus

$$\%\,\text{dc losses} = \frac{2I_d^2R}{V_dI_d} = \%\,\text{ac losses} = \frac{3I_L^2R}{3E_pI_L\cos\phi} \tag{1.4}$$

If $\cos\phi = \frac{2\sqrt{2}}{3}$ as before,

$$P_{dc} = \frac{3}{2}P_{ac} \tag{1.5}$$

In this comparison, the maximum dc power is 1.5 times the maximum ac power.

In order to illustrate the advantages of dc transmission graphically, three overhead lines are compared in Figure 1-8, all corresponding to a transmission capacity of 6000 MW. The ac voltages are given as line-to-line rms. It is clearly seen that dc transmission has significant advantages provided the cost of the ac-to-dc and dc-to-ac converters at the two ends of the line do not offset the saving in transmission line cost.

Figure 1-8 Comparison of right-of-way for ac and dc transmission.

Comparison with 3-wire single-phase ac

Low-power microgrids may be single-phase ac. Therefore, it is useful to compare three-wire single-phase ac with two-wire dc transmission as shown in Figure 1-9.

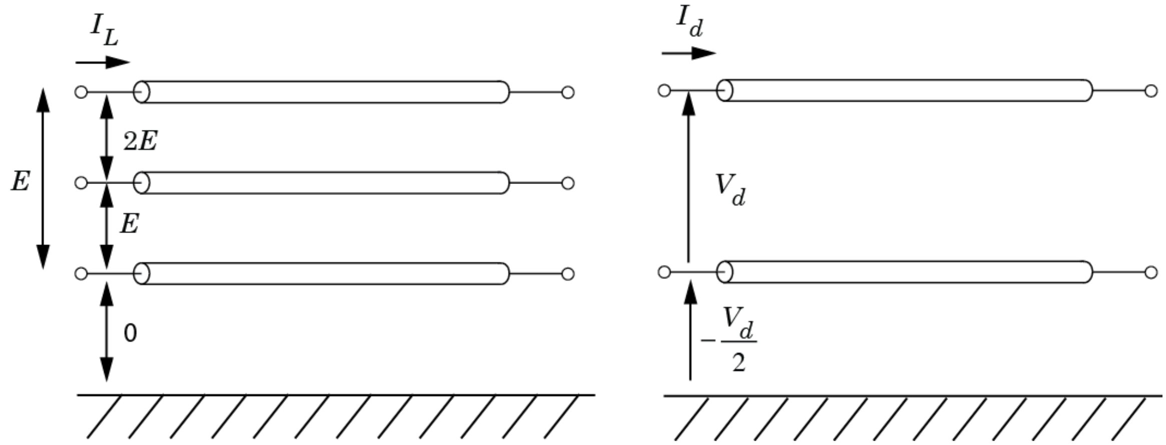

Figure 1-9 Three-wire single-phase ac versus two wire dc transmission.

Assuming equal insulating levels $\sqrt{2}E = V_d/2$ and conductor "temperatures" $I_d = I_L$, the ac and dc power may be expressed

$$P_{ac} = 2EI_L \tag{1.6}$$

$$P_{dc} = V_d I_d = 2\sqrt{2}EI_L \tag{1.7}$$

This, it is seen that the transmitted dc power P_{dc} is $\sqrt{2}$ larger with 2 conductors instead of 3.

Comparison with 2-wire single-phase ac

Finally, it is useful to compare the two-wire ac and two-wire dc transmission systems as shown in Figure 1-10.

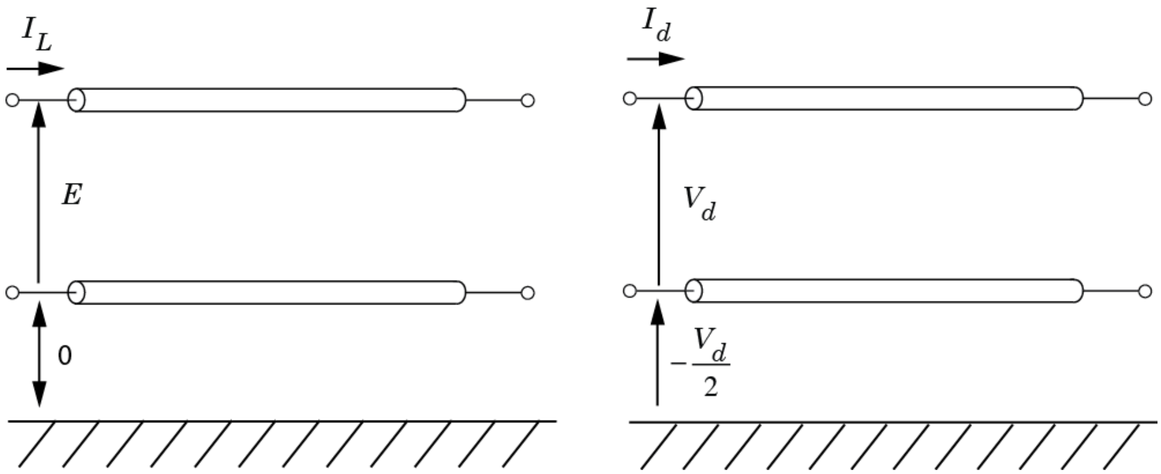

Figure 1-10 Two-wire ac and two-wire dc transmission.

Assuming equal insulating levels $\sqrt{2}E = V_d$ and conductor "temperatures" $I_d = I_L$

$$P_{ac} = EI_L \tag{1.8}$$

$$P_{dc} = V_d I_d = \sqrt{2}EI_L \tag{1.9}$$

In this case, the transmitted dc power P_{dc} is $\sqrt{2}$ (41%) larger.

In the previous analysis, only the thermal and insulation considerations were considered. However, in long ac lines, the power flow is not limited due to thermal constraints but to its reactance. In particular, if the resistance is neglected, the per unit power flow across a balanced three-phase transmission line may be expressed

$$P_{12} = \frac{V_1 V_2}{X}\sin\left(\theta_1 - \theta_2\right) \tag{1.10}$$

where V_1 and V_2 are the per unit voltage magnitudes at the two ends of the line, $\theta_1 - \theta_2$ is the phase angle difference between the voltage phasors, and X is the per unit positive-sequence series reactance of the ac line, assuming that the line is modeled using a pi-equivalent circuit (Appendix A). If the voltages at the two ends are regulated to 1 pu, the absolute maximum power flow is $1/X$; however, the phase angle is commonly limited to values less than approximately 45° for stability reasons. In any case, this maximum value may be significantly less than the thermal limit for high-voltage lines longer than approximately 50 miles. This result tilts the scale further in favor of dc transmission.

It may be noted that several approaches have been used to augment the power transfer capabilities of long ac transmission lines. These include shunt compensation [2] and series compensation [3]. In shunt compensation, a synchronous condenser or controllable capacitor bank (static VAR controller or SVC) is located approximately midway between the two terminals. The injected reactive power is used to regulate the voltage magnitude at the midpoint of the transmission line. If the midpoint voltage is regulated to 1 pu, the maximum power flow is effectively doubled since the reactance between either terminal and the midpoint is half of the total reactance. In series compensation, a capacitor bank is placed in series at either end of the line. Since capacitive reactance is negative, it cancels a part of the positive-sequence reactance of the transmission line, reducing the net reactance and hence increasing the maximum power transfer. However, the latter approach may produce a subsynchronous resonance (SSR) that interacts with the torsional modes of steam turbine generators. This interaction, if left unchecked, may result in turbine shaft failures [4]. Several methods of mitigating the effects of SSR have been developed [5] and [6]; however, these methods add substantial cost to the transmission line. Shunt compensation does not lead to SSR; however, in both series and shunt compensation, there is significant additional cost associated with the additional equipment required (SVC, series capacitors, SSR mitigation strategy) that could instead be diverted to the ac/dc and dc/ac converters connected at the two ends of an HVDC line.

In summary, if equal power transmission is assumed, dc transmission lines are significantly smaller and lighter, requiring less conductor material and, for high-voltage applications, requiring significantly less right-of-way and structural materials for the towers. Finally, if a long dc line interconnects two dc systems instead of two ac systems as assumed heretofore, the dc/dc converters at the two ends of the transmission line used to control the power flow contain fewer switches with correspondingly smaller losses than the ac/dc and dc/ac converters that would be required if the given line interconnects two ac systems. Indeed, modern power electronics has significantly altered the balance in favor of dc since Edison's first dc power system. In the next section, various aspects of modern dc microgrids are examined.

2 MODERN DC MICROGRIDS

With the advent of power electronics, modern dc components are significantly different in terms of construction, functionality, and dynamic performance than the counterparts that existed during Edison's era. For example, a prototypical dc source such as that used in diesel locomotives consists of an ac alternator connected to a diode bridge rectifier as shown in Figure 2-1. The output voltage is regulated by adjusting the current in the rotating field winding using an excitation system. The excitation system may be stationary with its output connecting to the field winding through a brush-slip-ring arrangement as shown in Figure 2-1, or rotating where the armature windings of a second "inverted" ac generator (stationary field, rotating armature) are connected through a rotating rectifier to the field winding of the main generator. Also shown in Figure 2-1 is an interface device (ID) that is described in more detail in a later section.

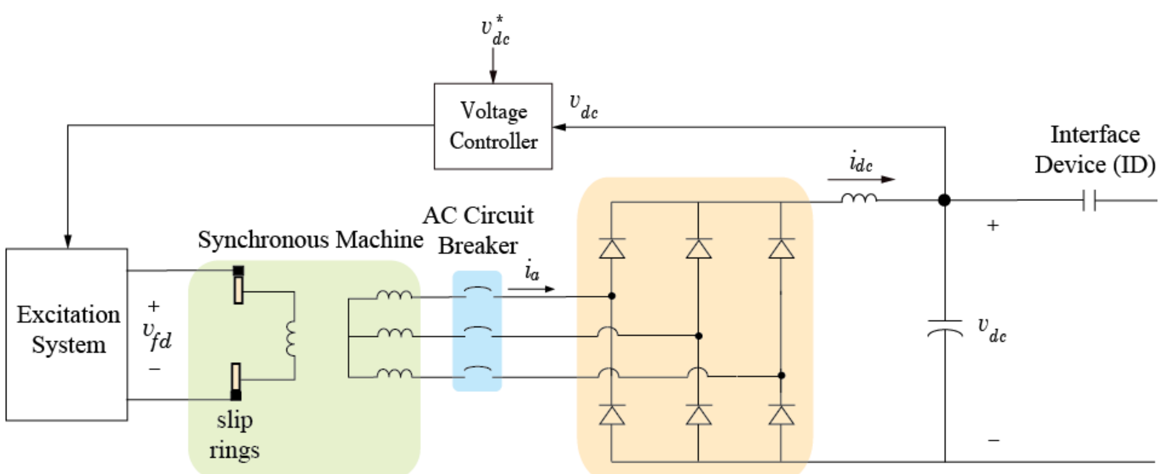

Figure 2-1 Rotating source with diode bridge rectifier.

Unlike the original dc dynamo, the dc source in Figure 2-1 will not exhibit the large fault currents associated with the original dynamo. Instead, the dc fault current is limited by the armature reactance of the ac generator (subtransient, transient or steady state, depending upon the time frame of interest). Moreover, a circuit breaker can be installed on the ac side of the rectifier to isolate the generator in the event of a fault on the dc bus. This eliminates two of the significant disadvantages of early dc generators.

Due to the relatively large time constant of the field winding of the main generator, the bandwidth of the voltage regulator is somewhat limited making it difficult to parallel two dc sources of the type shown in Figure 2-1. However, with the advent of thyristors and, more recently, insulated gate bipolar transistors (IGBTs), the passive diode bridge rectifier can be replaced with an IGBT-based active rectifier as shown in Figure 2-2 or a thyristor-based rectifier as shown in Figure 2-3. In both cases, the bandwidth of the voltage controller is significantly enhanced making it possible to more accurately and rapidly control the output voltage. Paralleling of such sources is readily achievable using, for example, droop based voltage regulation strategies as discussed in a later section.

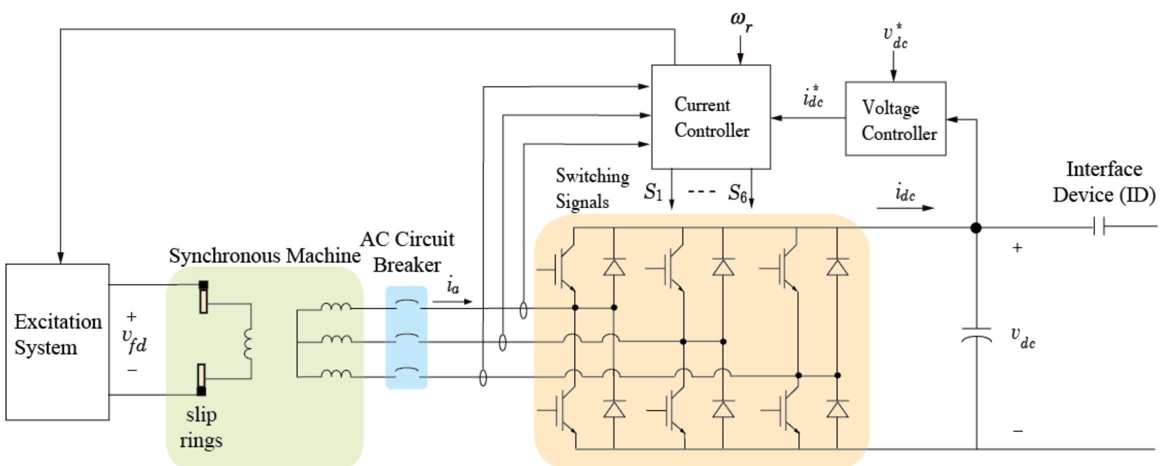

Figure 2-2 Rotating source with active rectifier.

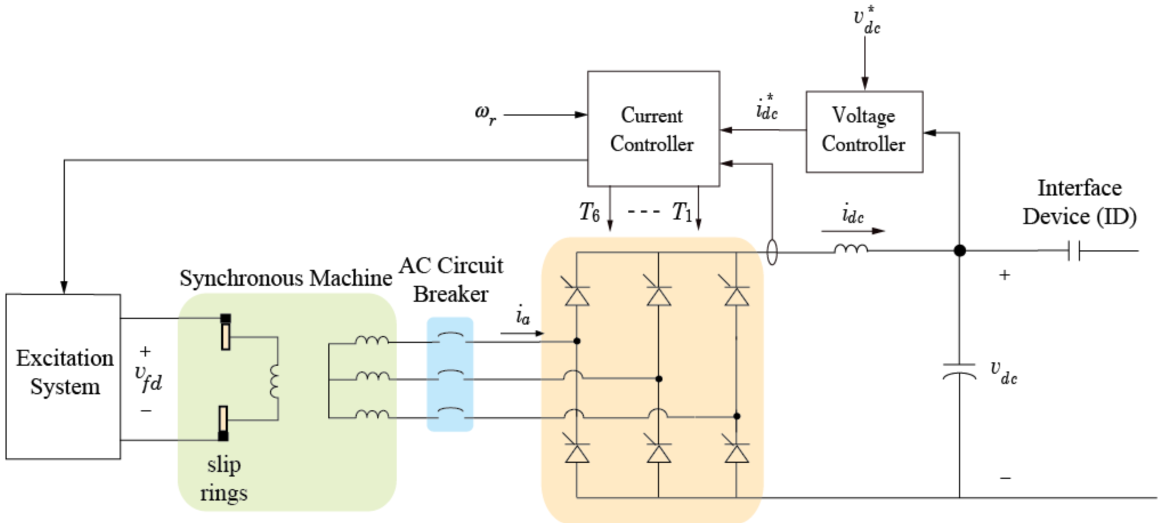

Figure 2-3 Rotating source with thyristor bridge rectifier.

Another prototypical dc source used in microgrid applications is the photovoltaic array connected to the dc bus through a buck/boost converter as shown in Figure 2-4. The voltage on the array side of the converter can be controlled using a simple pulse-width modulation control so as to extract optimal power from the array. If the dc bus is short circuited, the fault current is typically limited to no more than 20% of rated current by virtue of the self-limiting IV characteristics of the array.

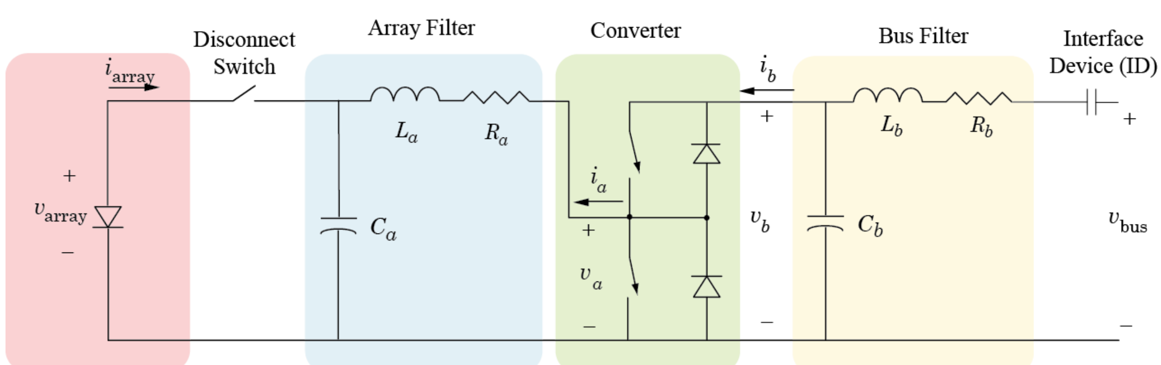

Figure 2-4 Non-isolated photovoltaic source with two-quadrant buck/boost converter.

Energy storage is an extremely important component in any microgrid since the available generation may not always be sufficient to meet load demand. A prototypical battery energy storage unit (BESU) is depicted in Figure 2-5 wherein a battery is connected to the dc bus through a bidirectional buck/boost converter. That is, the converter acts as a buck converter during charging and boost converter during discharging. In this case, a fault on the dc bus can give rise to very large fault currents (from the battery to the fault itself) due to the very low output impedance of the battery. These large fault currents are potentially very damaging to the battery, converter, and cables connected between the BESU and the fault. Therefore, it is imperative in this circuit configuration that a fast-acting fuse of appropriate current and voltage rating be connected as close as possible to the battery terminals.

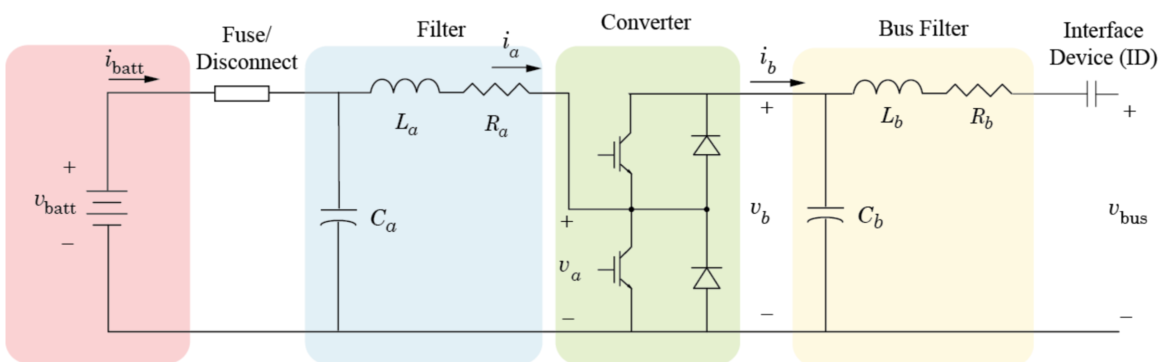

Figure 2-5 Prototypical battery energy storage unit (BESU).

Alternatively, if a dc-to-dc converter that includes an isolating transformer is used and the fault occurs on the bus side of the isolating transformer, a much smaller fault current will result with much less likelihood of damage to the battery. Moreover, a dc bus fault will not cause the battery fuse to open since a sustained fault on the dc bus will not propagate through the isolating transformer to affect the battery. A device failure on the battery side of the isolation transformer may still result in a large fault current and opening of the battery fuse, leading to a sustained loss of the BESU. However, the BESU should be able to fully recover from faults in other parts of the dc microgrid. Thus, the challenge of having to interrupt potentially very large fault currents in early dc systems no longer (or need not) apply to modern dc microgrids.

For purposes of example, a modern dc microgrid is depicted in Figure 2-6. Aspects to be considered include stability and control, protection, power quality, and power/energy management strategies. These aspects are described in the following sections.

•

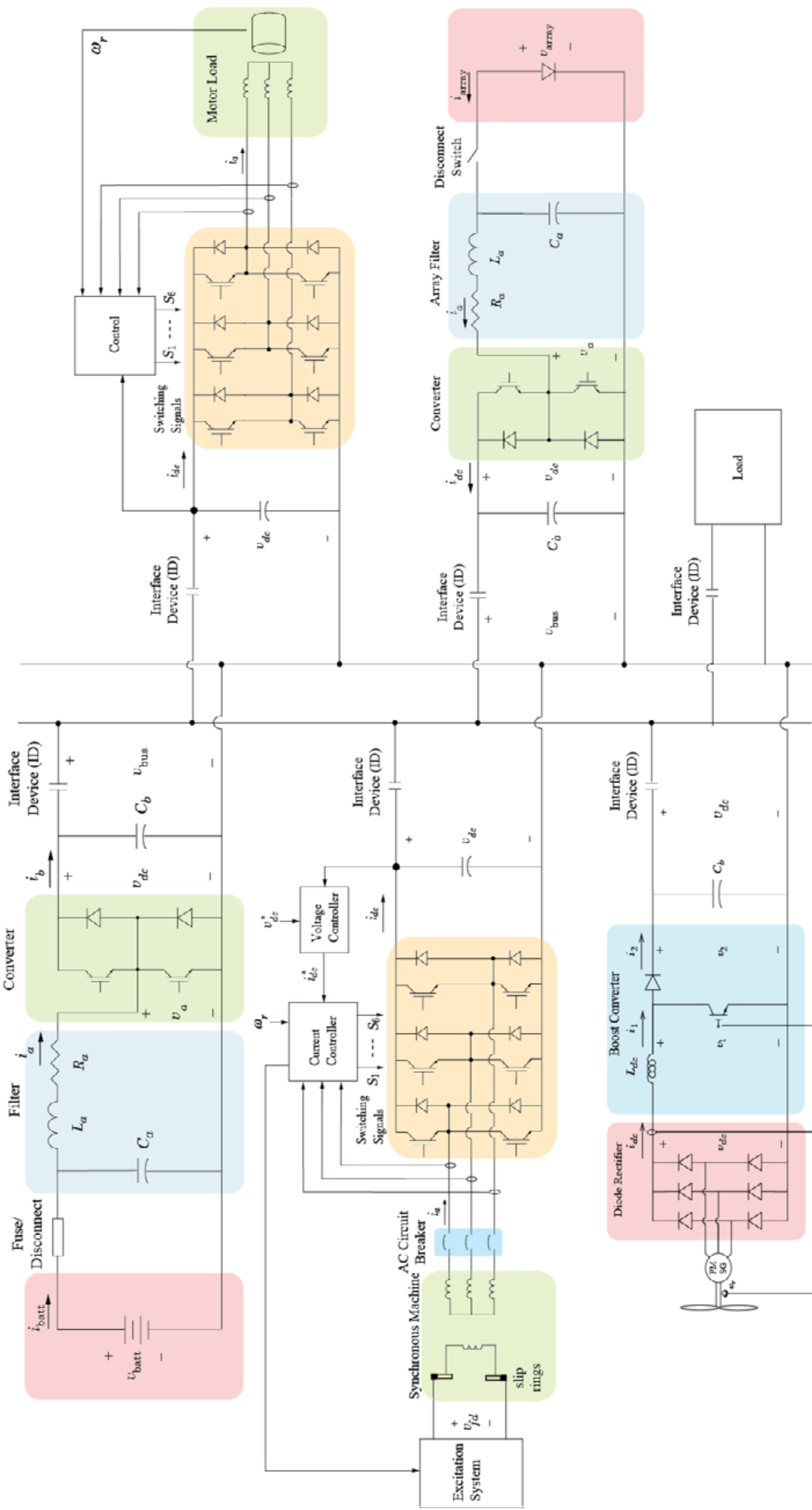

Figure 2-6 Example dc microgrid.

2.1 Stability and Control of Dc Microgrids

Microgrids may consist of disparate sources and loads with significantly different response characteristics. For example, fuel cells or inertial sources may be slow to respond to changes in load requiring energy storage to maintain the bus voltage following sudden and/or large changes in load. Photovoltaic and/or wind energy sources are subject to variability and, if operated at their peak-power point, may be viewed as time-varying negative loads. Electrical loads too may have vastly different dynamic characteristics. Some loads, such as regulated electronic loads or motor drives, often exhibit a negative incremental impedance characteristic. That is, the current drawn by the load increases if the bus voltage decreases. A generally accepted worst-case scenario occurs when all of the loads are controlled such that they consume the same amount of power even if the bus voltage varies. In other words, all of the loads are constant-power loads (CPLs). For small variations in voltage, CPLs behave dynamically like a negative resistance over an infinite frequency range. Consequently, systems with a large penetration of CPLs typically possess modes (natural frequencies) with less damping than systems with constant-current or constant-impedance loads.

Due to the aforementioned reasons, control and stability are important issues on par with protection (safety), thermal management, and reliability. The purpose of this section is to outline established techniques of analyzing stability characteristics of isolated dc microgrids that are composed of multiple sources and loads connected to a common dc bus in which the cabling impedances are negligible. If the impedances of the lines connecting the microgrid components to the dc bus are negligible, and the microgrid is not connected to a larger grid, it is referred to as a stiffly connected isolated dc microgrid (SCIDCM).

2.1.1 Nyquist analysis

It is useful to initially consider a system consisting of two sources and one load, which may represent an aggregate of many loads, as shown in Figure 2-7. Therein, υ_1^* and υ_2^* are the commanded output voltages of Source 1 and 2, respectively, and υ_b is the bus voltage.

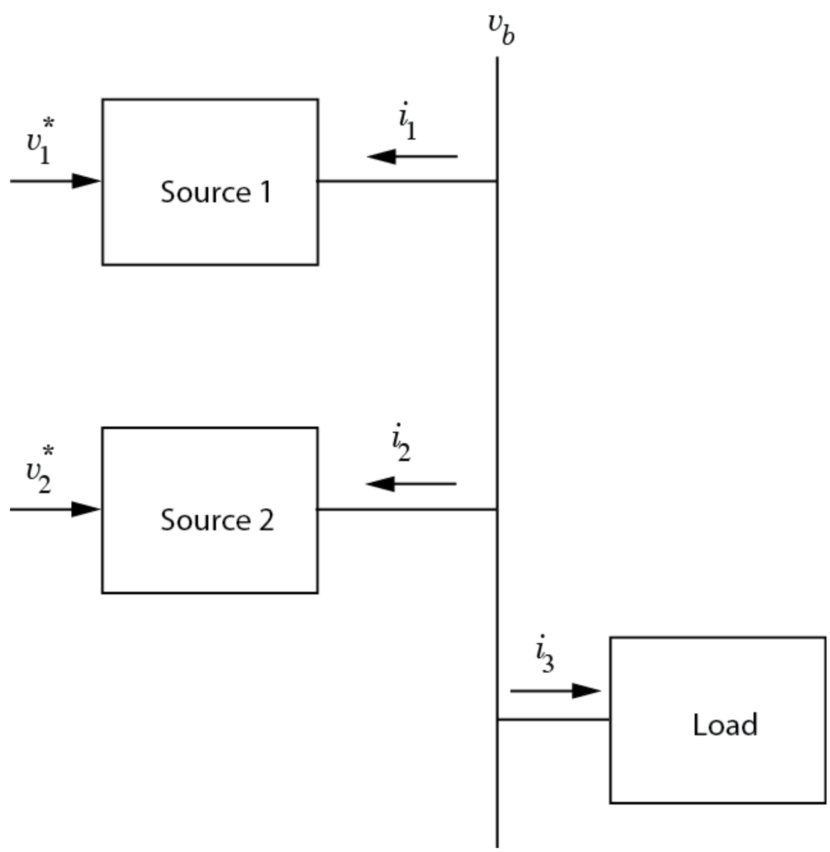

Figure 2-7 One-line diagram of a two-source stiffly-connected isolated dc microgrid.

In the given system, there are two independent sources that are assumed to regulate the same bus voltage. The subsequent equations are expressed in the frequency (s) domain. Also, v_b (Δv_b) is (change in) the bus voltage. The superscript * indicates that the asterisked variable is its commanded value (i.e. a control signal).

$$\Delta i_1 = Y_1 \Delta v_b - Y_1^* \Delta v_1^* \tag{2.1}$$

$$\Delta i_2 = Y_2 \Delta v_b - Y_2^* \Delta v_2^* \tag{2.2}$$

$$\Delta i_L = Y_L \Delta v_b \tag{2.3}$$

Here, Y_i is the source/load admittance and Y_i^* is a control-related admittance function relating the change in source current to a change in commanded voltage. A numerical method of establishing these admittances is described in Section 2.5.4. Summing (2.1) through (2.3),

$$0=\left(Y_1+Y_2+Y_L\right)\Delta v_b-Y_1^*\Delta v_1^*-Y_2^*\Delta v_2^* \tag{2.4}$$

Solving for Δv_b

$$\Delta v_b=\frac{Y_1^*\Delta v_1^*}{Y_1+Y_2+Y_L}+\frac{Y_2^*\Delta v_2^*}{Y_1+Y_2+Y_L} \tag{2.5}$$

Equivalently,

$$\Delta v_b=\frac{Z_1Y_1^*\Delta v_1^*}{1+Z_1\left(Y_2+Y_L\right)}+\frac{Z_2Y_2^*\Delta v_2^*}{1+Z_2\left(Y_1+Y_L\right)} \tag{2.6}$$

Let

$$Y_i=\frac{n_i}{d_i} \tag{2.7}$$

$$Y_i^*=\frac{n_i^*}{d_i^*} \tag{2.8}$$

where n_i and d_i are polynomials in *s*. Then

$$\Delta v_b=\frac{n_1^*d_1\Delta v_1^*}{d_1^*n_1\left[1+Z_1\left(Y_2+Y_L\right)\right]}+\frac{n_2^*d_2\Delta v_2^*}{d_2^*n_2\left[1+Z_2\left(Y_1+Y_L\right)\right]} \tag{2.9}$$

Sufficient and necessary conditions for stability include:

1. no n_i zeros in RHP (this should not be a problem)
2. no d_i^* zeros in RHP (this also should not be a problem)
3. no zeros of $1+Z_1\left(Y_2+Y_L\right)$ in RHP $\Leftrightarrow$ no encirclements of $-1+j0$ by Nyquist contour of $Z_1\left(Y_2+Y_L\right)$
4. no zeros of $1+Z_2\left(Y_1+Y_L\right)$ in RHP $\Leftrightarrow$ no encirclements of $-1+j0$ by Nyquist contour of $Z_2\left(Y_1+Y_L\right)$

Sufficient conditions for stability include:

5. Condition 3 suggests that $\left|Z_1\right|$ and/or $\left|Y_2 + Y_L\right|$ should be small (product less than 1) to avoid encirclements of $-1 + j0$. This is known as the Middlebrook criterion, which is sufficient but not necessary.
6. Condition 4 suggests that $\left|Z_2\right|$ and/or $\left|Y_1 + Y_L\right|$ should be small (product less than 1) to avoid encirclements of $-1 + j0$ (Middlebrook strategy).

Sufficient Conditions 5 and 6 are inconsistent (they both cannot both be satisfied). Since the Middlebrook criterion is sufficient but not necessary, this does not mean system will be unstable; rather, the Middlebrook criterion is not the appropriate strategy for analyzing paralleled sources connected to stiff bus. Necessary conditions 3 and 4 do, however, suggest that it is desirous for Y_L (load admittance) to be small, (i.e. loads to look like a current sink).

Suppose momentarily that

$$Z_i(\omega) = r_i f(\omega) \tag{2.10}$$

$$Y_i(\omega) = \frac{1}{r_i} f^{-1}(\omega) \tag{2.11}$$

for all *i* where r_i is a scale factor. Then

$$Z_1(Y_2 + Y_L) = r_1\left(\frac{1}{r_2} + \frac{1}{r_L}\right) \tag{2.12}$$

$$Z_2(Y_1 + Y_L) = r_2\left(\frac{1}{r_1} + \frac{1}{r_L}\right) \tag{2.13}$$

which are both real numbers independent of frequency (meaning no encirclements!). From Conditions 3 and 4, the system is guaranteed to be stable.

Equation (2.10) requires that all sources and loads have same frequency-response characteristics with perhaps a scale factor related to its power rating. This, in turn, implies the time-domain (e.g. step) responses also have same shape. This requirement would be difficult if not impossible to achieve in practice. At the very least, it is unreasonable. Specifically, some sources may exhibit inductive characteristics at high frequency, while others may exhibit capacitive characteristics. Some may be slower to react to changes in loads (inertial sources or fuel cells, for example) while others are faster (e.g. batteries or ultracapacitors). Nonetheless, Conditions 3 and 4 suggest that some level of coordination is necessary amongst sources to avoid encirclements and associated instability. Dynamic stability is an important consideration in the Open Architecture Power/Energy Management Framework discussed in a subsequent subsection.

2.1.2 Droop-Based Voltage Control

To set the stage for the discussion of droop-based control, it is convenient to initially consider the two-source one-load system of Figure 2-8. Therein, all sources have an inner current-control loop that allows the source to be modeled as a controllable current source whose reference (asterisked) current is defined by a droop-based voltage regulator. This structure is desirable since protective current limits can be readily incorporated into the control. In this subsection, it is assumed that the current loop is ideal (infinitely fast and no limits). That is, $i_i = i_i^*$. Also, it is convenient to assume the load is a constant-current load ($Y_L = 0$).

The underlying concept of a droop-based control strategy is that if a load step change (e.g. increase) occurs, each source contributes to the increase in load current in direct proportion to its rating – both in the steady and dynamic states. The latter condition implies that the frequency-response characteristics have the same shape. Let P_i denote the rating of source *i* and $P_{\text{net}} = \sum_{i=1}^{N} P_i$ is the total installed capacity in microgrid. The rated voltage of the dc bus is denoted as V_b, the rated current of source *i* is denoted $I_i = P_i / V_b$, and $i_{i,\text{pu}} = i_i / I_i$ is the per unit current of source *i*. Per unit impedance for source *i* is defined as

$$Z_i = \frac{V_b}{I_i} = \frac{V_b^2}{P_i} \tag{2.14}$$

Finally, the system base impedance is defined as

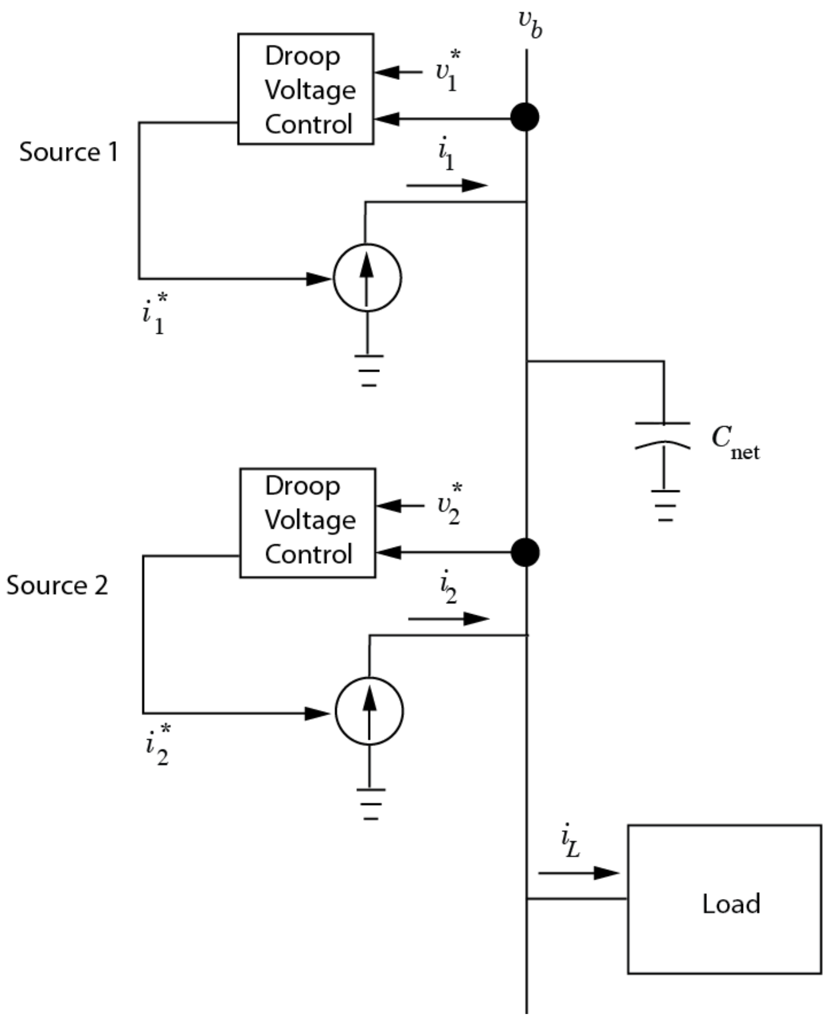

Figure 2-8 Droop-based control system.

$$Z_b = \frac{V_b}{I_{\text{net}}} = \frac{V_b^2}{P_{\text{net}}} \tag{2.15}$$

Many (not all) dc sources will have an output capacitor for filtering purposes. If the connections to the dc bus have negligible impedance, the capacitances are connected in parallel. In Figure 2-8, C_{net} denotes the net bus capacitance contributed by all sources/loads. The per unit value of C_{net} is defined as

$$C_{\text{net,pu}} = Z_b C_{\text{net}} \tag{2.16}$$

In a droop-based voltage-control strategy, the current reference is set so that the output-voltage-versus-current characteristics are as shown in Figure 2-9, i.e.

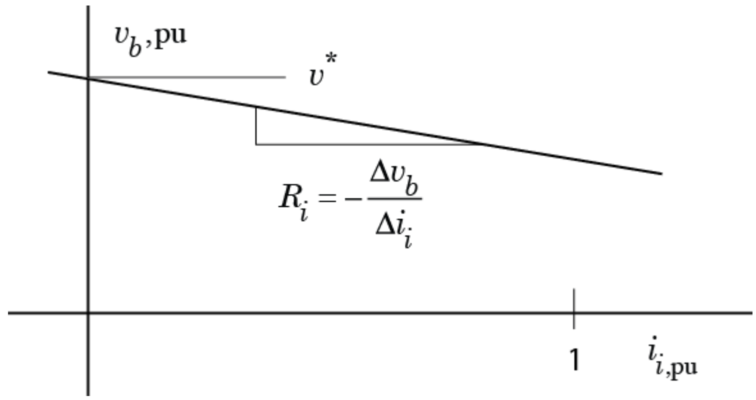

Figure 2-9 Output voltage versus current in droop-based control strategy.

$$i_{i,\text{pu}} = \frac{v^*_{i,\text{pu}} - v_{b,\text{pu}}}{R_{i,\text{pu}}} \tag{2.17}$$

Here, $R_{i,\text{pu}}$ is a regulation constant that appears resistive but does not contribute to real power losses. If $R_{i,\text{pu}}$ is expressed in per unit relative to the rating of the source, its per unit value relative to the net base power P_{net} is

$$R_{i,\text{pu,sys}} = R_{i,\text{pu}} \frac{P_{\text{net}}}{P_i} \tag{2.18}$$

If $R_{i,\text{pu}}$ are the same for all sources (with respect to the corresponding source rating P_i), each source contributes to changes in load current in direct proportion to its rating. If, moreover, each $v^*_{i,\text{pu}}$ is set to the same value, each source contributes to the steady-state net load current in direct proportion to its rating. Redistribution of current (power) among sources can be changed by setting $v^*_{i,\text{pu}}$ to different values while maintaining the same regulation constants $R_{i,\text{pu}}$. Thus, the steady-state distribution of net load current among sources may be different from the transient distribution. It may be desirable to have the faster-acting sources participate more aggressively in the regulation of bus voltage, with slower sources having a diminished role. This can readily be accomplished by increasing the value of $R_{i,\text{pu}}$ in the slower sources. In the extreme case, where $R_{i,\text{pu}}$ along with $v_{i,\text{pu}}^{*}$ are set to very large values, the source behaves like a constant-current source whose current is equal to $v_{i,\text{pu}}^{*} \big/ R_{\text{i,pu}}$.

Solving for the change in bus voltage

$$\Delta v_{b,\text{pu}} = \frac{1}{sC_{\text{net,pu}}} \sum_{i=1}^{N} \frac{\Delta v_{i,\text{pu}}^{*} - \Delta v_{b,\text{pu}}}{R_{i,\text{pu,sys}}} \tag{2.19}$$

Simplifying,

$$\Delta v_{b,\text{pu}} = \frac{1}{sC_{\text{net,pu}} + R_{\text{net,pu}}^{-1}} \sum_{i=1}^{N} \frac{\Delta v_{i,\text{pu}}^{*}}{R_{i,\text{pu,sys}}} \tag{2.20}$$

where

$$R_{\text{net,pu}} = \frac{1}{\sum_{i=1}^{N} R_{i,\text{pu,sys}}^{-1}} \tag{2.21}$$

is the net regulation constant for the SCIDCM. In (2.21), the individual $R_{i,\text{pu,sys}}$ are expressed in pu with respect to the net (system) power rating. If all sources have the same $R_{i,\text{pu}}$ with respect to the corresponding source rating (e.g. 0.05), then it is readily shown that $R_{\text{net,pu}}$ will also be equal to 0.05 when expressed in per unit relative to the net power rating.

According to (2.20), for the given control strategy, the system will exhibit a first-order response for step changes in $\Delta v_{i,\text{pu}}^{*}$ with a time constant of $R_{\text{net,pu}} C_{\text{net,pu}}$. Due to droop, the system will, in general, exhibit a steady-state error, e.g. $v_{b,pu} \neq 1$. In particular, if $v_{i}^{*} = 1$ and $R_{i,\text{pu}} = 0.05$ for all i, and the net load increases from 0 to P_{net}, the bus voltage will decrease from 1 to 0.95. The steady-state error can be corrected at next level of control by adjusting or scheduling $v_{i,\mathrm{pu}}^{*}$. A centralized scheduler, or power/energy management system (PEMS) handles potential redistribution of power among sources and correction of steady-state error. This control can have smaller bandwidth.

Comments on stability

In droop-based control, if the bandwidth of the current controller is infinite, $Y_i = 1/R_i$ and $Z_i = R_i$. Thus, Z_1Y_2 and Z_2Y_1 are both real numbers independent of frequency, which in turn implies there will not be any encirclements of -1 by Z_1Y_2 and Z_2Y_1, i.e. the system is guaranteed to be stable.

2.1.3 Effect of Finite Control Bandwidth

Now consider finite bandwidth of sources as shown in Figure 2-10. It is readily shown that the source admittance becomes

$$Y_i = \frac{1}{R_i(\tau_i s + 1)} \tag{2.22}$$

In (2.22) and hereafter, it is assumed that the R_i's are all expressed in per unit relative to the net power rating. The extra subscripts that were previously used to denote the base power are omitted for notational compactness. If, moreover, $Y_L = 0$ (constant-current load), the transfer function relating changes in bus voltage to changes in the reference voltages may be expressed

$$\Delta v_b = \frac{1}{sC_{\mathrm{net}} + \sum_{i=1}^{N} \frac{1}{R_i(\tau_i s + 1)}} \sum_{i=1}^{N} \frac{\Delta v_i^{*}}{R_i(\tau_i s + 1)} \tag{2.23}$$

For $N = 1$, the denominator polynomial expands to

$$s^2 C_{\mathrm{net}} R_1 \tau_1 + sC_{\mathrm{net}} R_1 + 1 \tag{2.24}$$

Applying the Routh-Hurwitz criterion [7] reveals that the system will be stable for all values of C_{net}, R_1 and τ_1. Moreover, applying the quadratic formula reveals that the system response will be overdamped if

$$R_1 C_{\mathrm{net}} > 4\tau_1 \tag{2.25}$$

and underdamped if

$$R_1 C_{\mathrm{net}} < 4\tau_1 \tag{2.26}$$

Selecting a regulation constant $R_1 = 0.05$ (comparable to the frequency droop in conventional ac power systems), the previous inequality suggests that the ratio of C_{net}/τ should be larger than 80 to produce a critically or overdamped response. Assuming, furthermore, a practicable current-control time constant of $\tau = 10$ ms, then $C_{\mathrm{net}} > 0.8\,\mathrm{pu}$ produces a stable overdamped response For purposes of interpretation, a C_{net} of 1 pu means that if all sources are suddenly set to zero (disconnected) with rated load current and an initial bus voltage of 1 pu, the bus voltage will collapse to zero in 1 sec. Equivalently, the stored energy at rated voltage is equal to half of the net power rating P_{net} times 1 sec. It must be noted that this represents a significant amount of capacitance; traditional values are typically much smaller since capacitors are commonly sized for the purpose of filtering switching-frequency harmonics rather than bulk energy storage. If a damped response is desired with a smaller value of bus capacitance, it is necessary for the source to have a faster response if a critically or overdamped response is desired.

It is interesting to compare the energy stored in a 1-pu capacitor to the kinetic energy stored in the rotating inertias of a conventional ac system. The typical inertia constant of a turbine generator, commonly denoted as H, is in the neighborhood of 5 sec [8]. The value is somewhat larger in the case of hydro generators. The corresponding rotational kinetic energy is equal to the generator power rating multiplied by the inertia constant. Thus, the energy stored in a C_{net} of 1 pu is roughly one fifth of the kinetic energy stored in a power system comprised of steam turbine generators.

It is also interesting to compare the voltage droop in a dc system with the frequency droop in an ac system. In both cases, droop is used as a first line of control for short-term mismatches between load and generation. However, since the form of stored energy is different, kinetic in an ac system and electrostatic in a dc system, droop-frequency control is used in ac systems whereas droop voltage control would be used in dc systems. In both cases, a droop of 5% appears reasonable since a 5% change in frequency or voltage is not likely to cause equipment damage especially if the change is short term.

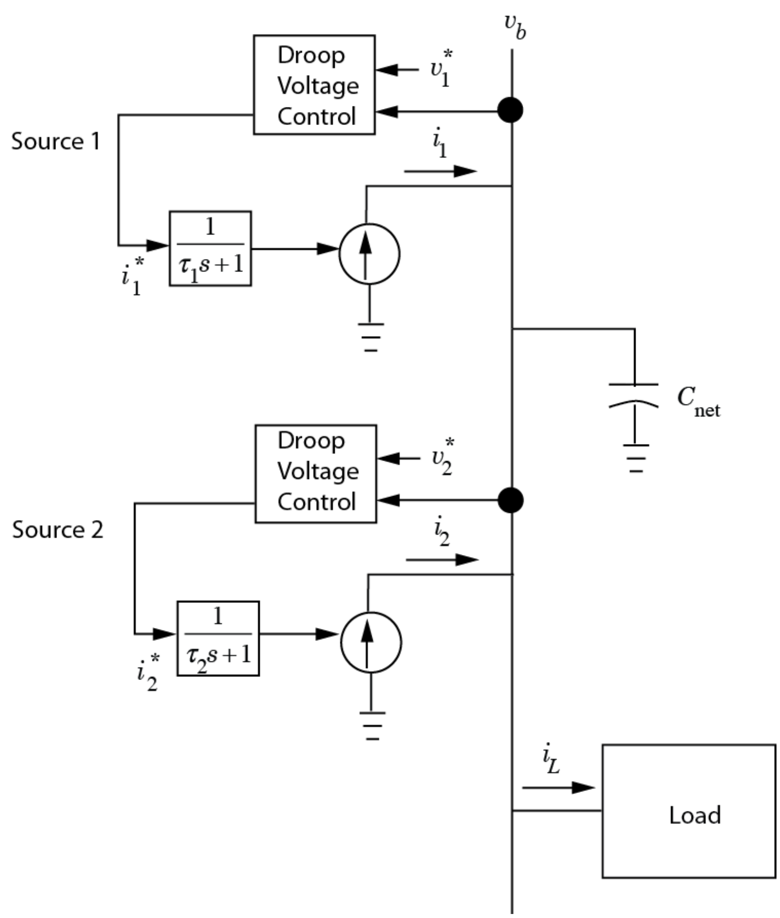

Figure 2-10 Droop controlled SCIDCM with finite source response times.

From (2.25), it can be observed there exists a three-way tradeoff between the regulation constant, the bus capacitance, and the responsiveness of the source. With the advent of ultracapacitors, a potential strategy in the design of SCIDCM's is to set C_{net} to a large value (e.g. 1 pu), and utilizing conventional droop compensation in all sources that participate in voltage regulation. For $C_{\text{net}} = 1\,\text{pu}$, $R_1 = 0.05\,\text{pu}$, and $\tau_1 = 0.01\,\text{s}$, the closed-loop time constants are readily established from (2.24) as $\tau_1 = 0.0138\,\text{s}$ and $\tau_2 = 0.0362\,\text{s}$, which are commensurate with the open-loop time constants. As noted previously, a smaller capacitance can be utilized if a faster source is employed. For example, with $C_{\text{net}} = 0.1\,\text{pu}$, $R_1 = 0.05\,\text{pu}$, and $\tau_1 = 0.001\,\text{s}$, the closed-loop time constants are identical to the previous example.

For $N = 2$, the denominator polynomial (2.23) expands to

$$s^3 C_{\text{net}} R_1 R_2 \tau_1 \tau_2 + s^2 C_{\text{net}} (\tau_1 + \tau_2) R_1 R_2 + s(R_1 \tau_1 + R_2 \tau_2) + (R_1 + R_2) \qquad (2.27)$$

Applying the Routh-Hurwitz test [7] reveals that the system will also be stable for all values of C_{net}, R_i and τ_i; however, the response may be underdamped. The same result can be verified for $N = 3$ and it is reasonable to conjecture that it is true for larger N, although this conjecture has not been verified. While this result is instructive, it is not necessarily true for more complex source dynamics.

For $C_{\text{net}} = 1\,\text{pu}$, $R_i = 0.1$ for $i = 1,2$ (resulting in an effective R_{net} of 0.05 since the sources are connected in parallel), and $\tau_i = 0.01\,\text{s}$, the closed-loop time constants are readily established as $\tau_1 = 0.0138\,\text{s}$ and $\tau_2 = 0.0362\,\text{s}$, and $\tau_3 = 0.01\,\text{s}$. It is interesting to note that the first two time constants are identical to those of the single-source example considered previously. Again, the response is overdamped with the closed-loop time constants commensurate with the open-loop values

2.1.4 Constant-Power Loads

In the preceding section, it was assumed that the incremental load admittance was zero implying a constant-current load (CCL). However, some regulated power electronic loads and some motor drives exhibit a constant-power characteristic. That is, if the bus voltage decreases, the control system compensates by adjusting the duty cycle such that the power delivered to the load remains constant. Such a load is frequently called a constant-power load (CPL). It is well known that CPLs can have a detrimental effect of the stability of power systems. A 1-pu CPL is defined herein as a CPL that draws rated power.

The incremental admittance of a CPL may be derived by first expressing load power as

$$P_L = vi \tag{2.28}$$

The differential change in load power may be expressed using ordinary calculus

$$dP_L = v\,di + i\,dv = 0 \tag{2.29}$$

The incremental load admittance becomes

$$G_L = \frac{di}{dv} = -\frac{i}{v} = -\frac{P_L}{v^2} \tag{2.30}$$

Here, the symbol G_L is used to emphasize that the load admittance (conductance) is a real quantity, albeit negative, in an ideal CPL. It is readily shown that for $N = 1$, the denominator of the transfer function relating the bus voltage to the commanded voltage becomes

$$s^2 C_{\text{net}} R_1 \tau_1 + s\left(C_{\text{net}} R_1 + G_L R_1 \tau_1\right) + 1 + G_L R_1 \tag{2.31}$$

For a CPL with $P_L = 1\,\text{pu}$ at rated voltage ($v = 1\,\text{pu}$), the incremental conductance of the load is $G_L = -1$ whereupon

$$s^2 C_{\text{net}} R_1 \tau_1 + s\left(C_{\text{net}} R_1 - R_1 \tau_1\right) + \left(1 - R_1\right) \tag{2.32}$$

For $C_{\text{net}} = 1\text{ pu}$, $R_1 = 0.05\,\text{pu}$, and $\tau_1 = 0.01\,\text{s}$, the closed-loop time constants are readily established as $\tau_1 = 0.0296\,\text{s}$ and $\tau_2 = 0.0178\,\text{s}$, which is a relatively minor shift from the original closed-loop poles (with $Y_L = 0$). It is worthy to note that the system is small-displacement stable and exhibits an overdamped response even with a 1-pu constant-power load.

It is instructive to establish the Nyquist contour of $Z_1 Y_L$ for the preceding parameters. It is readily shown that for $N = 1$, the sourced impedance is

$$Z_1 = \frac{R_1\left(\tau_1 s + 1\right)}{s^2 R_1 C_{\text{net}} \tau_1 + s R_1 C_{\text{net}} + 1} \tag{2.33}$$

For a 1-pu CPL, $Y_L = -1\,\text{pu}$, which is independent of frequency. The Nyquist contour of $Z_1 Y_L$ is plotted in Figure 2-11 as s is varied from 0 to $j\infty$. The Nyquist contour of $Z_1 Y_L$ as s is varied from $-j\infty$ to 0 is symmetrical with respect to the real axis and therefore need not be plotted. Since there are no open-loop poles in the right half plane, the number of right-half-plane closed-loop poles is equal to the number of clockwise encirclements of $-1 + j0$ by the Nyquist contour. Since there are no encirclements, the system is stable. Moreover, it is seen that the system is not even close to being unstable with a gain margin of approximately 20. In other words, $Z_1 Y_L$ must be increased by a factor of 20 before an encirclement (instability) occurs. Computer-aided methods of establishing the source and/or load impedance/admittance plots using more complex source/load models are described in Section 2.5.4.

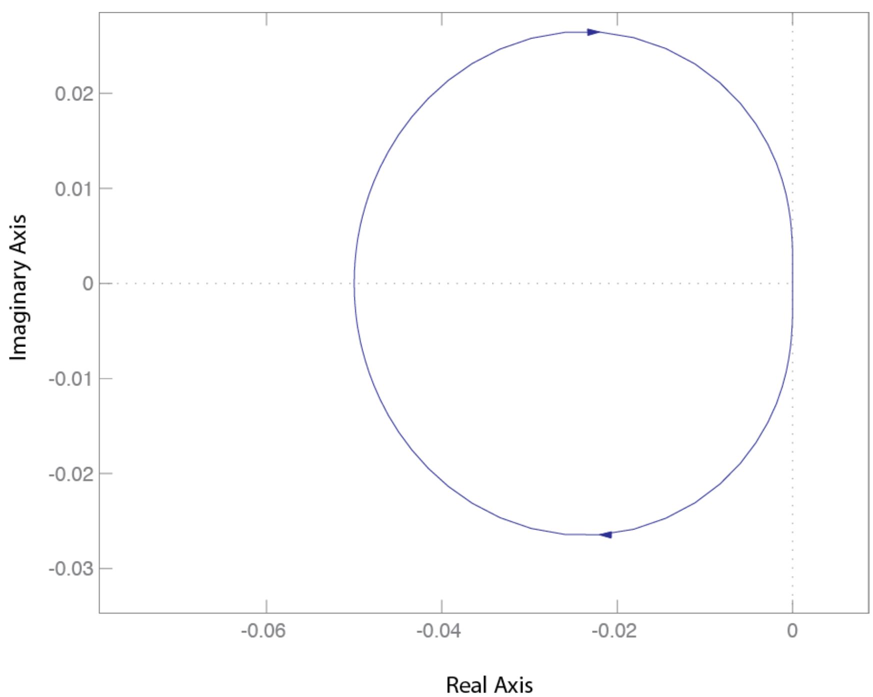

Figure 2-11 Nyquist contour of $Z_1 Y_L$ for $R_1 = 0.05\,\text{pu}$, $\mathrm{C}_{\text{net}} / \tau_1 = 100$, and $Y_L = -1\,\text{pu}$.

2.1.5 Large-Displacement Stability and the Effect of Current Limits

Consider an SCIDCM with finite response times and current limits as shown in Figure 2-12. If a source operates at a current limit, it behaves as a constant-current source ($Y_i = 0$), eliminating it from consideration in the small-displacement stability analysis. If all sources hit their limits, however, voltage regulation is lost. The potential for this condition should be monitored by the PEMS. If the majority of sources are operating at their current limit, it is necessary to bring additional sources on line or be prepared to shed load. Utilities typically maintain a 5-10% spinning reserve to accommodate any sudden load increases.

It is instructive to consider the large-displacement stability for the single-source system shown in Figure 2-13. The given system has two state variables (v_b and i_1). The region of asymptotic stability (RAS) can be established numerically by plotting the phase-plane trajectory for various initial conditions and is depicted in Figure 2-14 for $P_L = 1$, $R_1 = 0.05$, $C_{\text{net}} / \tau_1 = 100$, $i_{1,\text{ll}} = -1.2$, and $i_{1,\text{ul}} = 1.2$. The current limits were set to a value somewhat larger than ± 1 so as to ensure stability following transients. In Figure 2-14, the source current i_1 is plotted as a function of the voltage error, $v_b - v_1^*$. As shown, the RAS excludes the shaded portions $i_1 > i_{1,\text{ul}}$, $i_1 < i_{1,\text{ll}}$, and the left-hand region bounded by a trajectory beginning at Point *e*. All trajectories beginning in the unshaded RAS converge to the equilibrium point (Point *o*).

If the load power P_L is changed, the steady-state equilibrium point will also change since the droop control exhibits steady-state error. The locus of equilibrium points for $-1 \le P_L \le 1$ is depicted as a dashed line in Figure 2-14. For decreasing values of P_L, the left-hand unstable (shaded) region moves further to the left (RAS larger); however, the RAS continues to exclude the upper and lower regions, $i_1 > i_{1,\text{ul}}$ and $i_1 < i_{1,\text{ll}}$, due to the hard limits on the source current. It is interesting to note that if the initial state begins in the RAS depicted in Figure 2-14, the load power can be set to any value $-1 \le P_L \le 1$ at any point in time during the trajectory without causing the state to leave the RAS. This, in turn, implies that the given system will be large-displacement stable for any value of load power $-1 \le P_L \le 1$. For purposes of illustration, the time-domain step response for step changes in P_L from 0 to 1 to -1 and back to 1 is depicted in Figure 2-15. In summary, large-displacement stability with a CPL (the most destabilizing load characteristic) is ensured with a transient overload capacity of 20% and a C/τ ratio of 100.

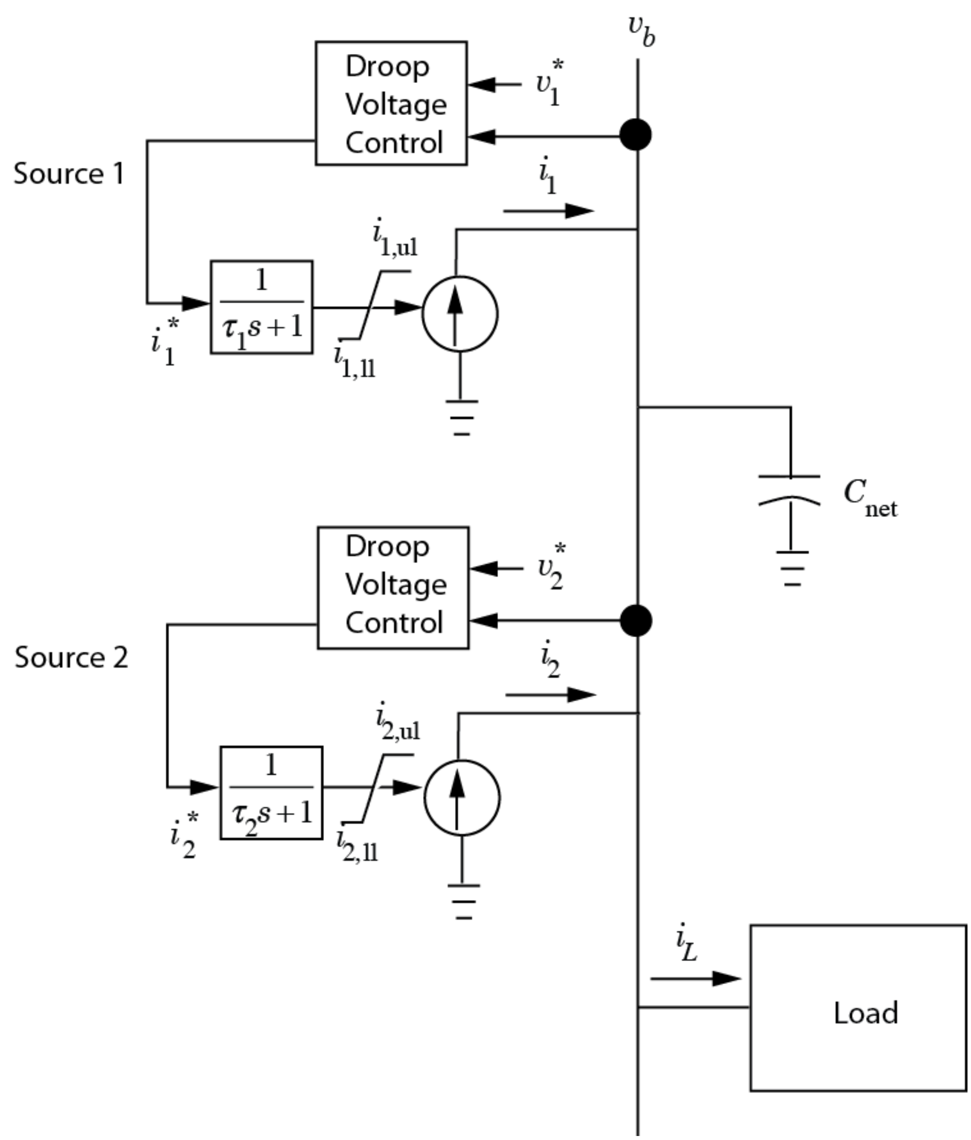

Figure 2-12 Droop-controlled SCIDCM with finite source response times and current limits.

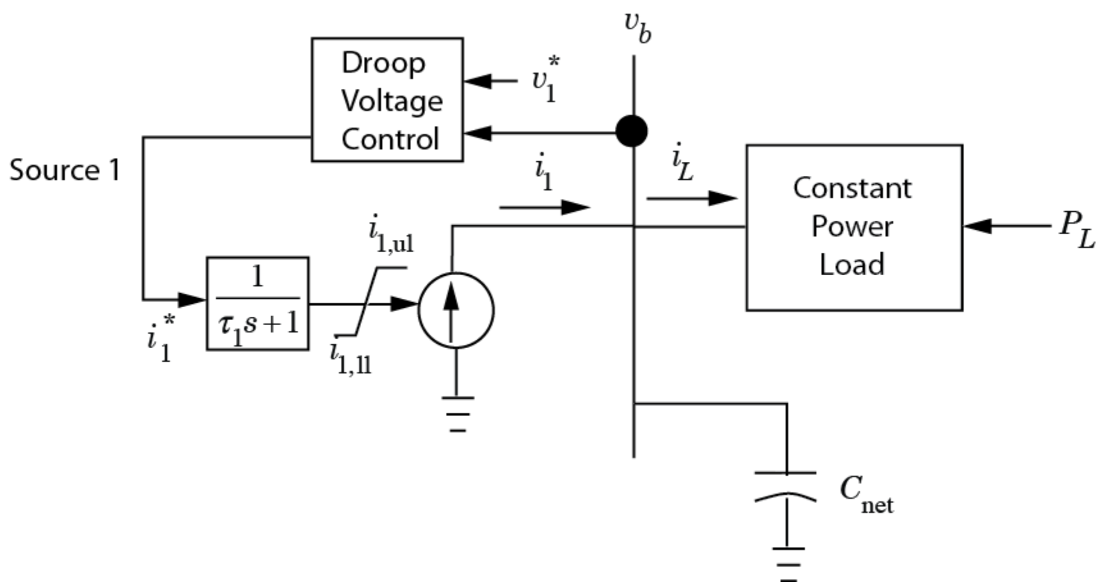

Figure 2-13 Single-source system with constant-power load.

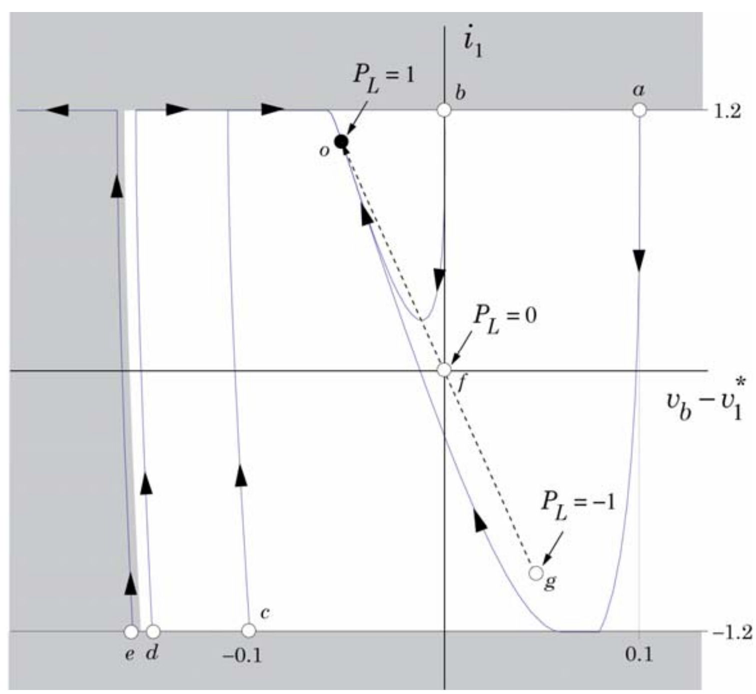

Figure 2-14 RAS (non-shaded region) for $P_L = 1\,\mathrm{pu}$, $R = 0.05\,\mathrm{pu}$, $C/\tau = 100$. Dashed line denotes loci of equilibrium points for $-1 \le P_L \le 1$. Trajectories beginning at Points *a*, *b*, *c*, and *d* are stable. Trajectory beginning at Point *e* is unstable.

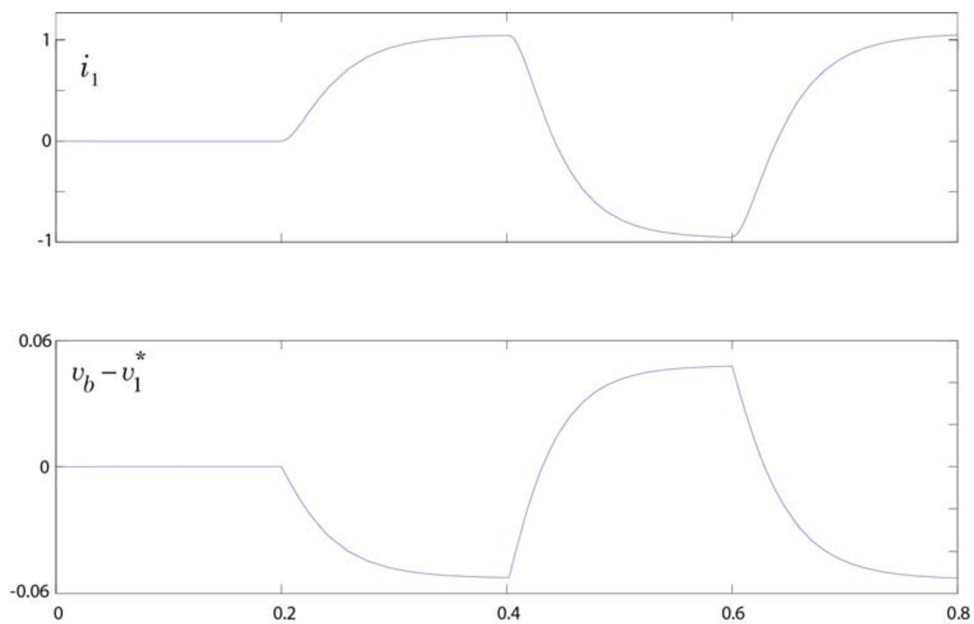

Figure 2-15 Step response for step changes in P_L from 0 to 1 to -1 and back to 1.

2.2 Power Quality

Although there does not exist a universally accepted and strict definition of power quality, the attributes of a system that are commonly associated with power quality include: continuity of service, variations in voltage magnitude, allowable transients in voltages and currents, and harmonic content in the waveforms for voltage and/or power. Allowable variations in voltage may be specified in the form of a magnitude-versus-time plot such as that shown in Figure 2-16, which is a part of MIL-STD-704F for aircraft electric power systems [9].

A large harmonic content in the voltages may lead to excessive losses (heating) in certain components, electromagnetic (radio) interference (EMI/RFI), and in extreme cases control-related dysfunctions. Thus, it is desirable to limit the allowable harmonic distortion during normal operating conditions. Allowable harmonic content for aircraft dc systems is shown in Figure 2-17.

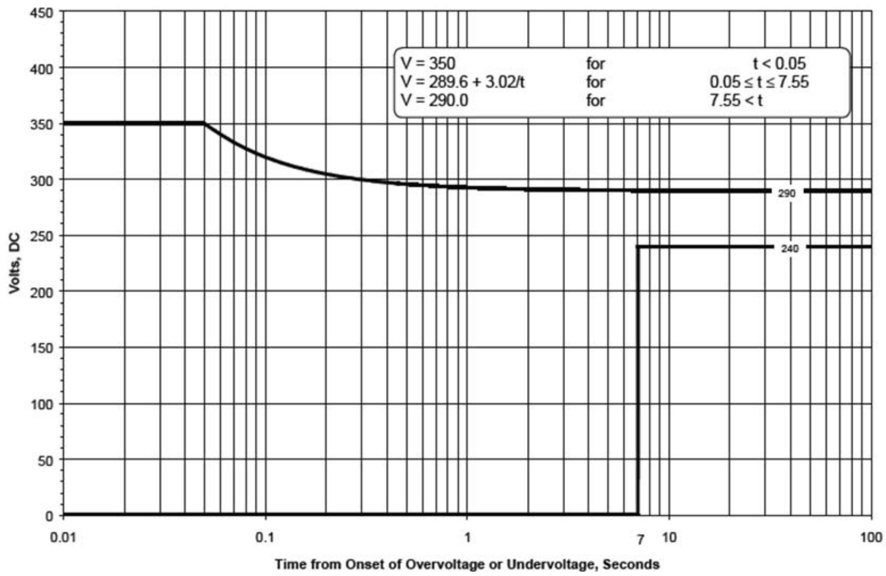

Figure 2-16 Allowable voltage deviation in an aircraft dc power system [9].

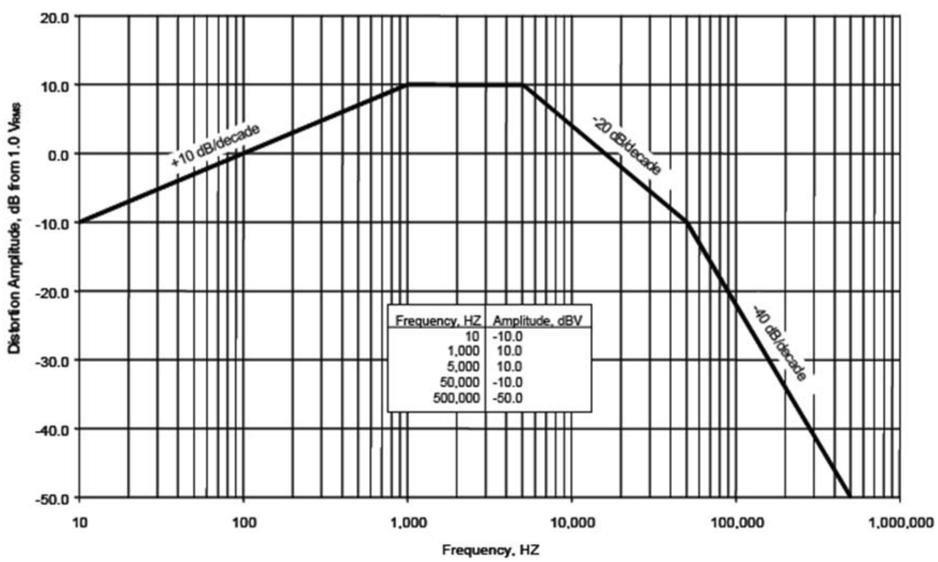

Figure 2-17 Allowable harmonic content in an aircraft dc power system [9].

2.3 Protection and Coordination

One of the several factors that had favored ac over dc during the early period of the electric power industry was the fact that fault currents in a dc system are limited primarily by the armature resistance of the dynamo. Since this resistance is made as small as possible to reduce losses during normal operation, the fault current is very large. Faults are typically interrupted by separating the metal-to-metal contacts in a circuit breaker. In ac or dc systems, an arc is typically produced due to very large induced voltages (attributed to Faraday's law) when the contacts are first opened. In an ac system, the arc is extinguished when the current naturally crosses zero and will not reignite provided the ensuing voltage does not exceed the sparking potential of the separated contacts.

In a dc system, however, it may be necessary to extinguish the arc by other means such as blowing it out using a blast of air (or other gas), or creating a magnetic field causing it to elongate, thereby increasing its resistance and eliminating the thermodynamic conditions needed for the arc to sustain itself. The physics of arc modeling is very complex to say the least and circuit breaker ratings are typically established using extensive laboratory testing. Some circuit breakers are rated for both dc and ac applications, although the dc ratings are generally less than the corresponding ac rating. For example, a commercially available 250-Vac (rms) breaker, when used in a dc system, is rated only 65 V dc as shown in Figure 2-18.

Solid-state circuit breakers offer an advantage when used in dc systems since the turn-off transients can be accurately controlled so as to avoid large inductive voltage spikes. However, a disadvantage of solid-state breakers is the presence of on-state losses attributed to a voltage drop across the device when it is on. A hybrid approach, whereby a solid-state breaker is used in parallel with a conventional one, can be used to take advantage of the benefits of each technology.

2.4 An Open Architecture Power /Energy Management Framework

Preceding studies (Section 2.1.5) have shown that in a single-source stiffly connected dc microgrid, a capacitance-to-response-time ratio exceeding 80 results in a very stable and well-damped response even with a 1-pu CPL (rated-power CPL). In systems with multiple sources and loads, each with diverse response characteristics, the situation is considerably more complex. In an *N*-source SCIDCM, the RAS dimension is $N+1$, which makes it considerably more difficult to establish and interpret graphically. However, time-domain simulation and small-displacement analysis based upon the frequency-response characteristics remain powerful tools for characterizing stability in more complex systems.

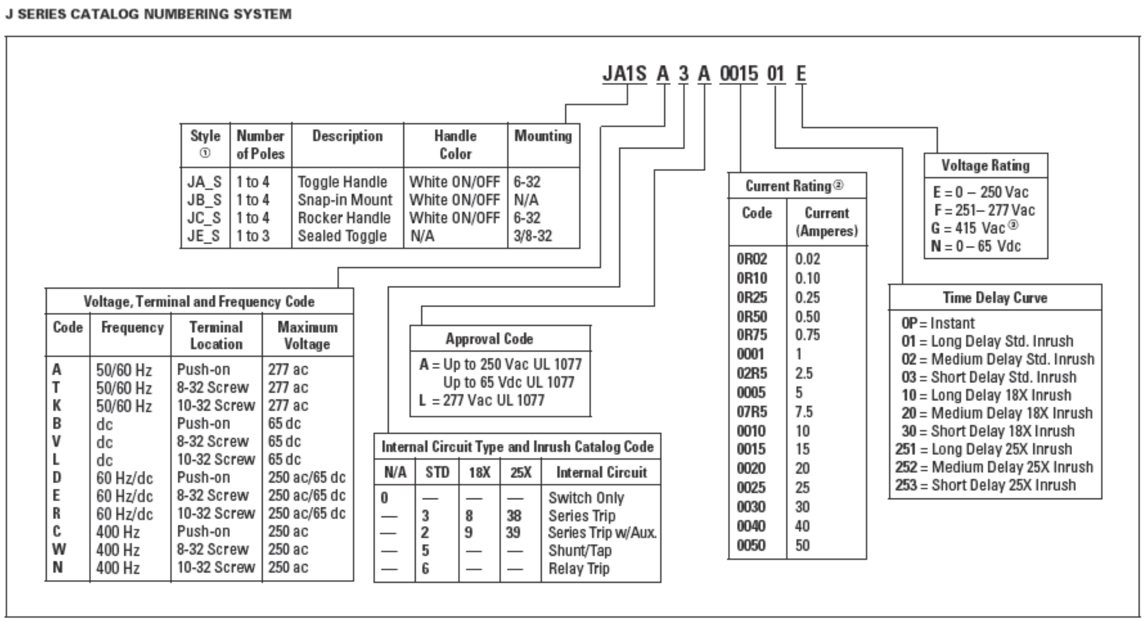

Figure 2-18 Commercially available circuit breaker ratings [10].

Unlike conventional power systems, microgrids typically include a small number of sources and loads, which precludes the use of "statistically averaged" source and/or load models (dynamic equivalents). Moreover, the connection or disconnection of any individual source or load may have a significant influence on the dynamic characteristics of the microgrid. In order to ensure stable, safe, and sustained operation for a wide range of operating conditions, it can be argued that a centralized power and energy management system (PEMS), analogous to an Independent System Operator (ISO) in the U.S. power grid, is needed. The PEMS, like an ISO, serves as a "middle man" for transactions between loads and sources. A circuit/block diagram of a microgrid with *N* sources and *M* loads is depicted in Figure 2-19. Therein, an Open Architecture Power/Energy Management Framework is utilized to facilitate coordination among sources and loads.

For purposes of discussion, it is assumed that each source can be characterized by a small number of parameters: τ_{Si} - response time, R_i - voltage regulation constant, $i_{Si,\mathrm{ll}}$ - lower current limit, $i_{Si,\mathrm{ul}}$ - upper current limit, and C_{Si} - bus capacitance. Loads are assumed to have a similar set of parameters; however, since they do not participate in the regulation of bus voltage, load parameters do not include a voltage regulation constant R_i. In Figure 2-19, sources and loads are connected to the main bus, commonly called the point of common coupling (PCC), through an interface device (ID) that can isolate the source or load in the event of a fault. Unlike a conventional circuit breaker, an ID is capable of communicating its status to the PEMS. Moreover, the PEMS is able to command the ID to open or close. The ID may be conventional (separable metal-to-metal contacts), solid state (e.g., field-effect or IGBT transistors), or a hybrid combination of conventional and solid state devices. A solid-state ID has the advantage that they can be programmed to limit currents in the event of a fault (provided they can dissipate the power loss that occurs in the device during the fault); however, they have the disadvantage of a steady-state voltage drop (power loss) during normal operation.

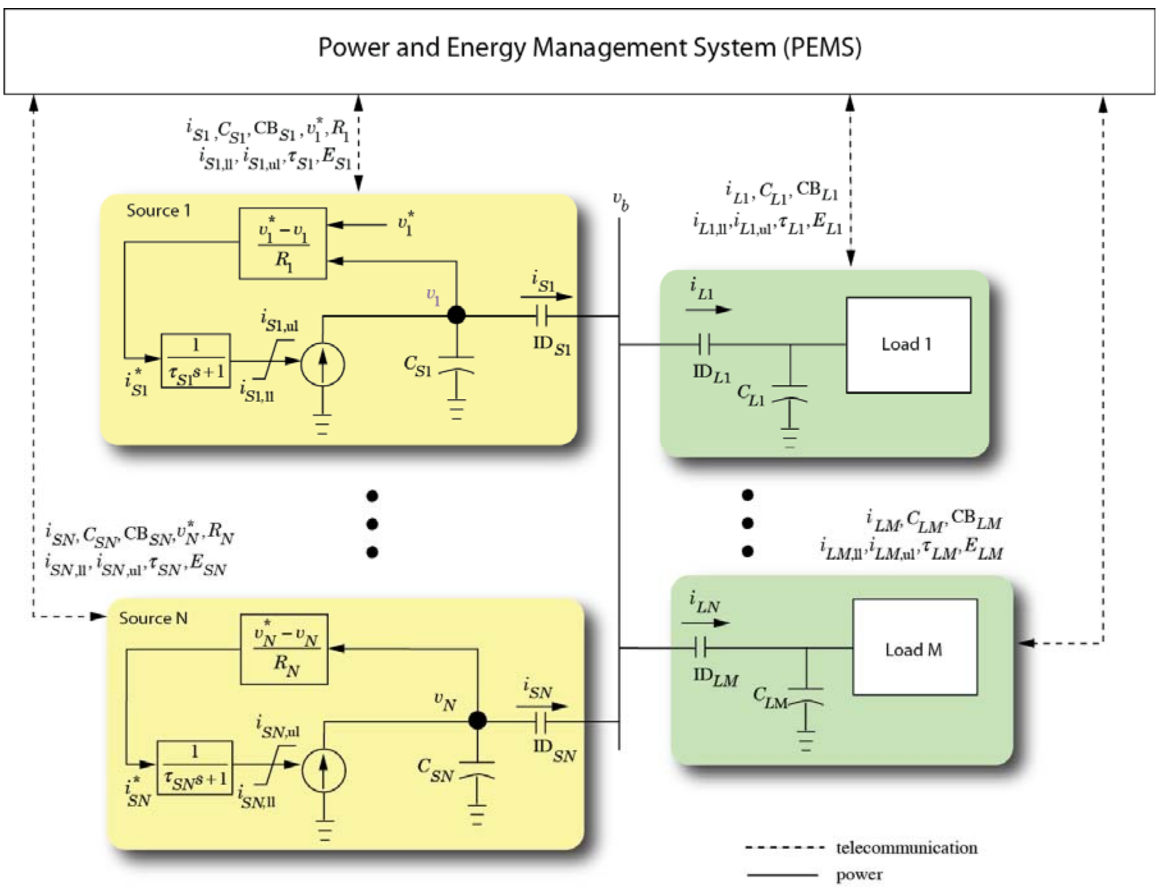

Figure 2-19 Potential Open Architecture Framework with droop-based voltage regulation.

The primary role of the PEMS is to coordinate sources and loads to ensure stable and reliable operation of the microgrid. To accomplish this goal, the PEMS monitors key parameters and variables as delineated below.

Monitored parameters/variables for sources:

1. Connection (ID) status
2. Bus capacitance C_{Si}
3. Current/power response time constant or maximum slew rate, τ_{Si}
4. Current/power limits, $i_{Si,\text{ll}}$, $i_{Si,\text{ul}}$
5. Available energy, E_i
6. Voltage regulation constant, R_i
7. Reference voltage, v_i^*
8. Actual current, i_{Si}
9. Frequency-response characteristics, $Y_i(\omega)$ (possibly operating-point dependent)

In addition to monitoring key parameters and variables, the PEMS is also capable of setting or dispatching the values of certain parameters and variables as delineated below.

Dispatchable parameters/variables for sources:

1. Connection status (PEMS can disconnect unruly sources and/or loads)
2. Regulation constant, R_i
3. Reference voltage, v_i^*

In a conventional droop-based control strategy, the regulation constant is set to the same value for all sources (in per unit relative to the corresponding source rating) and is not dispatchable. In this case, all sources respond proportionately to their rating to changes in net load. The steady-state distribution of power among sources can be adjusted by dispatching v_i^*. That is increasing v_i^* for source i will increase its steady-state contribution to the net load; however, the source will continue to respond proportionate to its rating to subsequent changes in net load. This strategy has two main advantages. First, a sudden and unexpected loss of an individual source will not necessarily result in a complete loss of power (blackout). The remaining sources will respond autonomously through their independent droop-based voltage regulators. Second, the loss of communications with the PEMS or the loss of the PEMS itself will not necessarily result in the loss of power since the individual sources have a considerable degree of autonomy.

In some cases, it may be desirable to set the regulation constant to a value significantly different from the remaining sources. For example, it is reasonable to conjecture that faster sources should participate more (or slower sources less) aggressively in the regulation of bus voltage. In one extreme, where R_i and v_i^* are simultaneously set to large values with the ratio v_i^* / R_i set to a constant (say I_i^*), the source, in effect, becomes a constant-current source. In the other extreme where the regulation constant R_i is set to zero, the source, in effect, becomes a constant-voltage source.

Another viable operating strategy is to identify a single source such as a battery energy storage unit (BESU) to be the primary regulator of voltage with the remaining dispatchable sources controlled so as to emulate constant-current sources. The BESU, in effect becomes the slack generator that supplies or absorbs all of the mismatch between the net load and the power generated by non-slack sources. The long-term energy state of the BESU can be controlled by adjusting I_i^* in the non-slack dispatchable sources. A disadvantage of this strategy is that the loss of the BESU will result in the total loss of voltage regulation and likely blackout. A second disadvantage is that the BESU must absorb or supply any and all changes in load prior to the PEMS's rescheduling of I_i^*. If the net change in load exceeds the BESU rating, a significant voltage transient will occur potentially resulting in a cascading sequence of events leading to a blackout.

Allowing R_i to be dispatchable in an Open Architecture Framework, a wide variety of operating strategies are permissible. This flexibility is desirable since the optimal strategy is likely to be dependent upon specific applications and operating conditions (i.e., system state). For example, a military microgrid in a forward operating base may require a tightly regulated voltage to support sensitive electronic loads. The sources may be diverse and include a mix of solar, wind, and/or fossil-fuel-based rotating sources operating in conjunction with a BESU. The fossil-fuel-based source is likely to be considerably slower than the BESU while the solar and wind generators are typically controlled so as to extract maximum power from renewable sources. Therefore, the most apparent strategy would be for the BESU to be the primary regulator (slack source) with the remaining dispatchable sources to be controlled as current sources, while the renewable sources, when operated at peak power, behave like negative loads. On the other hand, in a commercial or residential microgrid that includes a much larger number of sources and loads, a distributed approach may be more appropriate wherein the regulation of bus voltage is shared among a variety of distributed sources. The Open Architecture Framework should be sufficiently flexible to accommodate either scenario

In addition to monitoring of the key variables for the available sources, it is desirable to monitor several key parameters and variables associated with loads as described below.

Monitored parameters/variables for loads:

1. Connection (ID) status
2. Bus capacitance C_{Li}
3. Current/power response time constant or maximum slew rate, τ_{Li}
4. Current/power limits, $i_{Li,\text{ll}}$, $i_{Li,\text{ul}}$
5. Anticipated (requested) energy use, E_{Li}, prior to shutdown.
6. Actual current, i_{Li}
7. Frequency-response characteristics, $Y_{Li}(\omega)$ (possibly operating-point dependent)

Since loads are likely to be designed for specific functions, the only assumed dispatchable variable associated with a load is its connection status. If the PEMS determines that a load is unruly (e.g., absorbing more power than requested) or if insufficient generation exists to support the load, the PEMS is capable of disconnecting any and all loads through a dispatched ID signal.

In the Open Architecture Framework, loads do not communicate directly with individual sources but with the PEMS. A typical dialog between pending load and the PEMS may consist of the following steps:

- The load requests to draw a specified amount of power/energy from the microgrid.
- The PEMS is aware of active (on-line) sources and their state (incremental power capacity, available energy, …).
- The PEMS determines whether the load request can be supported without violating current limits or causing instability. In this regard, it is useful to note that on-line monitoring of the gain and/or phase margin is technically feasible given knowledge of source and load frequency-response characteristics.
- If the PEMS determines there are insufficient resources to supply the existing and pending loads, it may first issue a request to an off-line source(s) to become active. The associated capacitance can (should) be pre-charged prior to ID closure to minimize electric transients (analogous to the synchronization of an ac generator in the conventional grid)
- If the PEMS determines there are insufficient sources to supply existing and pending loads after all available off-line sources are activated, low-priority loads may be disabled to support the pending load transaction provided the pending load has a higher priority.
- If the load request can be supported, the PEMS sends a signal to the load allowing the associated ID to close and the load to begin drawing power. Standards are needed to limit inrush currents (e.g. charging of bus capacitance) to avoid undesirable transients. In-rush current can be limited using pre-insertion resistors or current-limiting solid-state circuit breakers.

During normal operating conditions, the PEMS may activate/deactivate sources so as to maintain an "active reserve" (analogous to the spinning reserve in the conventional power system), which serves to prevent a total blackout in case of unanticipated loss of a single source. An "active reserve" source is one in which the corresponding ID is closed but v_i^* scheduled so that the average power supplied by the source is zero. Moreover, the PEMS can periodically monitor the stability margin and/or perform Monte-Carlo-like time-domain simulations for a prescribed set of contingencies (bus faults, unanticipated loss of source or load) to identify vulnerabilities. If needed, additional sources can be "activated" for improved reliability.

In Figure 2-19, sources are approximated using a very simplified model that may or may not adequately represent the true dynamics of a source. However, the concepts described herein regarding an Open Architecture Framework and droop-based voltage regulation apply nonetheless. It is very desirable from an Open Architecture perspective that suppliers or vendors of equipment provide models and associated parameters that adequately approximate the actual dynamic and steady-state characteristics. Such models could be incorporated into the time- and/or frequency-domain simulations performed by the PEMS to more accurately predict stability margins, identify vulnerabilities, and, if necessary, adjust dispatchable parameters to augment system stability.

Given the data previously identified, the PEMS is capable of monitoring availability of energy and anticipated energy use. In order to optimize the available resources (optimum dispatch), the PEMS is capable of adjusting the division of net power among active sources by calculating and dispatching optimal v_{Si}^*. The PEMS can also adjust individual R_i's for stability purposes. In the extreme case where R_i is set to a large value, the source, in effect, becomes a constant-current source and in the other extreme where R_i is set to zero, it becomes a voltage source. Finally, in the event of a complete loss of power, the PEMS is responsible for implementing a black-start procedure wherein sources and loads are activated in an appropriate sequence to restore the microgrid to a normal operating state.

Comments:

- With dynamically changing loads, there is an ever-present mismatch between generation and consumption.

- The short-term power mismatch is "absorbed/supplied" by the net bus capacitance causing short-term voltage variations. A larger capacitance <-> smaller voltage variations.

- The mid-term power mismatch is controlled by increasing/decreasing the current command signals for active sources. This is accomplished at local level using droop-based voltage regulators.

- The long-term distribution of power among sources is handled by supervisory PEMS that can redistribute power flow by rescheduling v_{Si}^{*}. Temporal average of bus voltage can be controlled at PEMS level.

- The given architecture is federated in the sense that sources and loads have sufficient autonomy to continue operation in the event of the loss of communication with the PEMS. The PEMS, however, is capable of overseeing the entire system and can coerce individual sources (through scheduling of v_{Si}^{*}) to operate in a manner that benefits the system as a whole (improved reliability, optimal use of nonrenewable fuels, …).

2.5 Stability of Interconnected Dc Microgrids

In this section, an analytical approach for characterizing the stability of two dc microgrids interconnected via a potentially long transmission line is described. Herein, it is assumed that two different microgrids, each consisting of a variety of sources and loads, are to be interconnected via a long dc transmission line as shown in Figure 2-20. The dc line parameters include the inductance, resistance, and capacitance per unit length, as well as the line length.

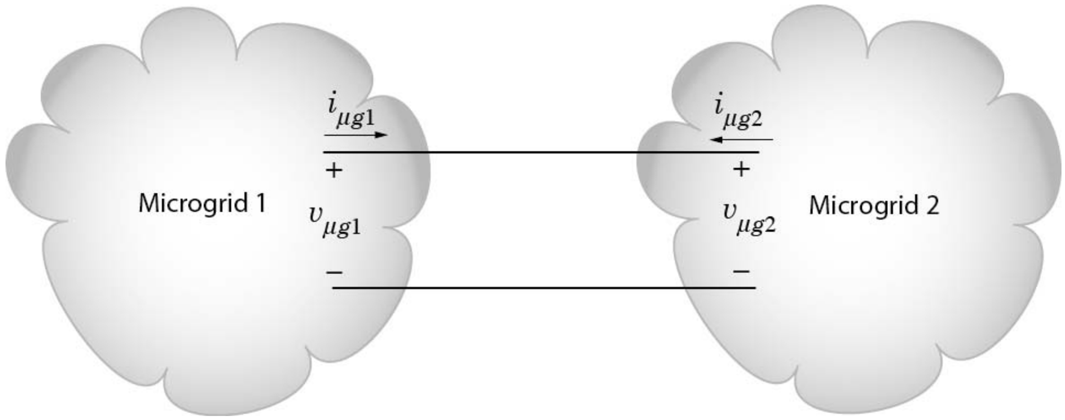

Figure 2-20 Two microgrids interconnected via dc line.

The voltage and current at the point of interconnection in Microgrid 1 is denoted as $v_{\mu g1}$ and $i_{\mu g1}$, respectively. Likewise, the voltage and current in Microgrid 2 at the point of interconnection is denoted as $v_{\mu g2}$ and $i_{\mu g2}$, respectively.

2.5.1 Small-Displacement Equations

For small variations in the voltages and currents, the dynamic behavior of Microgrid 1 may be characterized using a linearized system of equations that can be expressed in transfer-function form as

$$\Delta v_{\mu g1} = -Z_{\mu g1}(s)\Delta i_{\mu g1} + H(s)\Delta v^{*}_{\mu g1} \tag{2.34}$$

Here, Δ denotes the variation from an operating point and $v^{*}_{\mu g1}$ is the commanded voltage of Microgrid 1. The transfer function $Z_{\mu g1}(s)$ represents the Thevenin impedance of Microgrid 1 as measured at the point of interconnection. A numerical approach for calculating the Thevenin impedance is described in Subsection 2.5.4.

Expressing a similar equation for Microgrid 2 and combining the two scalar equations into one matrix equation yields

$$\begin{bmatrix} \Delta v_{\mu g1} \\ \Delta v_{\mu g2} \end{bmatrix} = -\begin{bmatrix} Z_{\mu g1} & 0 \\ 0 & Z_{\mu g2} \end{bmatrix}\begin{bmatrix} \Delta i_{\mu g1} \\ \Delta i_{\mu g2} \end{bmatrix} + \begin{bmatrix} H_{\mu g1} & 0 \\ 0 & H_{\mu g2} \end{bmatrix}\begin{bmatrix} \Delta v^{*}_{\mu g1} \\ \Delta v^{*}_{\mu g2} \end{bmatrix} \tag{2.35}$$

The previous equation may be expressed symbolically as

$$\Delta \mathbf{v}_{\mu g} = -\mathbf{Z}_{\mu g} \Delta \mathbf{i}_{\mu g} + \mathbf{H} \Delta \mathbf{v}_{\mu g}^{*} \tag{2.36}$$

The transmission line equations can be expressed in transfer-function form as

$$\begin{bmatrix} \Delta i_{\mu g1} \\ \Delta i_{\mu g2} \end{bmatrix} = \begin{bmatrix} y_{11} & y_{12} \\ y_{21} & y_{22} \end{bmatrix} \begin{bmatrix} \Delta v_{\mu g1} \\ \Delta v_{\mu g2} \end{bmatrix} \tag{2.37}$$

which can be expressed symbolically as

$$\Delta \mathbf{i}_{\mu g} = \mathbf{Y}_{\mathrm{tl}} \Delta \mathbf{v}_{\mu g} \tag{2.38}$$

Here, $\mathbf{Y}_{\mathrm{tl}}$ it the transmission line admittance matrix. An analytical approach for calculating this matrix is described later in this document. The previous equations can be expressed in block-diagram form as shown in Figure 2-21, which depicts the relationships between the small-displacement voltages and currents at the points of interconnection.

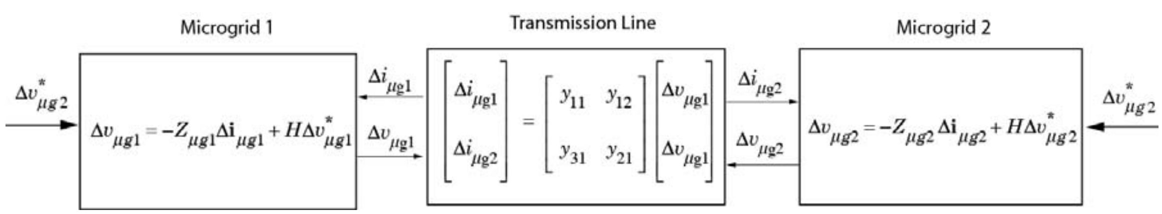

Figure 2-21 Block diagram illustrating relationships between voltages and current at point of interconnection.

Equations (2.36) and (2.38) can be combined into a single equation

$$\Delta \mathbf{i}_{\mu g} = -\mathbf{Y}_{\mathrm{tl}} \mathbf{Z}_{\mu g} \Delta \mathbf{i}_{\mu g} + \mathbf{Y}_{\mathrm{tl}} \mathbf{H} \Delta \mathbf{v}_{\mu g}^{*} \tag{2.39}$$

Rearranging,

$$\Delta \mathbf{i}_{\mu g} = \left[\mathbf{I} + \mathbf{Y}_{\mathrm{tl}} \mathbf{Z}_{\mu g} \right]^{-1} \mathbf{Y}_{\mathrm{tl}} \mathbf{H} \Delta \mathbf{v}_{\mu g}^{*} \tag{2.40}$$

The relationships between the voltages and currents at the points of interconnection can also be expressed in block-diagram form as shown in Figure 2-22, which is the traditional form for multi-input multi-output feedback systems.

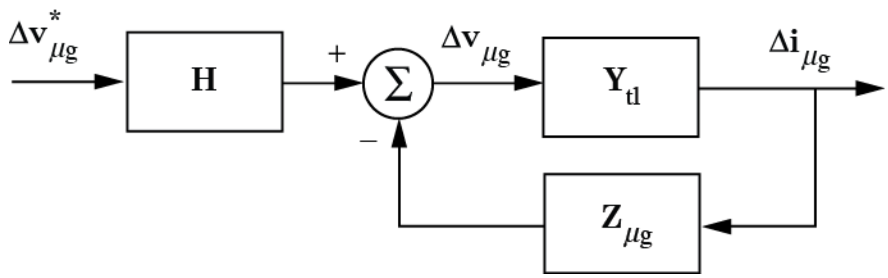

Figure 2-22 Transfer function block diagram illustrating relationships between voltage and currents.

2.5.2 Multivariable Nyquist Criterion

Assuming there are no open-loop uncontrollable and/or unobservable modes whose characteristic frequencies lie in the right-half plane, the closed-loop system in Figure 2-22 is stable if and only if the net sum of counter-clockwise encirclements of the critical point ($-1+j0$) by the set of characteristic loci of the return ratio $\mathbf{L}(s) = \mathbf{Y}_{\mathrm{tl}}(s)\mathbf{Z}_{\mu g}(s)$ it is equal to the total number of right-half plane zeros of $\mathbf{Y}_{\mathrm{tl}}(s)$ and $\mathbf{Z}_{\mu g}(s)$ [12]. The characteristic loci are established by plotting the eigenvalues of $\mathbf{L}(s) = \mathbf{Y}_{\mathrm{tl}}(s)\mathbf{Z}_{\mu g}(s)$ as s is varied from $-j\infty$ to $j\infty$.

2.5.3 Middlebrook-like Stability Criteria

If the characteristic loci are constrained to lie within the unit circle, there can be no counterclockwise encirclements and, assuming there are no right-half plane zeros of $\mathbf{Y}_{\mathrm{tl}}(s)$ and $\mathbf{Z}_{\mu g}(s)$, this will ensure stability. Although guaranteeing stability, it is not an absolute requirement for stability.

Consider the 2×2 return ratio matrix $\mathbf{L}$ at a fixed value of s. By Gershgorin's circle theorem [13], the eigenvalues will lie within circles centered at l_{11} and l_{22} in the complex plane with radii $\left|l_{12}\right|$ and $\left|l_{21}\right|$, respectively. If $\left|l_{ij}\right| < \frac{1}{2}$ for all i, j then all eigenvalues will lie within the unit circle. Considering

$$l_{ij} = \sum_{k=1}^{N} y_{ik} z_{kj} \tag{2.41}$$

Then

$$\left|l_{ij}\right| \leq \sum_{k=1}^{N} \left|y_{ik}\right| \left|z_{kj}\right| \leq \max_{1 \leq i \leq N} \sum_{j=1}^{N} \left|y_{ij}\right| \max_{j} \sum_{i=1}^{N} \left|z_{ij}\right| = \left\|\mathbf{Y}_{tl}\right\|_{\infty} \left\|\mathbf{Z}_{\mu g}\right\|_{1} \tag{2.42}$$

where $\left\|\mathbf{Z}\right\|_{1} = \max_{j} \sum_{i=1}^{N} \left|z_{ij}\right|$ (maximum absolute row sum) is the induced 1-norm and $\left\|\mathbf{Y}\right\|_{\infty} = \max_{i} \sum_{j=1}^{N} \left|y_{ij}\right|$ (maximum absolute column sum) is the induced infinity-norm. Consequently, if

$$\left\|\mathbf{Y}_{tl}\right\|_{\infty} \left\|\mathbf{Z}_{\mu g}\right\|_{1} \leq \frac{1}{2} , \tag{2.43}$$

the magnitude of characteristic loci will be less than 1 ensuring stability.

A similar criterion can be derived by defining the matrix "max" norm as $\left\|L\right\|_{\max} = \max_{i,j} \left|l_{ij}\right|$. By definition,

$$\left|l_{ij}\right| \leq \left\|\mathbf{L}\right\|_{\max} \tag{2.44}$$

By constraining

$$\left\|\mathbf{Y}_{tl}\right\|_{\max} \left\|\mathbf{Z}_{\mu g}\right\|_{\max} \leq \frac{1}{4} , \tag{2.45}$$

then, for a 2×2 return ratio matrix $\mathbf{L}$, it is readily shown using rules of multiplying matrices that $\left\|\mathbf{L}\right\|_{\max} \leq \frac{1}{2}$ whereupon the characteristic loci will again lie inside the unit circle.

Yet another criterion can be established using the result that the induced 2-norm of a matrix can be calculated as

$$\|\mathbf{L}\|_2 = \sigma_{\max}(\mathbf{L}) = \sqrt{\lambda_{\max}(\mathbf{L}^*\mathbf{L})} \tag{2.46}$$

where $\sigma_{\max}$ is the maximum singular value (principal gain) of $\mathbf{L}$ and $\lambda_{\max}$ is the maximum eigenvalue of $\mathbf{L}^*\mathbf{L}$. From linear algebra, the largest eigenvalue (spectral radius) of a matrix is less than $\sigma_{\max}$. Moreover, $\|\mathbf{YZ}\|_2 \le \|\mathbf{Y}\|_2 \|\mathbf{Z}\|_2$. Together, these results imply that if

$$\|\mathbf{Y}_{\mathrm{tl}}\|_2 \|\mathbf{Z}_{\mu g}\|_2 \le 1 \tag{2.47}$$

for all values of $s = j\omega$, the characteristic loci of $\mathbf{L}$ will lie inside the unit circle and the system will be stable.

Equations (2.43), (2.45), and (2.47) are similar but involve different matrix norms. The common theme, however, is that there is a tradeoff between the norms of the impedance and admittance matrices. That is, a large impedance norm means that the admittance norm must be small and vice versa. This is analogous to the classic Middlebrook criterion developed for single-input, single-output (scalar) systems.

Since $\mathbf{Z}_{\mu g}$ is diagonal,

$$\|\mathbf{Z}_{\mu g}\|_1 = \|\mathbf{Z}_{\mu g}\|_2 = \|\mathbf{Z}_{\mu g}\|_\infty = \max(|Z_{\mu g1}|, |Z_{\mu g2}|) \tag{2.48}$$

However, the same statement cannot be made regarding $\mathbf{Y}_{\mathrm{tl}}$. It was demonstrated in [14] that (2.47) (involving the 2-norm) is the least conservative of the three Middlebrook-like criteria described here. Therefore, the 2-norm will be used hereafter.

2.5.4 Numerical Calculation of $Z_{\mu g}$

A necessary initial step to the application of (2.47) is the determination of Thevenin impedance at the point of interconnection. Given a Simulink model of the microgrid, this can be accomplished numerically. The Simulink model may include any number of sources and loads however, it is important that average-value models are used to represent the power-electronic converters. The average-value models can be linearized about any state yielding a set of **A**, **B**, **C**, and **D** matrices that characterize the small displacement dynamics of the microgrid as observed from the point of connection. These matrices can be subsequently used to establish the Bode plot of $Z_{\mu g}$.

This procedure is automated in the Control System Design toolbox available through Mathworks. The user simply copies and pastes the "Bode Plot" tool into the Simulink workspace. Double-clicking on this block opens the dialog window depicted in Figure 2-23. The user then selects the appropriate input and output that, respectively, correspond to dc voltage and current at the point of interconnection. The user also specifies the instant of time at which linearization takes place.

Once the dialog entries are made, the user executes the model. At the time instant selected for linearization, the simulation pauses briefly, whereupon the linearized **A**, **B**, **C**, and **D** matrices are established by numerically perturbing states and inputs and calculating the resulting outputs and derivatives of state. This is done automatically without user intervention. By selecting "Show Bode Plot" in the "Algorithm-Options" field of the dialog window, the desired Bode Plot is drawn in a new figure window.

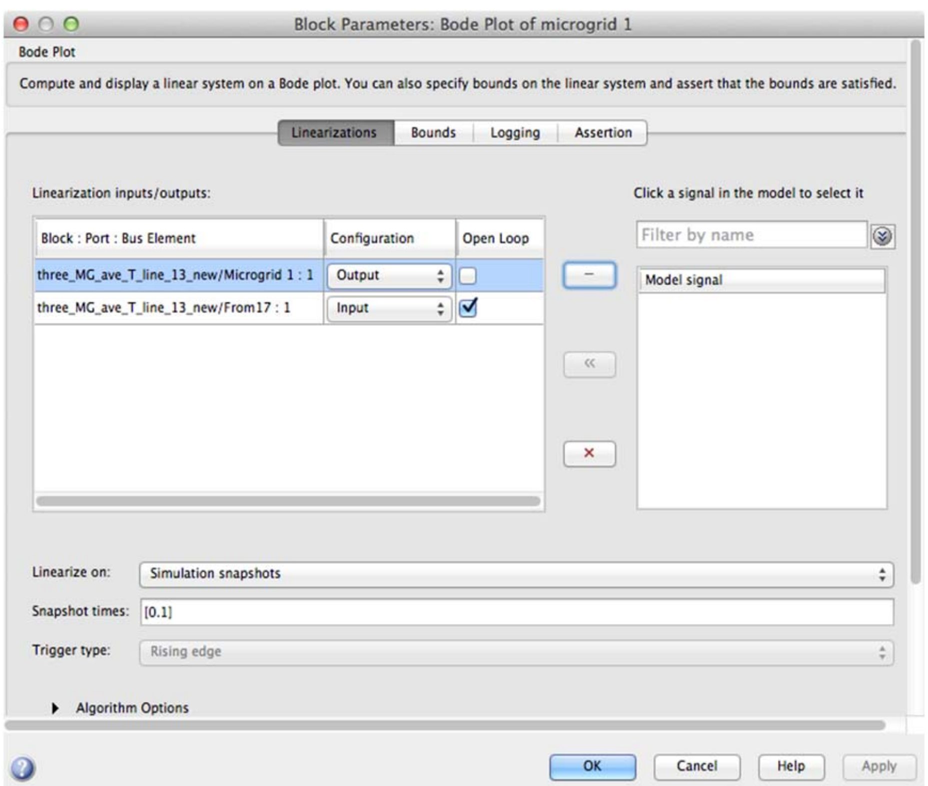

Figure 2-23 Dialog window for Simulink Bode Plot tool.

A sample Bode impedance plot is depicted in Figure 2-24. The selected microgrid is composed of a diesel generator with ARESE-B, a wind turbine generator with ARESE-B, a resistive load, and an ARESE-A. The microgrid components are described in [15]. The magnitude is plotted in db for reasons to be discussed shortly. That is, the Bode magnitude plot depicts $20\log\left|Z_{\mu g1}\right|$. Assuming Microgrid 2 is identical, the given Bode plot also represents the 2-norm of the Thevenin impedance matrix $\left\|\mathbf{Z}_{\mu g}\right\|_2$.

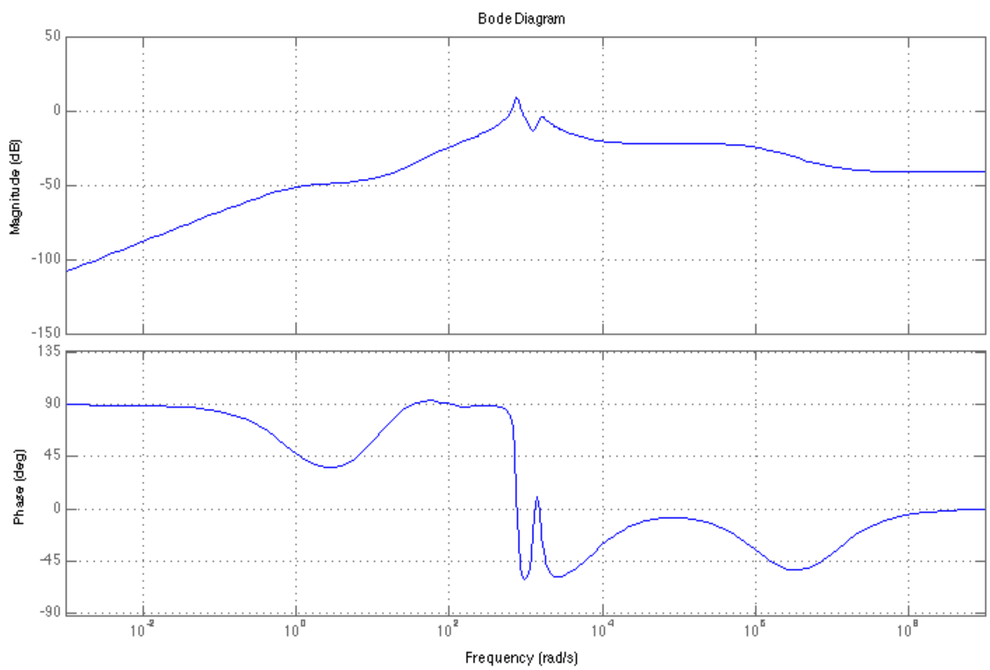

Figure 2-24 Bode plot of $Z_{\mu g}$.

The Thevenin impedance can also be established using detailed models by injecting a cyclic perturbation in current and measuring the corresponding cyclic perturbation in voltage for various frequencies; however, this approach is generally more time consuming since is involves potentially long run times, especially if the low-frequency impedance is to be established. Experimental measurement of the impedance is also feasible if hardware exists that is capable of injecting cyclic perturbations in current at the point of interconnection and measuring the resulting change in voltage.

2.6 Calculation of $\mathbf{Y}_{\mathrm{tl}}$

Although the transmission line admittance matrix can also be established using the Bode Plot tool, an analytical approach is possible and preferable (for accuracy purposes) using the frequency-domain solution of the classic transmission line equations. As documented in Appendix A, the relationship between voltage and currents can be expressed in the frequency domain as

$$i_L = v_L \frac{\coth \gamma d}{Z_c} - v_R \frac{1}{Z_c \sinh \gamma d} \tag{2.49}$$

$$i_R = -v_L \frac{1}{Z_c \sinh \gamma d} + v_R \frac{\coth \gamma d}{Z_c} \tag{2.50}$$

where

$$\gamma = \sqrt{(R + j\omega L)(G + j\omega C)} \tag{2.51}$$

is the propagation constant and

$$Z_c = \sqrt{\frac{R + j\omega L}{G + j\omega C}} \tag{2.52}$$

is the characteristic impedance. Here R, L, G, C are the series resistance, series inductance, shunt conductance, and shunt capacitance per unit length, respectively. These line parameters may be a function of frequency. Since the equations are linear, they also apply to small-displacement voltages and currents. Hence,

$$\mathbf{Y}_{tl} = \frac{1}{Z_c} \begin{bmatrix} \coth \gamma d & \operatorname{csch} \gamma d \\ \operatorname{csch} \gamma d & \coth \gamma d \end{bmatrix} \tag{2.53}$$

The calculation of $\left\|\mathbf{Y}_{\mathrm{tl}}\right\|$ can be achieved using a simple Matlab™ script and is depicted in Figure 2-25 for a line whose parameters are: $d = 100\,\mathrm{km}$, $L = 0.1667\ \mu\mathrm{H/m}$, $C = 66.67\,\mathrm{pF/m}$, $R = 10\,\mu\Omega/\mathrm{m}$, and $G = 0$. The 2-norm of the admittance matrix for a 1-km line with the same parameters is depicted in Figure 2-26. As shown, admittance norm is much larger at low frequencies, which means that the Thevenin impedance norm must be much smaller if the Middlebrook-like criterion is to be satisfied.

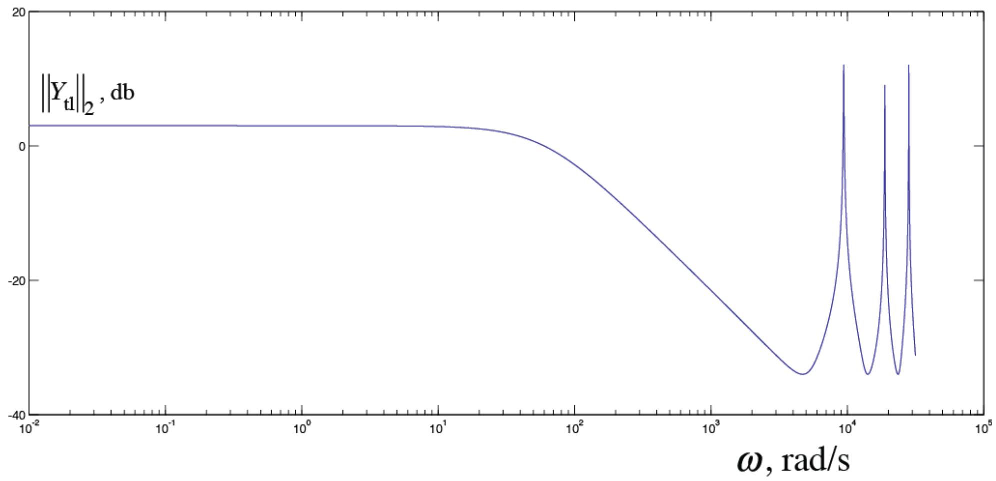

Figure 2-25 Admittance norm for transmission line with parameters: $d = 100\,\text{km}$, $L = 0.1667\ \mu\text{H/m}$, $C = 66.67\,\text{pF/m}$, $R = 10\,\mu\Omega/\text{m}$, $G = 0$.

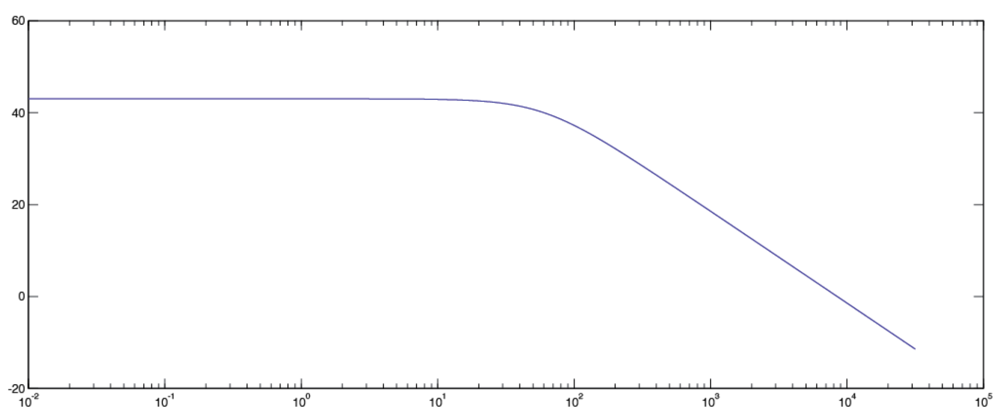

Figure 2-26 Admittance norm for transmission line with parameters: $d = 1\,\text{km}$, $L = 0.1667\ \mu\text{H/m}$, $C = 66.67\,\text{pF/m}$, $R = 10\,\mu\Omega/\text{m}$, $G = 0$.

2.6.1 Stability Analysis

The sum of the magnitude plots in Figure 2-24 and Figure 2-25 represents the product $\left\|\mathbf{Y}_{\mathrm{tl}}\right\|_2 \left\|\mathbf{Z}_{\mu g}\right\|_2$ when expressed in db. It is primarily for this reason that the magnitudes are plotted in db. At low frequencies, $\left\|\mathbf{Y}_{\mathrm{tl}}\right\|_2 \approx 5\,\mathrm{db}$ and $\left\|\mathbf{Z}_{\mu g}\right\|_2 \approx -100\,\mathrm{db}$. When $\left\|\mathbf{Z}_{\mu g}\right\|_2$ reaches its maximum of approximately 0 db, $\left\|\mathbf{Y}_{\mathrm{tl}}\right\|_2 \approx -20\,\mathrm{db}$. It is apparent by inspection that the sum is always less than 0 db implying that $\left\|\mathbf{Y}_{\mathrm{tl}}\right\|_2 \left\|\mathbf{Z}_{\mu g}\right\|_2 < 1$ for all frequencies. This, in turn, implies that the interconnected system will be stable.

However, if the shorter line is used to interconnect the two microgrids, the magnitude plots in Figure 2-24 and Figure 2-26 should be summed. At a frequency of approximately 100 rad/s, $\left\|\mathbf{Z}_{\mu g}\right\|_2 \approx -25\,\mathrm{db}$ while $\left\|\mathbf{Y}_{\mathrm{tl}}\right\|_2 > 40\,\mathrm{db}$. Thus, $\left\|\mathbf{Y}_{\mathrm{tl}}\right\|_2 \left\|\mathbf{Z}_{\mu g}\right\|_2 > 1$ near this frequency. This does not necessarily mean that the interconnected system will be unstable since (2.47) is sufficient but not necessary. Rather, stability for this case is indeterminate using this criterion. Instead, the more general Nyquist criterion must be used to determine whether an encirclement of the critical point exists.

2.6.2 Conclusions

From the previous analysis, it should be apparent that a long line is desirous from the standpoint of stability since the associated admittance norm will be small. A short line is potentially problematic since it can give rise to interactions between the voltage regulators of the two microgrids. Since short lines will generally lead to violation of the Middlebrook-like criteria described in this document, a more comprehensive analysis is necessary using, for example, the sufficient and necessary multivariable Nyquist criterion. However, for short lines, potentially unstable interactions can be mitigated by placing a dc/dc converter at either end of the line and using the duty cycle signal to control the current flow through the line. Within the bandwidth of the current regulator, the admittance norm essentially becomes zero, effectively decoupling the dynamics of the two microgrids.

3 AC MICROGRIDS

An example ac microgrid is depicted in Figure 3-1, which includes all of the components of the dc microgrid depicted in Figure 2-6; however, each component includes a dc-to-ac inverter that interfaces an intermediate dc but to a common ac bus. A brief description of the microgrid components is provided in the following paragraphs.

Power/Energy Management System (PEMS)

The PEMS is responsible for monitoring the status of the micro-grid and scheduling the sources accordingly. It is also responsible for shedding loads if the power/energy supply cannot meet the demand. This subsystem is analogous to the area control center of an electric utility in the conventional power system.

Energy Storage Unit (ESU)

The ESU is comprised of a battery connected to a regulated dc bus through a dc-to-dc converter. The dc bus voltage is regulated by adjusting the duty cycle of the dc-to-dc converter. The regulated dc voltage is then converted to three-phase ac through an inverter using the control strategy described in the previous section. The power supplied by or injected into the battery is controlled by the scheduled command P_{sched}.

Diesel Generator (DG)

The DG is comprised of a diesel engine connected to an ac generator whose output voltages are rectified using a diode bridge rectifier. The rectified dc voltage is regulated by adjusting the voltage applied to the field winding of the ac generator. The speed of the diesel engine is regulated by the engine's governor, which controls the fuel supply. As in the ESU, the regulated dc voltage is converted to three-phase ac using a dc-to-ac inverter and control strategy similar to that described in the previous section.

Photovoltaic Generator (PVG)

The PVG is comprised of a photovoltaic array connected to a regulated dc bus through a dc-to-dc converter. Unlike the previous components, the PVG does not participate in regulation of the bus voltage. The duty cycle of the dc-dc converter is adjusted so that the voltage appearing across the array maximizes the extracted power. The optimum duty cycle is determined using a peak-power tracking control [16], [17]. The array power is injected into the ac system through the inverter. Although not essential, it is assumed here that the reactive power supplied by the inverter is zero, i.e. the PVG does not participate in the regulation of the ac voltage.

Wind Turbine Generator (WTG)

The WTG is comprised of a wind turbine connected to a permanent-magnet ac machine whose output is rectified using a diode bridge. Since the turbine speed will vary as a function of wind speed, the rectified output voltage will vary correspondingly. The rectified output voltage is connected through a boost converter to a regulated dc bus. The duty cycle of the boost converter is controlled so as to maximize the power extracted from the wind as described in [18]. This power is injected to the ac system through the inverter. As in the PVG, it is assumed that the reactive power supplied by the inverter is zero, i.e. the WTG also does not participate in the regulation of the ac voltage.

Asynchronous Loads (ALs)

ALs are those loads that do not require special considerations for synchronization. These include induction machines, diode bridge rectifier loads, lighting loads etc. ALs consume real power and typically consume reactive power. The asynchronous loads are switched in and out as decided by exogenous user demand. From the preceding descriptions, it should be apparent that the PVG and WTG are non-dispatchable sources. That is, under normal operating conditions, maximum power is extracted from the sun and wind and that no reactive power is supplied or consumed by either source. In subsequent discussions, the system or overall base power is selected to be the sum of the power ratings of dispatchable sources.

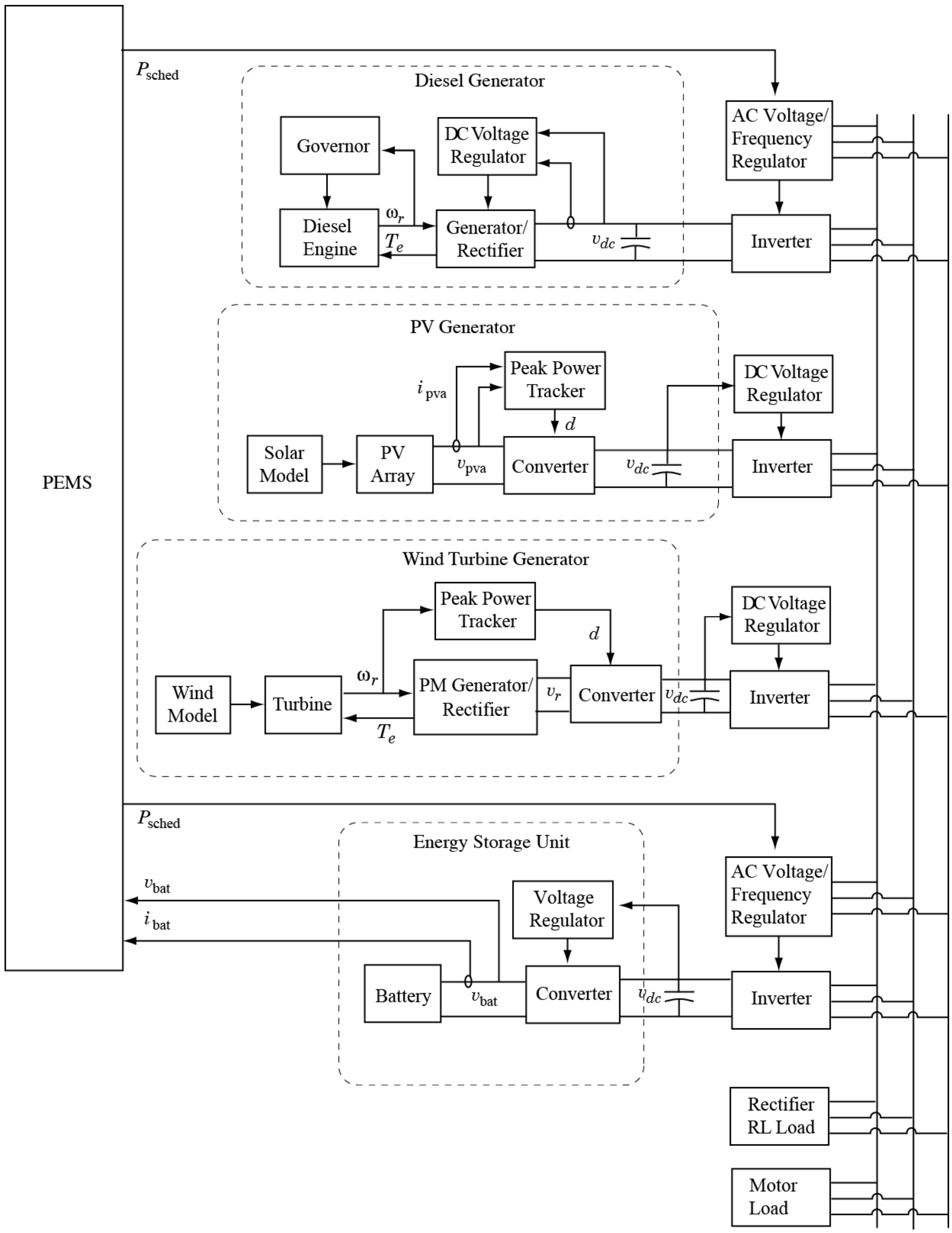

Figure 3-1 Example ac microgrid.

3.1 Stability and Control of AC Systems

As in the dc case, there are many potential modes of operation and control strategies for the given system. In ac systems, the situation is more complex since it is necessary to regulate both the amplitude and the frequency of the ac voltage. In this section, the techniques of controlling and analyzing the stability of ac systems is reviewed.

3.1.1 Nyquist Stability

In order to analyze multivariable systems with methods similar to single-input single-output systems, a generalized form of the Nyquist Criteria was developed by MacFarlane and Postlethwaite [12]. The generalized Nyquist Criteria states that a system with the general transfer function

$$\mathbf{y}(s) = [\mathbf{I} + \mathbf{G}(s)\mathbf{K}(s)]^{-1}\mathbf{K}(s)\mathbf{u}(s) \tag{3.1}$$

will be closed-loop stable if and only if the net counter-clockwise encirclements of the point $(-1 + j0\ )$ by the characteristic loci of $\mathbf{L}(\mathbf{s})$ = $\mathbf{G}(\mathbf{s})\mathbf{K}(\mathbf{s})$ is equal to the number of RHP poles of $\mathbf{G}(s)$ and $\mathbf{K}(s)$. The characteristic loci are defined as the contours of $\lambda_i(s)$, the eigenvalues of $\mathbf{L}(s)$, as s traverses the Nyquist contour.

To examine the stability criteria for ac power systems, it is important to understand the general layout of such systems such as in Figure 3-2. This simple ac system consists of a filtered three-phase source and a regulated load with commanded real and reactive power values, P and Q.

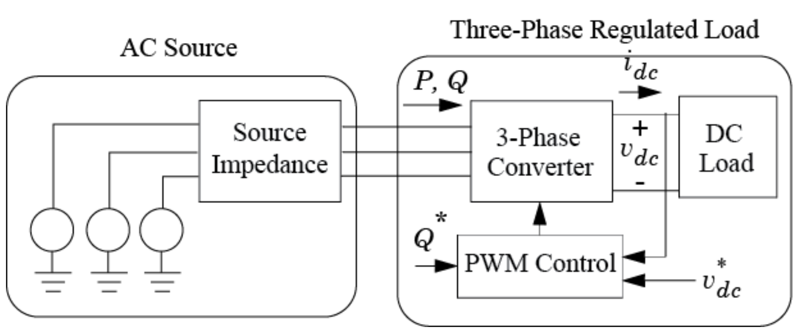

Figure 3-2 Simple ac system.

In the synchronous reference frame linearized around some operating point, the small-displacement load characteristics can be expressed in the form

$$\Delta\mathbf{i}_{qd}^{e} = \mathbf{Y}_L \Delta\mathbf{v}_{qd}^{e} \tag{3.2}$$

where $\Delta\mathbf{i}_{qd}^{e}$ is the change in the *qd*-axis currents, $\Delta\mathbf{v}_{qd}^{e}$ is the change in *qd*-axis bus voltages, and $\mathbf{Y}_L$ is the frequency-dependent load admittance matrix and can be related to the load properties as outlined in [8].

Regulated loads or loads with controlled power-electronic converters may exhibit a negative impedance characteristic for a range of frequencies that may, in turn, lead to instabilities. In a limiting case, the load may be approximated as a constant–power load, i.e., one in which the load power does not change even if the bus voltage changes. The situation is somewhat more complex in ac systems in the sense that there are two components of power, real and reactive. If the real and reactive components of power are user-supplied inputs, changes in the corresponding *q*- and *d*-axis components of load current may be calculated as

$$\Delta i_{qL} = \frac{\Delta v_q P_L - \Delta v_d Q_L}{v_q^2 + v_d^2} \tag{3.3}$$

$$\Delta i_{dL} = \frac{\Delta v_d P_L + \Delta v_q Q_L}{v_q^2 + v_d^2} \tag{3.4}$$

Thus, the corresponding load admittance matrix may be expressed

$$Y_L = \frac{1}{v_q^2 + v_d^2}\begin{bmatrix} P_L & -Q_L \\ Q_L & P_L \end{bmatrix} \tag{3.5}$$

which is independent of frequency.

The ac source can be modeled in the synchronous reference frame, after being linearized, with the matrix equation

$$\Delta\mathbf{v}_{qd}^{e} = \mathbf{Z}_S \Delta\mathbf{i}_{qd}^{e} + \mathbf{H}\Delta\mathbf{v}_{qdS}^{e} \tag{3.6}$$

where $\mathbf{v}_{qdS}^{e}$ is the qd-axis Thevenin-equivalent source-voltage vector, $\mathbf{Z}_S$ is the frequency-dependent source impedance matrix and $\mathbf{H}$ is a transfer function matrix that models the dynamics of the filter on the open-circuit voltages. Replacing (3.2) into (3.6) results in the equation

$$\Delta\mathbf{v}_{qd}^{e} = [\mathbf{I} + \mathbf{Z}_S\mathbf{Y}_L]^{-1}\mathbf{H}\Delta\mathbf{v}_{qdS}^{e} \tag{3.7}$$

In block notation, (3.7) is equivalent to Figure 3-3. The generalized Nyquist criterion can be applied to this system to show that if the source and load are individually stable, the system will be stable if the characteristic loci generated by the eigenvalues of $\mathbf{Z}_S\mathbf{Y}_L$ do not encircle the point ($-1 + j0$).

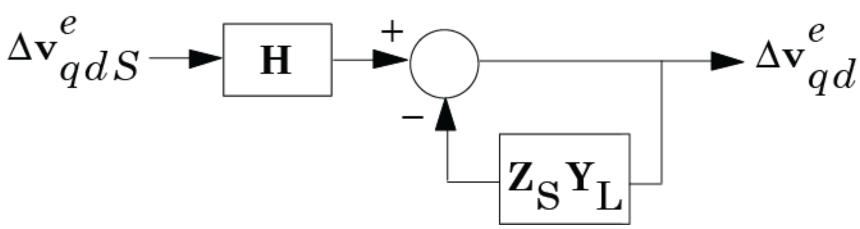

Figure 3-3 Transfer function block diagram for ac stability analysis.

As in the dc case, the generalized Nyquist criteria, while providing a useful graphical representation of system stability, does not relate that stability to the design parameters in a way that can lead to design specifications. To rectify this, an analog to the Middlebrook criteria was developed in [14], herein referred to as the Belkhayat criteria. This criteria ensures that the eigen-loci will not encircle ($-1 + j0$) provided

$$\sigma\big(\mathbf{Z}_S(\omega)\big)\sigma\big(\mathbf{Y}_S(\omega)\big) < 1 \ \ \forall\omega \tag{3.8}$$

where $\sigma\big(\mathbf{Z}_S(\omega)\big)$ and $\sigma\big(\mathbf{Y}_S(\omega)\big)$ are the largest singular value of the respective signal, also called the principle gain. Since all eigenvalues of the matrix must be smaller than the principle gain, this provides a more direct design procedure for ensuring small-displacement stability in ac systems. Equation (3.8) is analogous to the Middlebrook criterion commonly used in dc systems.

3.1.2 Droop-based Frequency /Voltage Regulation in Conventional Ac Systems

Prior to the discussion of regulation strategies in microgrids, it is worthwhile to review briefly the operating principles of the conventional power grid. In the steady state, all generators must operate at the same frequency, which is typically proportional to the corresponding speeds. Each generator includes a speed governor that controls the flow of steam or water to the turbine prime mover, which includes a droop characteristic such that the rotor speed decreases as the real output power increases as shown in Figure 3-4. The slope of the speed-versus-power characteristic is called the droop R_f and is typically set to 5% in North America.

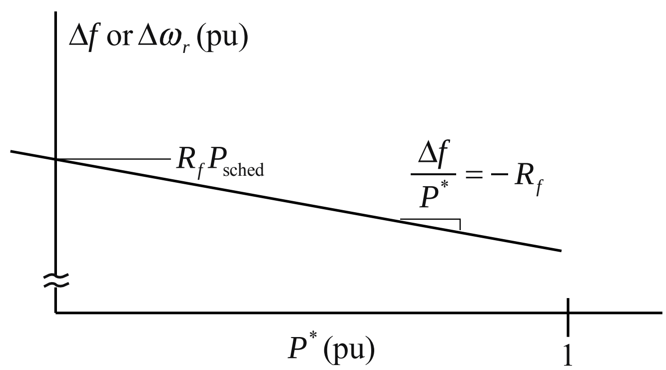

Figure 3-4 Speed/Frequency droop characteristic of typical generator.

If all generators in an interconnected grid have the same droop setting and a sudden change in net load power (ΔP_L) occurs, the output power of each generator will increase in proportion to it's rating such that the net increase in generation will equal ΔP_L. In other words, the per unit (pu) change in output power for each generator will be the same in the absence of any change in externally applied signals. The frequency will decrease by $\Delta f = R_f \Delta P_L$ where Δf and ΔP_L are typically expressed in pu. For example, if $R_f = 0.05$ and rated load is suddenly applied to a generator, the speed/frequency will decrease by 5% = 0.05 pu.

In order to restore the frequency back to 60 Hz, a supervisory layer of control is used, which is commonly called automatic frequency control (AFC). This layer is much slower in reacting to changes in supply and/or demand and involves the sampled acquisition of voltages, currents, power flows, frequencies, and/or angles throughout the system. If the area frequency is less than 60 Hz, incremental bias signals are sent to selected generators that raise the frequency-versus-power characteristics without changing the droop (slope). A redistribution of generated power can be affected at the supervisory layer by raising the bias signals for some generators, while lowering it in others. The advantage of this structure is that the system can continue to operate, albeit sub-optimally, if the supervisory control center is disabled due to natural or manmade disasters.

Due to the variability of loads, there is never an exact match between the generated power and the power consumed by loads. If the generated power exceeds that consumed by the loads, the speed (frequency) increases and vice versa. The power mismatch over the short term is made up by taking energy from or putting energy into the kinetic energy of the system as a whole. The rotating masses represent a form of energy storage. As the generators correspondingly slow down or speed up, the associated speed governors autonomously adjust the steam or fuel flow to prevent over- or under-speed conditions. In the absence of any other control action, the frequency of a synchronous grid will vary as a function of the load/generation mismatch. As mentioned, these frequency variations are corrected at the supervisory level by power system operators that can change the scheduling (power commands) of the generators in the system, bringing additional generators on line, or shutting off unnecessary generation.

As dictated by the North American Reliability Corporation (NERC), operators are typically required to maintain a 5% spinning reserve to accommodate sudden changes in load or the loss of a generating plant. If, hypothetically, all variations in load are very slow and uniformly distributed throughout the system, the frequency, although changing due to the ever-present mismatch between generation and load, will be the same throughout the system due to the electromagnetic synchronizing torques that exist between the synchronous generators. If however, there is a local disturbance such as the sudden loss of a load/generator within an area, the speeds of the generators will deviate from one another during the ensuing transients. If the resulting angle between generators (time integral of the difference in frequencies) exceeds a critical value, the synchronizing torques can actually become destabilizing, causing additional generators to lose synchronism and subsequently trip off line. This consequential event generally results in a larger power mismatch, causing further transient deviations in speed/frequency, and potentially the cascading loss of generation across a very large area [19].

In addition to the regulation of frequency, it is also imperative to regulate voltage amplitudes. When multiple ac sources, each with output voltage regulators, are connected in parallel, the potential for instabilities exists since all of the sources are attempting to regulate the same voltage [20]. To avoid voltage instabilities, a voltage-versus-reactive-power droop characteristic such as that shown in Figure 3-5 can be used [21]. Therein, the commanded voltage V^* is decreased in proportion to the reactive power being supplied by the ac source. Equivalently, a current-dependent compensating voltage can be added to the measured voltage before it is subtracted from the set-point value [22]. If the voltage droop setting (slope = R_V) is the same in all sources, each provides reactive power in proportion to its rating with the net reactive power corresponding to that needed to support the desired ac voltage. This prevents the ac sources from fighting each other in an attempt to regulate the same bus voltage. As in real power control, the redistribution of reactive power among sources may be accomplished by setting the voltage droop or scheduled voltage for each source individually.

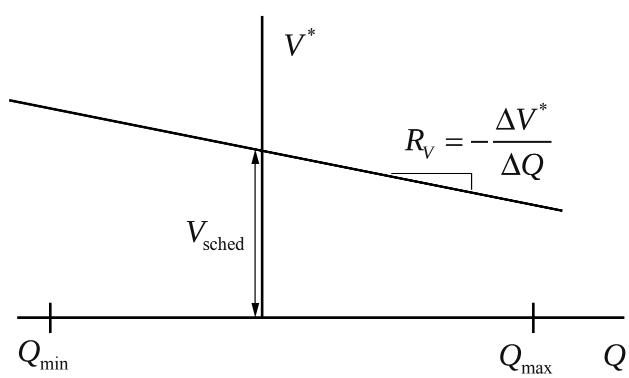

Figure 3-5 Voltage droop in an ac system.

3.1.3 Frequency/Voltage Regulation in AC Micro Grids

It is useful to review the fundamental relationships that relate real and reactive power flow to voltage amplitudes, frequencies, and/or phase angles. A prototypical dc-to-ac inverter is depicted in Figure 3-6. Therein, the sensing block measures the instantaneous voltage and currents and calculates the real and reactive power (P_L and Q_L). The sensing block also includes a phase locked loop (PLL) to establish the frequency f, instantaneous angle θ_V, and amplitude V of the ac voltages. The steady-state relationships between the inverter and bus voltage amplitudes and the real and reactive power supplied by the inverter may be approximated as [23]

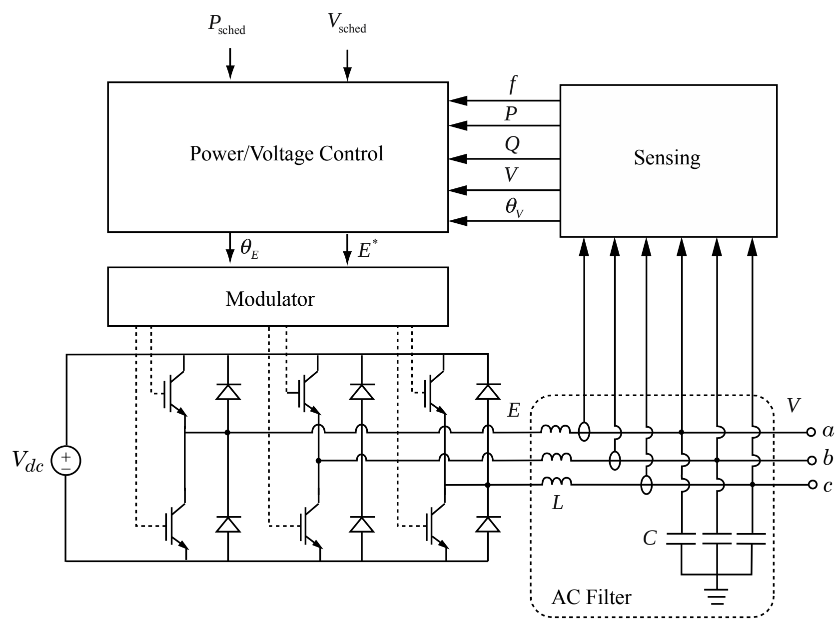

Figure 3-6 Circuit/block diagram of prototypical inverter.

$$P \approx \frac{VE}{X} \sin\delta \tag{3.9}$$

$$Q \approx \frac{E}{X}(E - V\cos\delta) \tag{3.10}$$

where $X = \omega_e L$ is the inductive reactance of the ac filter, E is the fundamental amplitude of the voltages on the inverter side of the ac filter (Figure 3-6) and

$$\delta = \theta_E - \theta_V \tag{3.11}$$

is the angle between the voltages on the inverter and ac bus sides of the ac filter. In the steady state, δ is constant. The voltage E can be set rapidly to any desired value between zero and an upper limit that is a function of the dc voltage and the modulation strategy used. The control of real and reactive power may be accomplished as follows. To control the active or real power supplied by the inverter, the measured power P is compared with the commanded power P_{sched} as shown in Figure 3-7. The difference is supplied to a Proportional-Integral-Derivative (PID) control that advances or delays the instantaneous phase signal θ_E by δ relative to the measured θ_V, the latter of which is established using the PLL. From (3.9), advancing (delaying) the phase angle δ increases (decreases) the output power. The droop compensation block in Figure 3-7 is discussed in the following section.

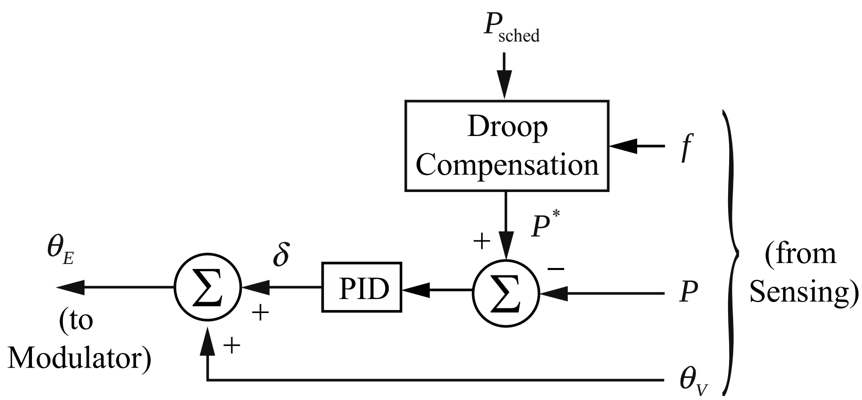

Figure 3-7 Inverter real power control.

The voltage amplitude V can be controlled as shown in Figure 3-8, wherein the measured amplitude V is compared to the commanded value V^*. The difference is supplied to a PID controller that adjusts the commanded voltage E^* on the inverter side of the ac filter. The droop compensation block in Figure 3-8 is discussed in the following section.

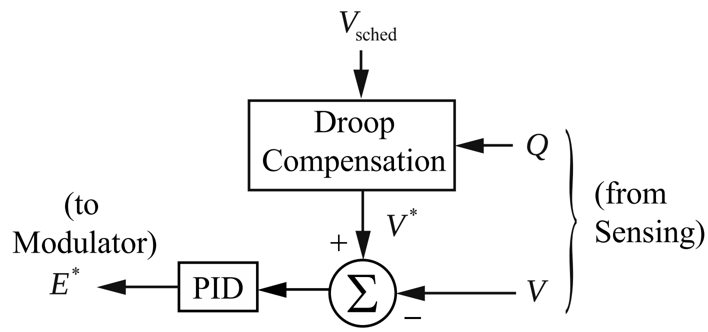

Figure 3-8 Inverter voltage control.

Finally, the modulator converts the instantaneous angle θ_E and commanded amplitude E^* to transistor switching (gating) signals using, for example, a space vector or sine-triangle strategy as described in [8].

Unlike the conventional bulk power grid, an ac micro-grid includes only a small number of sources and loads that may or may not be interconnected into the bulk power grid. For purposes of discussion, it is assumed that a specific isolated micro-grid consists of a diesel-engine-driven generator, a battery energy storage unit, a photovoltaic generator, a wind turbine generator, a diode bridge rectifier connected to a passive dc load, and a motor load. A block diagram of the example micro-grid utilizing droop control is depicted in Figure 3-9.

Droop-Based Frequency Voltage Regulation

At this point, it is possible to describe a frequency/voltage regulation paradigm analogous to that of the conventional power grid. The example micro-grid has two dispatchable sources (DG and the ESU) and two non-dispatchable sources (PVG and the WTG), which may be viewed as negative loads. If the micro-grid is isolated from the bulk power grid and the net load power (total power consumed by ALs less total power generated by non-dispatchable sources), the difference must be supplied by the dispatchable sources in any combination that does not violate any constraints. For example, it the battery SOC is close to zero, the net load power must be supplied by the

DG. If the DG is low on fuel, the net load power must be supplied by the ESU. If the fuel level is low and the SOC is close to zero, it becomes necessary to shed loads.

The proportion of net load supplied by each dispatchable source is determined by the PEMS through the scheduling commands P_{sched}. If the scheduled power does not match the net load power, the frequency will deviate from 60 Hz by $R_f \Delta P_L$ where ΔP_L is the difference between total scheduled and net load power. If the frequency is low (high), the scheduled power can be increased (decreased) to raise (lower) the frequency as in the AFC system of conventional grids.

If a positive change in net load power occurs, the frequency will decrease by $R_f \Delta P_L$. The power supplied by each dispatchable source will increase in proportion to its rating. If it is desired to alter the ratio, the regulation R_f can be set individually for each generator. For example, if it is desirable for a particular generator to supply a larger portion of the change in load (relative to its rating), the corresponding R_f can be decreased. In the absence of such a desire, the regulation R_f would be set to the same value for all sources. In the steady state, the distribution of power among dispatchable sources can also be adjusted through the scheduled power command signals.

Finally, if the net load power is negative, the battery must absorb the excess since the DG can only supply power. If, additionally, the battery SOC is close to 1, it becomes necessary to shut off or reduce the power supplied by the non-dispatchable sources, which results in an apparent contradiction in terminology. This contradiction may be resolved by altering the definition of non-dispatchable sources to be those sources that do not participate in the regulation of bus frequency or voltage.

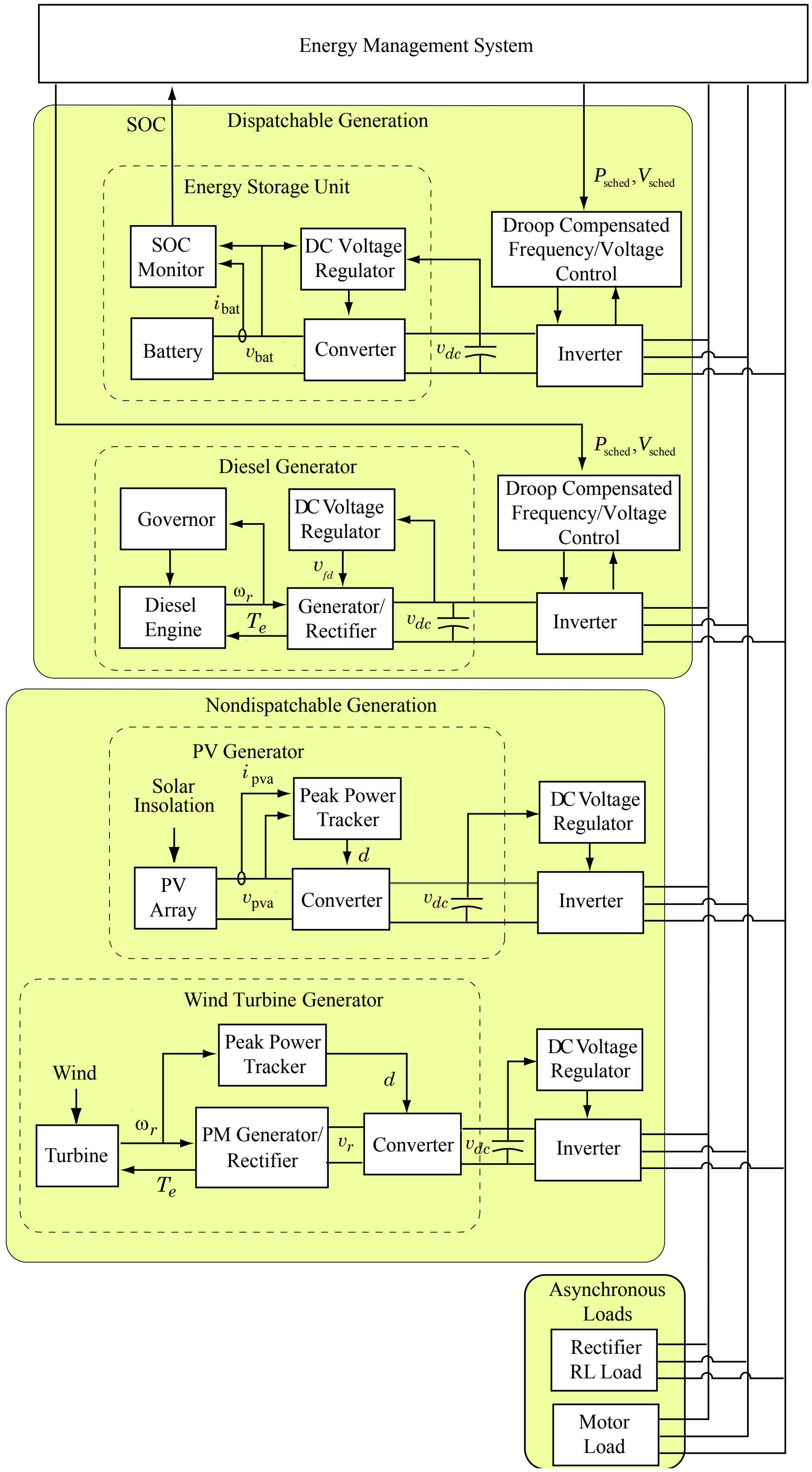

Figure 3-9 Example microgrid with droop-based voltage/frequency control.

Alternative Frequency/Voltage Regulation Paradigms

If the micro-grid control system is patterned after the conventional grid and a disturbance occurs such as a sudden change in load or the loss of a source, the frequency will not be constant nor uniform during the ensuing transients. Instead, oscillations in the frequencies of and angles between inverter output voltages will occur due to dissimilarities in the dynamic response characteristics of the corresponding sources. If the angular displacements become too large, transient instabilities can occur wherein synchronization is lost among micro-grid components very likely leading to a total blackout. Restoring the micro-grid to an active state can be accomplished by programming a black-start procedure into the PEMS. Finally, it should be noted that, unlike the conventional grid, frequency droop does not provide an apparent stability-related benefit since absorbing the power mismatch through the kinetic energy of rotating generators is not feasible unless the sources are rotating generators.

Due to the close proximity of all components in the microgrid, it would appear that a more direct approach of maintaining synchronism would be to broadcast a timing signal that synchronizes the switching waveforms of all inverters as shown in Figure 3-10. This completely eliminates the threat of transient instabilities; synchronization of inverter output voltages is essentially guaranteed. This timing signal could be broadcast by the PEMS using a wired or wireless local area network. Although this approach may appear to add complexity, it can be argued that it actually reduces complexity since it completely eliminates the need for any source (dispatchable or non-dispatchable) to include a PLL in its Sensing block. It also simplifies analysis by eliminating the state variables associated with the PLLs, which influence the overall dynamic response.

Although frequency regulation is no longer an issue in the system of Figure 3-10, it is still necessary to regulate the amplitude of the ac voltages. This can be accomplished using the voltage control strategy set forth in [25]. Therein, a hysteresis modulator is used in conjunction with a feedback/feedforward control strategy that precisely regulates the amplitude of the ac bus voltages, which was shown to be very robust with respect to system disturbances. To minimize transients on the dc side of the inverter, the control strategy in [25] should be applied to the BESU since it is the fastest acting dispatchable source. In this case, the BESU can be referred to as the slack generator, since its power will be equal to the difference between net load and total generation, excluding the BESU.

In Figure 3-10, the DG power is scheduled by the PEMS; however, it is no longer necessary to include a droop compensator since frequency is fixed throughout the micro-grid. That is, the inverter commanded power P_{sched} is directly set to the scheduled power. The reactive power supplied by the DG can be set to zero or to a value that minimizes inverter losses. The control systems for the non-dispatchable sources are similar to those described previously with the exception that PLLs are not needed. The switching frequencies are synchronized by a signal completely separate from the ac bus.

In this approach, long-term energy management is accomplished by scheduling the DG. If the battery SOC is low and non-dispatchable generation is less than net load, the DG is scheduled so that there exists a net excess that flows into the BESU to charge the battery. If the non-dispatchable generation exceeds net load, the DG can be turned off and excess generation continues to flow into the BESU charging the battery. If the SOC approaches 1, the DG is off, and a net excess of generation persists, it becomes necessary to reduce the power supplied by non-dispatchable sources. Variations to the preceding approach are possible. For example, the DG may be selected as the slack generator and the ESU as the dispatchable generator. However, sudden change in load may cause larger transients to occur on the associated dc bus since the diesel engine is slower acting. Intuitively, the fastest-acting source should be selected as the slack generator. Finally, whenever the micro-grid is connected into the bulk power grid, the PEMS may be designed so that the local clock frequency and voltage command signal for the slack generator exhibit conventional droop characteristics. Intuitively, this would lessen the impact that a growing penetration of distributed micro-grids might otherwise have on the bulk power system.

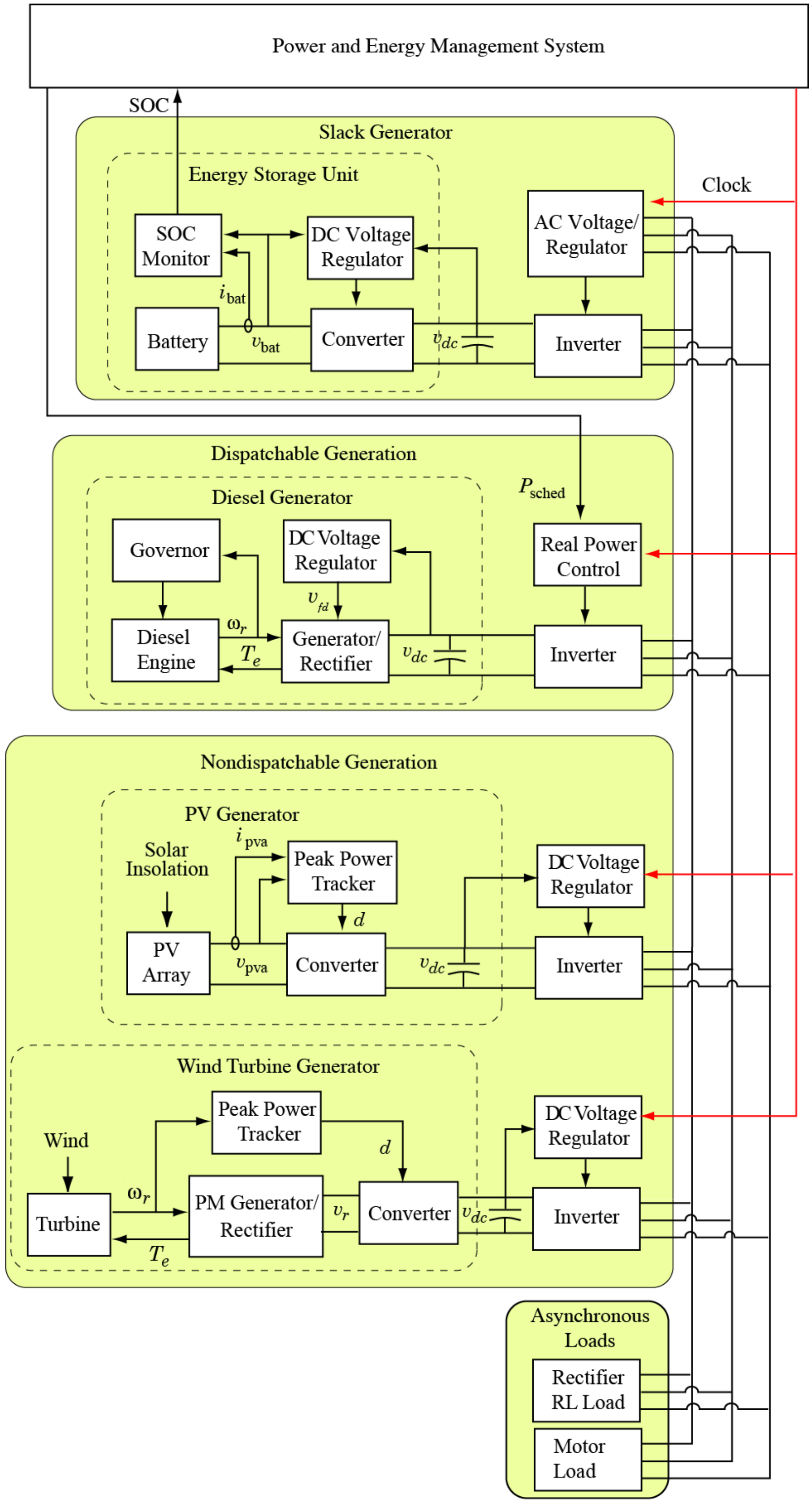

Figure 3-10 Alternative voltage regulation paradigm.

3.1.4 Large-Displacement Stability

As in the case of dc systems, guaranteeing small-displacement stability, albeit over a range of operating conditions, does not guarantee stability following large disturbances such as pulsed loads, faults, component failures, or simply the connection/disconnection of large loads. Recently, a design paradigm was developed with the goal of guaranteeing large-displacement stability of dc power systems containing a significant penetration of regulated (constant-power) loads for any value of load power up to and including the steady-state rating of the source [24]. This paradigm has subsequently been extended to ac systems as described in the following paragraphs.

A single-source single-load ac system is depicted in Figure 3-11. The source consists of a regulated dc-to-ac inverter whose output voltage is regulated (frequency and amplitude) using a strategy set forth in [25]. The main parameters of this source/control are: (1) V_{dc} - the dc supply voltage, (2) h the hysteresis level in the current control, (3) L the ac filter inductance, and C - the ac filter capacitance. The load is assumed to be an ideal *PQ* load. That is, the real and reactive power consumed by the load is equal to the commanded values P_L and Q_L. It is reasonable to ask the question: Is possible to select a set of inverter parameters such that the ac system is stable for ***any*** step change in real and reactive power within a circle whose radius corresponds to rated inverter power as shown in Figure 3-12. For generality, it is useful to use per unit notation. In per unit, the radius of the circle in Figure 3-12 is unity. If the answer to the preceding question is affirmative, the next question to ask is: For the selected parameters, are the parameter values practicable? It appears that the answer to both of these questions is yes.

To support the previous statement, a detailed simulation of the system in Figure 3-11 was developed. To reduce the parameter space, the hysteresis level was set to a value of 0.05 pu, which is commensurate with existing designs. The free parameters include: X_{Lac} - inductive reactance, X_{Cac} capacitive reactance, and V_{dc} - the supply voltage. A contingency set composed of eight step changes in P_L and Q_L in was selected as shown in Figure 3-11. This set includes step change in both P_L and Q_L starting from a point on the unit circle to another point diametrically opposite. For this contingency set, the stability boundary was established by repeatedly executing the detailed simulation as the free parameters are varied. The stability boundary is plotted as a family of curves as shown in Figure 3-13 wherein V_{dc} is plotted as a function of X_{Lac} for various values of X_{Cac}. For a selected X_{Lac} and X_{Cac}, there is a minimum V_{dc} needed to maintain stability for all step changes in the contingency set. As expected the minimum V_{dc} is larger for larger values of X_{Lac}.

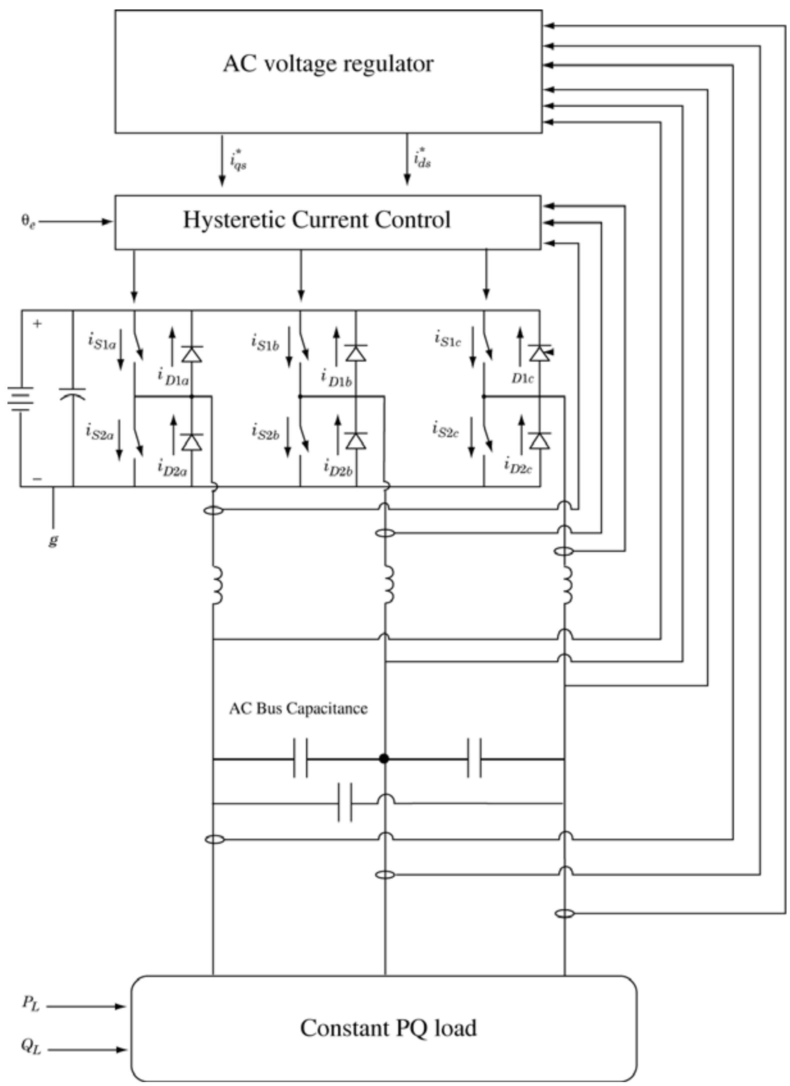

Figure 3-11 Inverter with regulated output voltage.

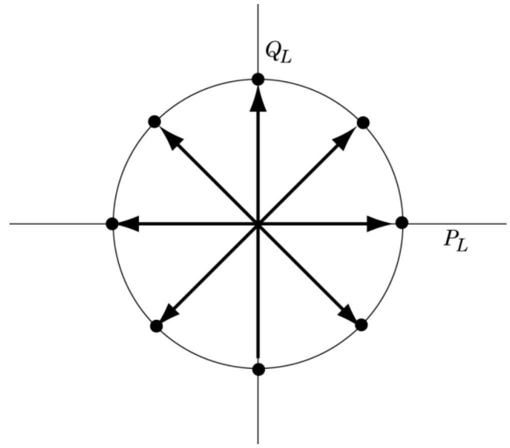

Figure 3-12 Allowable step changes in load real/reactive power.

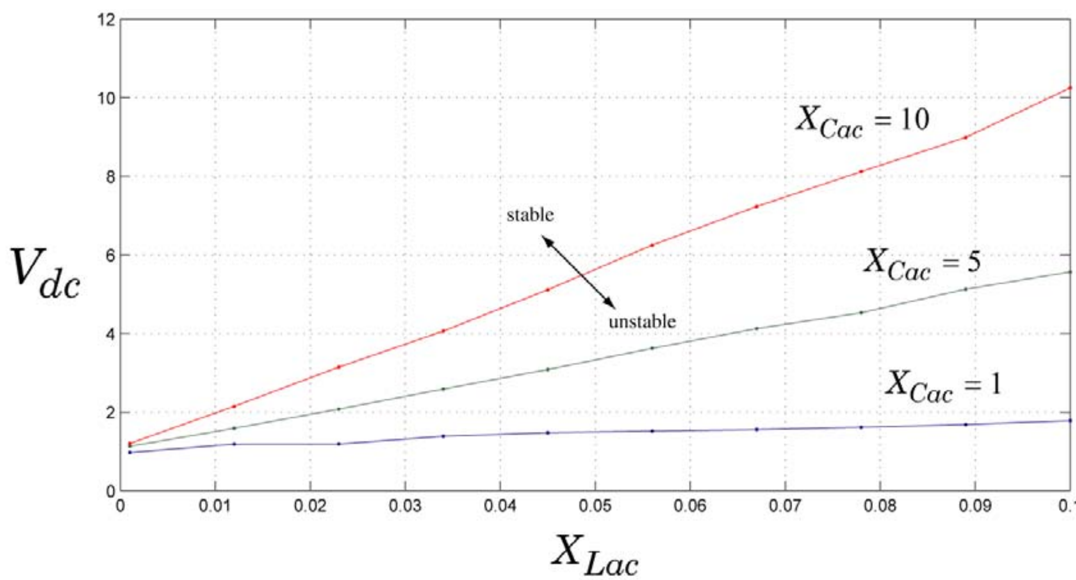

Figure 3-13 Stability boundary.

The preceding results indicate that it is indeed possible to select parameters that guarantee large-disturbance stability. However, it does not answer the question as to whether the parameters are practicable. To address the second question, the detailed model was used to establish the switching frequency and switching losses at selected points along the family of boundaries in Figure 3-14. In calculating the losses, it is assumed that the transistor turn-on and turn-off times are both 1 μs and the conduction drop is 2 V (with a base or rated voltage of 400 V). Switching losses are approximated as

$$E_{\text{turn-off}} = \frac{1}{2} V_{dc} I_o t_{\text{turn-off}} \tag{3.12}$$

$$E_{\text{turn-on}} = \frac{1}{2} V_{dc} I_o t_{\text{turn-on}} \tag{3.13}$$

where I_o is the transistor current at the instant of turn-on or turn-off. The calculated losses at the stability boundary are plotted in Figure 3-14. As shown for a capacitive reactance of $X_{Cac} = 5\,\text{pu}$, the inverter losses have a minimum of approximately 0.054 pu (5.4%) with an inductive reactance of $X_{Lac} = 0.0125\,\text{pu}$ and dc voltage of $V_{dc} = 1.75\,\text{pu}$. These values are all within a practicable range. An example time-domain study for a step change in real load power from -1 (full regeneration) to +1 (full load) is depicted in Figure 3-15. As shown, the system is stable for this extreme change in loading conditions.

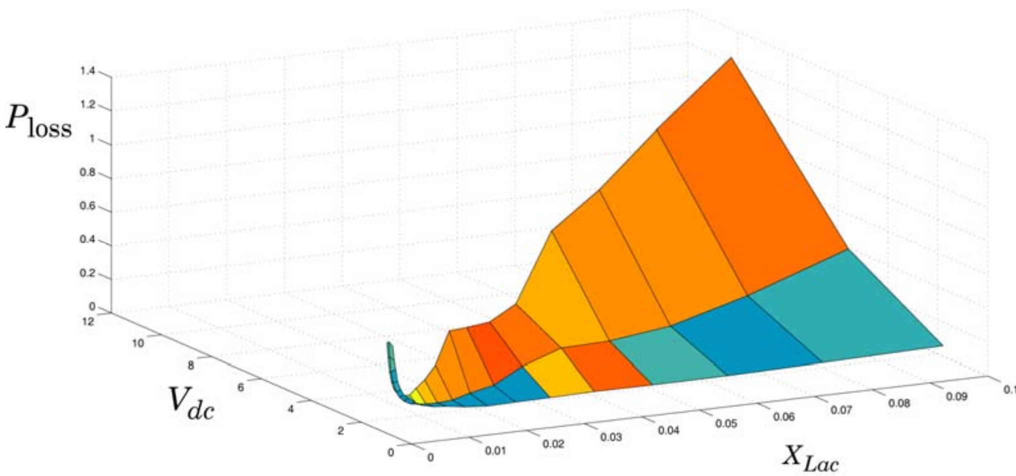

Figure 3-14 Inverter losses at boundary of stability.

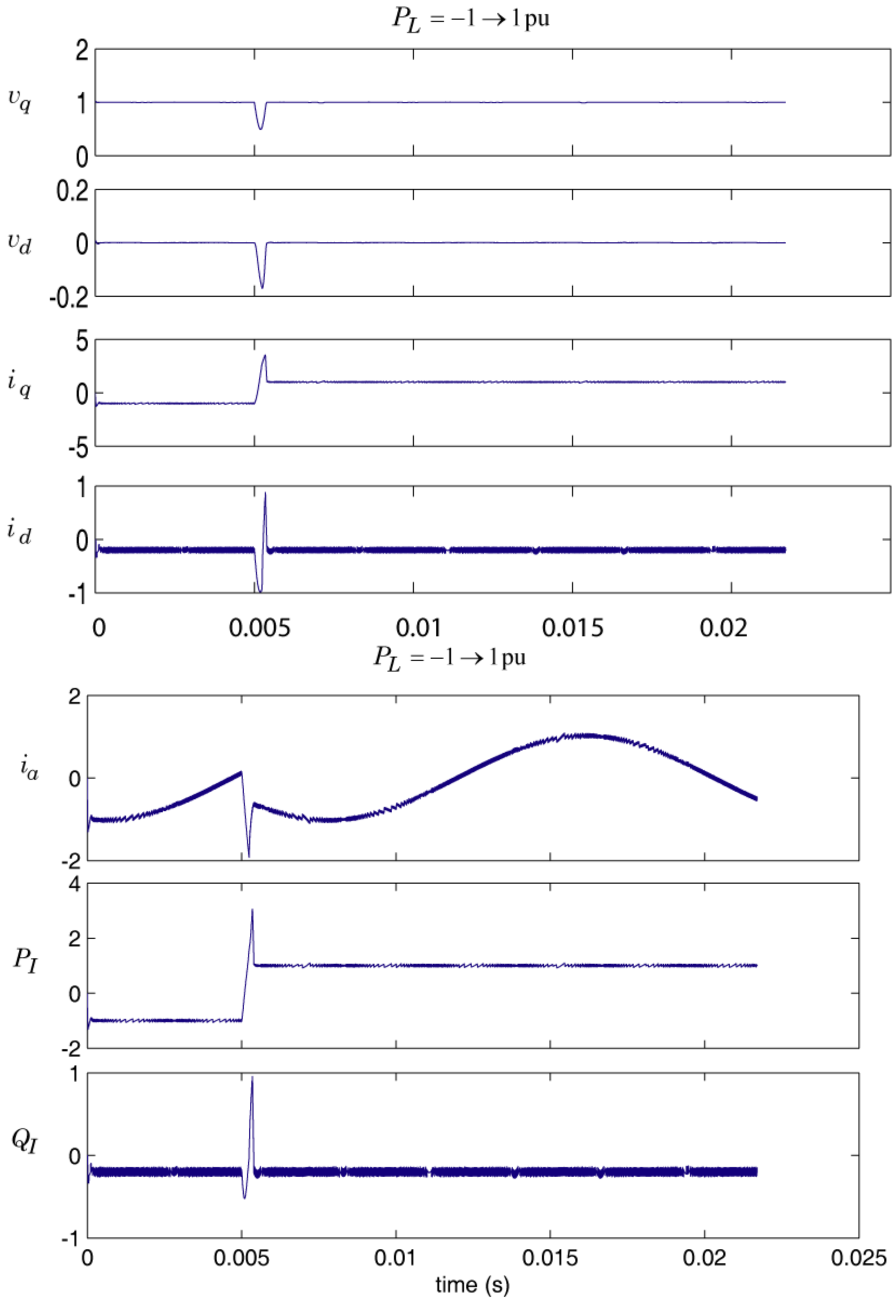

Figure 3-15 Example study for step change in real power from -1 to 1 pu.

3.2 Power Quality

Although there does not exist a universally accepted and strict definition of power quality in ac systems, the attributes of a system that are associated with power quality include: continuity of service, variations in voltage magnitude and frequency, allowable transient voltages and currents, harmonic content in the waveforms for voltage and/or power. Allowable variations in voltage may be specified in the form of a magnitude versus time plot such as that shown in Figure 3-16, which is a part of MIL-STD-704F for aircraft electric power systems.

A large harmonic content in voltages may lead to excessive losses (heating) in certain components, electromagnetic (radio) interference, and possible control-related dysfunctions. Allowable harmonic content for aircraft dc systems is shown in Figure 3-17.

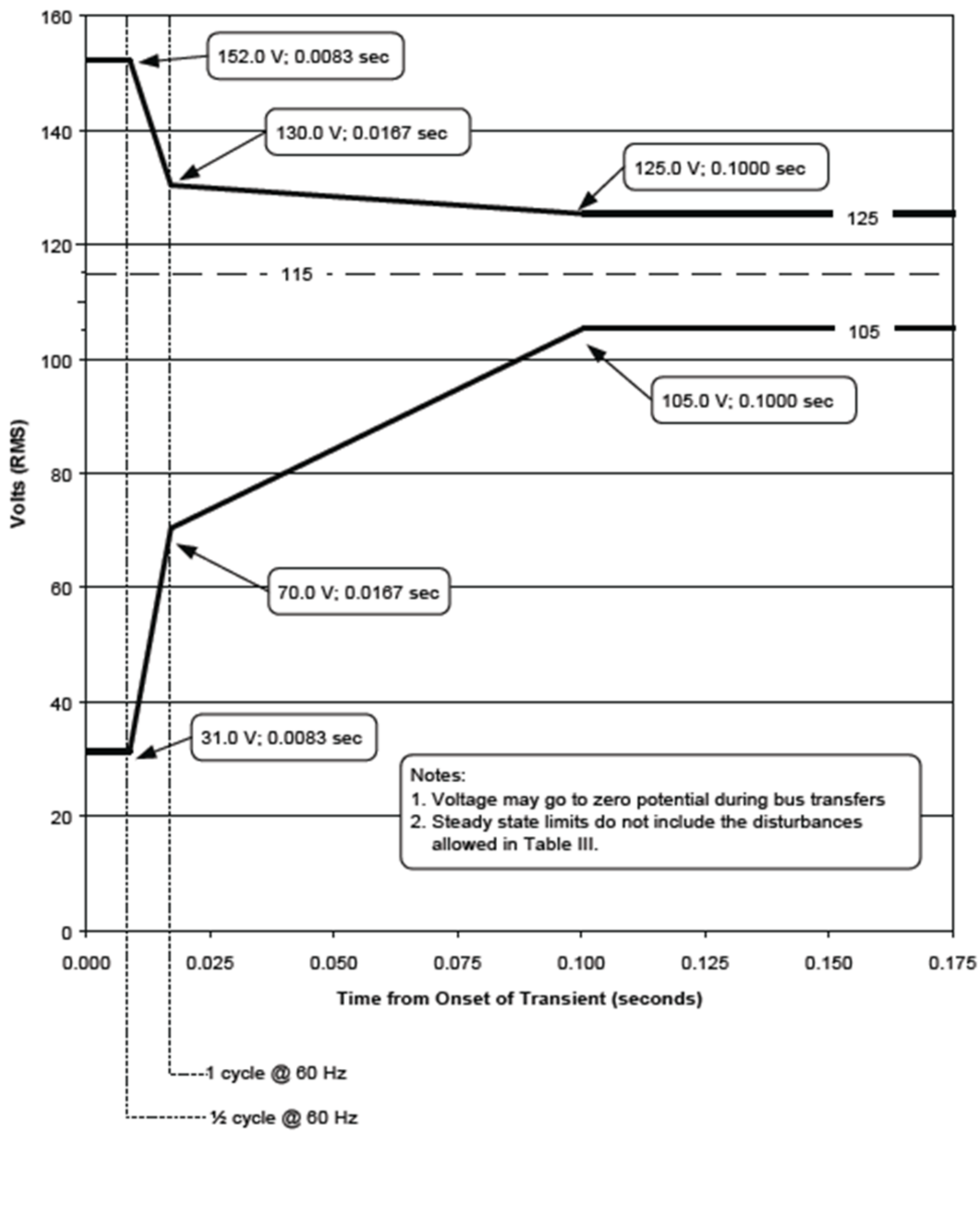

Figure 3-16 Allowable envelope for ac voltage transients [9].

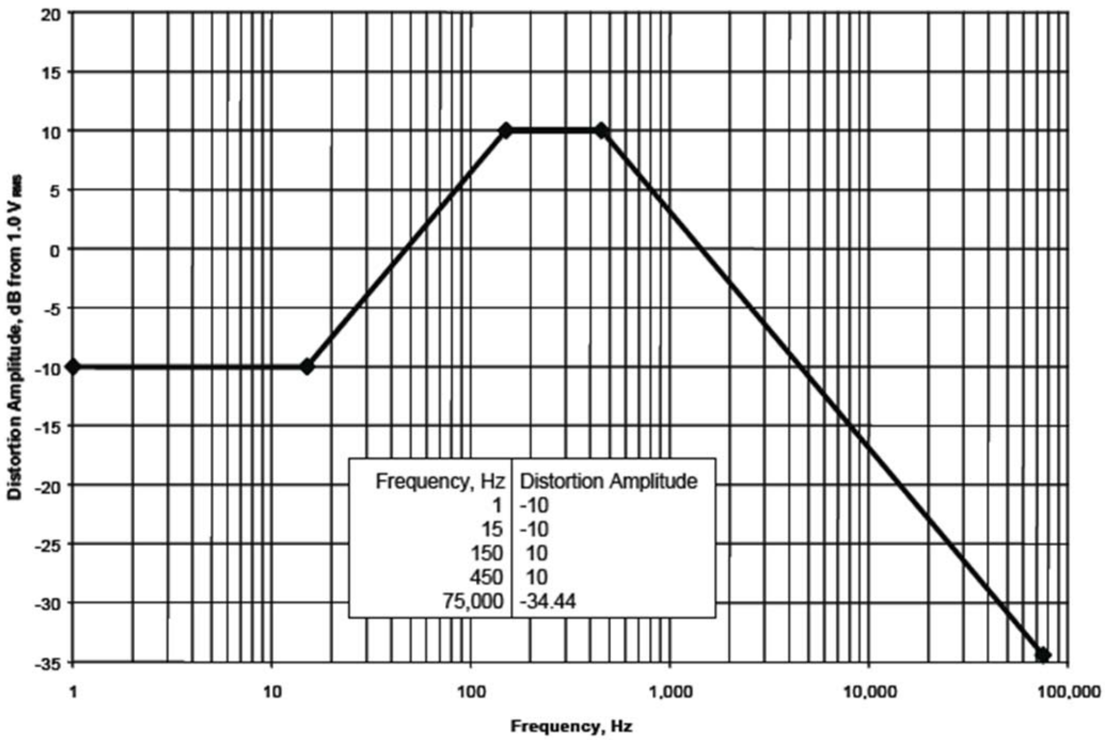

Figure 3-17 Maximum distortion spectrum for ac voltage [9].

3.3 Protection

As noted in a previous section, the protection of ac systems is somewhat less problematic than in dc systems due to the widespread availability of ac circuit breakers. However, it is important that the trip settings of the circuit breakers are coordinated so that when a fault occurs, it can be isolated with minimum impact on the remainder of the system. If, in a stiffly interconnected ac microgrid, the fault occurs on the ac bus or PCC, the given microgrid will experience a complete blackout. However, if the fault is internal to one of the components (on the component side of the circuit breaker or interrupting device), it is important that only the circuit breaker associated with that component is opened so that the remainder of the microgrid can continue operation. To make sure that only the appropriate breaker is opened, it is necessary to identify the location of the fault or unruly component. This is more readily accomplished at the system level suggesting another important role for the PEMS (i.e. protective device coordination) and corresponding need for on Open Architecture Framework to facilitate communication between the microgrid components and the PEMS.

Appendix A

Transmission-Line Modeling

In this appendix, computer representations of dc or single-phase ac transmission lines are developed suitable for predicting high-frequency switching transients. These models can be combined with dynamic representations of other power system components (e.g. rotating machines, solid-state power converters) for the purpose of evaluating switching events such as opening or closing of conventional or solid-state contactors [26], [27]. Additionally, reduced-order models are presented that are computationally more efficient for studying longer-term dynamics or control-system-related issues.

Single-Phase Transmission Line Equations

Consider a single-phase transmission line with a series inductance of L Henrys/meter, a series resistance of R ohms/meter, a shunt capacitance of C Farads/meter and a shunt conductance of G mhos/meter. The equivalent circuit of a differential section of the line is depicted in Fig. A-1.

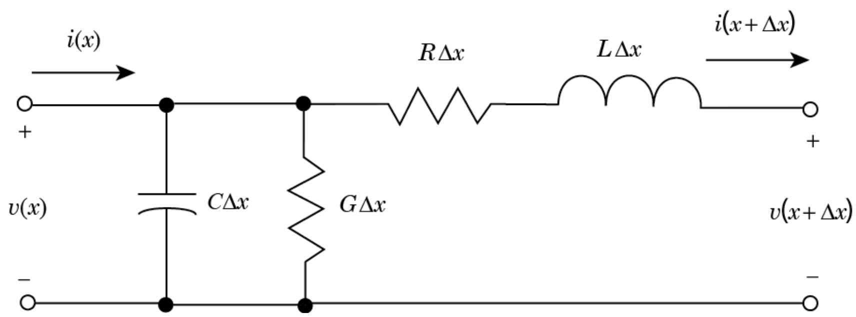

Figure A-1 Equivalent circuit of a differential section of a dc or single-phase ac transmission line.

From Kirchoff's voltage law,

$$v\left(x+\Delta x,t\right)-v\left(x,t\right)=-\left(L\Delta x\right)\frac{d}{dt}i\left(x+\Delta x,t\right)-\left(R\Delta x\right)i\left(x+\Delta x,t\right) \qquad \text{(A.1)}$$

Dividing by Δx

$$\frac{v\left(x+\Delta x,t\right)-v\left(x,t\right)}{\Delta x}=-L\frac{d}{dt}i\left(x+\Delta x,t\right)-Ri\left(x+\Delta x,t\right) \tag{A.2}$$

As Δx approaches zero, the left side of (A.2) approaches $\dfrac{\partial v\left(x,t\right)}{\partial x}$. Moreover $i\left(x+\Delta x,t\right)$ approaches $i\left(x,t\right)$. Taking the limit of both sides of (A.2) as Δx approaches zero,

$$\frac{\partial}{\partial z}v\left(x,t\right)=-Ri\left(x,t\right)-L\frac{\partial}{\partial t}i\left(x,t\right) \tag{A.3}$$

Similarly,

$$\frac{\partial}{\partial z}i\left(x,t\right)=-Gv\left(x,t\right)-C\frac{\partial}{\partial t}v\left(x,t\right) \tag{A.4}$$

The preceding equations represent two coupled, first-order, linear partial differential equations. In order to establish $v\left(x,t\right)$ and $i\left(x,t\right)$ from these equations, we require additional information which can be given in one of several forms. In particular, we may be given $v\left(x,t\right)$ at the two ends of the line. Alternatively, we may be given $i\left(x,t\right)$ at both ends of the line or we may be given $i\left(x,t\right)$ at one end and $v\left(x,t\right)$ at the other end. These define the so-called boundary conditions. Possible boundary conditions are depicted in Fig. A-2. Therein, it is assumed that $v_L(t)=v(0,t)$ [$i_L(t)=i(0,t)$] is the voltage [current] on the left-hand side of the transmission line and $v_R(t)=v(d,t)$ [$i_R(t)=i(d,t)$] is the voltage [current] on the right-hand side. Here, d is the physical length of the line. In addition to the boundary conditions, we also require knowledge of the initial voltage and current distribution, i.e. $v\left(x,0\right)$ and $i\left(x,0\right)$. These are the so-called initial conditions. Given the initial and boundary conditions, (A.3)-(A.4) may be solved for the voltage and current distribution for $t>0$.

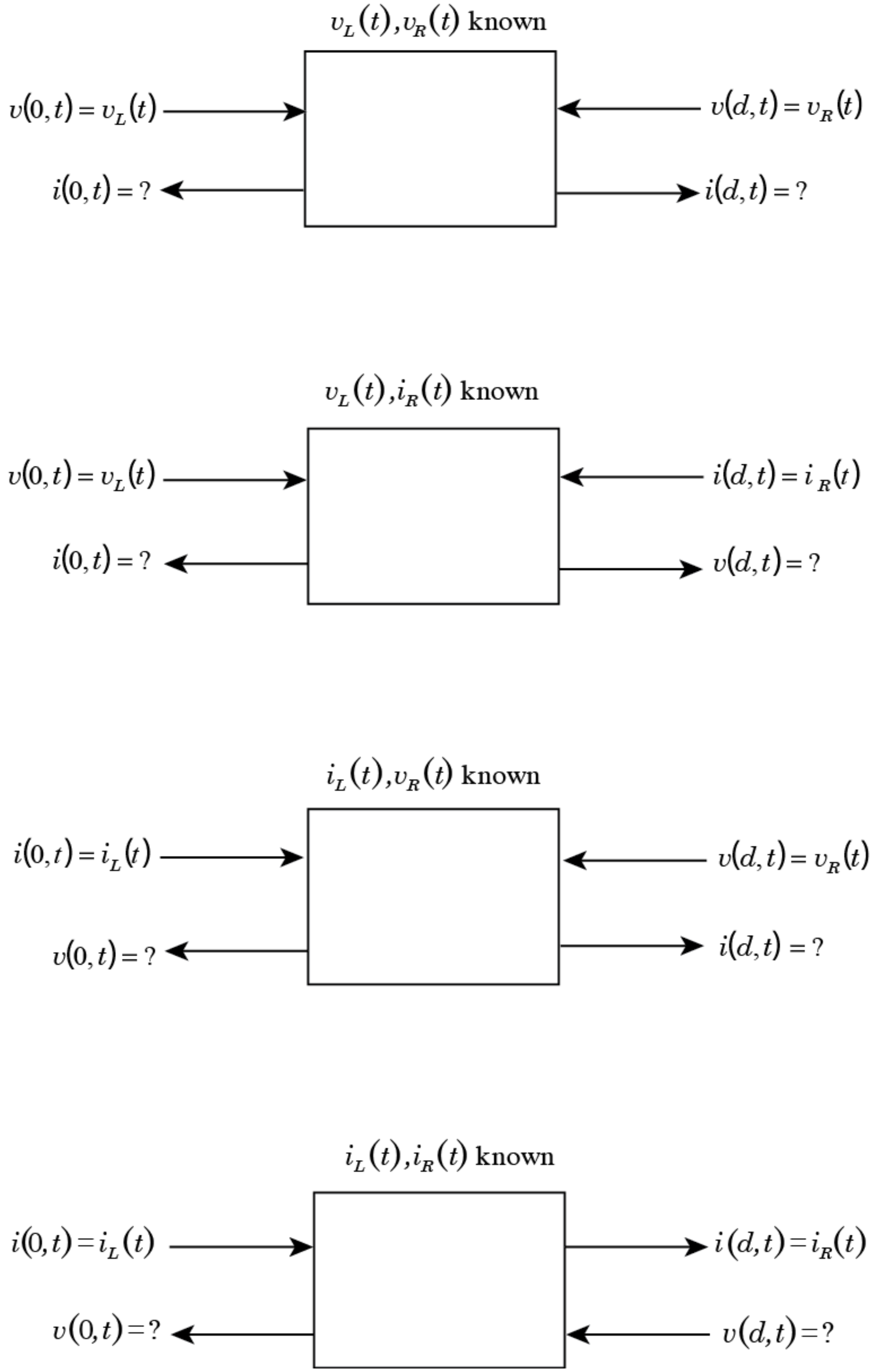

Figure A-2 Possible boundary conditions.

Solution of the Long-Line Equations

In order to solve the preceding set of partial differential equations, it is convenient to transform $v\left(x,t\right)$ and $i\left(x,t\right)$ into the frequency domain using the familiar Fourier transform. In particular

$$v\left(x,\omega\right)=\int_{-\infty}^{\infty} v\left(x,t\right)e^{-j\omega t}dt=\Im\left\{v\left(x,t\right)\right\} \tag{A.5}$$

Similarly, we define

$$i\left(x,\omega\right)=\Im\left\{i\left(x,t\right)\right\} \tag{A.6}$$

In the frequency domain, (A.3) and (A.4) may be expressed

$$\frac{d}{dx}v\left(x,\omega\right)=-Ri\left(x,\omega\right)-j\omega Li\left(x,\omega\right) \tag{A.7}$$

$$\frac{d}{dx}i\left(x,\omega\right)=-Gv\left(x,w\right)-j\omega Cv\left(x,\omega\right) \tag{A.8}$$

Equivalently,

$$\frac{d}{dx}v\left(x,\omega\right)=-Z\left(\omega\right)i\left(x,\omega\right) \tag{A.9}$$

$$\frac{d}{dx}i\left(x,\omega\right)=-Y\left(\omega\right)v\left(x,\omega\right) \tag{A.10}$$

where

$$Z\left(\omega\right)=R+j\omega L \tag{A.11}$$

$$Y\left(\omega\right)=G+j\omega C \tag{A.12}$$

It is possible to eliminate $i\left(x,\omega\right)$ from (A.9) by differentiating both sides with respect to x and substituting $-Y\left(\omega\right)v\left(x,\omega\right)$ for $\frac{d}{dx}i\left(x,w\right)$, i.e.

$$\frac{d^2}{dx^2}v(x,\omega)=Z(\omega)Y(\omega)v(x,\omega) \tag{A.13}$$

If ω is interpreted as a fixed parameter (instead of an independent variable), the preceding equation becomes a second-order, linear, ordinary differential equation. A similar equation can be established in terms of $i(z,\omega)$. In particular,

$$\frac{d^2}{dx^2} i\left(x,\omega\right) = Y\left(\omega\right) Z\left(\omega\right) i\left(x,\omega\right) \tag{A.14}$$

It is convenient to define $\gamma = \sqrt{Z(\omega)Y(\omega)}$ whereupon (A.13) and (A.14) become

$$\frac{d^2}{dx^2} v\left(x,\omega\right) = \gamma^2 v\left(x,\omega\right) \tag{A.15}$$

$$\frac{d^2}{dx^2} i\left(x,\omega\right) = \gamma^2 i\left(x,\omega\right) \tag{A.16}$$

If it can be assumed that $LG = RC$, then γ can be expressed as

$$\gamma = \alpha + j\omega\beta \tag{A.17}$$

where

$$\beta = \sqrt{LC} \tag{A.18}$$

and

$$\alpha = \sqrt{RG} \tag{A.19}$$

The variable γ is commonly called the propagation constant. The assumption that $LG = RC$ is not made for justifiable physical reasons. Instead, it is made to simplify the structure of the resulting model. Specifically, we can then express the general solution to (A.15) as

$$v\left(x,\omega\right) = v^+\left(x,\omega\right) + v^-\left(x,\omega\right) \tag{A.20}$$

where

$$v^+\left(x,\omega\right) = e^{-\gamma x} v^+\left(x_o,\omega\right) \tag{A.21}$$

and

$$v^-\left(x,\omega\right) = e^{\gamma x} v^-\left(x_o,\omega\right) \tag{A.22}$$

For reasons to be discussed v^{+} is called incident component of voltage and v^{-} is called the reflected component. The fact that (A.20)-(A.22) are a legitimate solution of (2.11) can readily be verified by differentiating (A.21)-(A.22) twice with respect to x and comparing the sum with the right-hand side of (A.15). Likewise, we can express

$$i\left(x,\omega\right)=i^{+}\left(x,\omega\right)+i^{-}\left(x,\omega\right) \tag{A.23}$$

where

$$i^{+}\left(x,\omega\right)=e^{-\gamma x}i^{+}\left(x_{o},\omega\right) \tag{A.24}$$

and

$$i^{-}\left(x,\omega\right)=e^{\gamma x}i^{-}\left(x_{o},\omega\right) \tag{A.25}$$

Consider the incident (+) component with x_{o} set to 0.

$$v^{+}\left(x,\omega\right)=e^{-\left(\alpha+j\omega\beta\right)x}v^{+}\left(0,\omega\right)=e^{-\alpha x}\left[e^{-j\omega\beta x}v^{+}\left(0,\omega\right)\right] \tag{A.26}$$

It is readily recognized that the term inside the square bracket represents the Fourier transform of $v^{+}\left(0,t\right)$ delayed by βx seconds. Thus, $v\left(x,t\right)$, which represents the voltage at a distance x from the selected origin, will be equal to the voltage at the origin at a previous instant of time $\left(t-\beta x\right)$ sec and attenuated by $e^{-\alpha x}$. Therefore, v^{+} can be associated with a traveling wave. The exponential term $e^{-\alpha x}$ represents the attenuation of the wave as it propagates in the direction of increasing x. Similarly, $v^{-}\left(x,\omega\right)$ can be associated with a traveling wave that propagates in the opposite direction. Thus, α may be viewed as an attenuation constant and β as a phase or time-delay constant.

Alternative Solution of the Transmission Line Equations

The solution of the transmission line equations given in (A.26) is particularly useful of interpreting the general nature of the propagation of signals within the transmission line. However, the boundary conditions are more conveniently incorporated by considering an alternative form of the general solution. In particular, let us reconsider (A.9)

$$\frac{d}{dx}v(x,\omega) = -Z(\omega)i(x,\omega) \tag{A.27}$$

Substituting (A.19)-(A.21) into the previous equation gives

$$\frac{dv}{dx} = -Ze^{-\gamma x}i^{+}(x_o,\omega) - Ze^{\gamma x}i^{-}(x_0,\omega) \tag{A.28}$$

Integrating with respect to *z* gives

$$v(x,\omega) = Z_c e^{-\gamma x}i^{+}(x_0,\omega) - Z_c e^{\gamma x}i^{-}(x_0,\omega) \tag{A.29}$$

where

$$Z_c = Z\gamma^{-1} \tag{A.30}$$

is the characteristic impedance. If losses (R and/or G) and included, or if frequency-dependence of parameters are considered, Z_c will vary as a function of frequency. However, if losses are neglected and it is assumed that L and C are independent of frequency, Z_c will be a constant and real and is commonly called the surge impedance.

Boundary Relationships

Suppose reference directions for the voltage and current at the two ends of a single-phase line are a depicted in Fig. A-1. Suppose we take $x_0 = 0$ at the left end of the line with *x* decreasing to the left. In general,

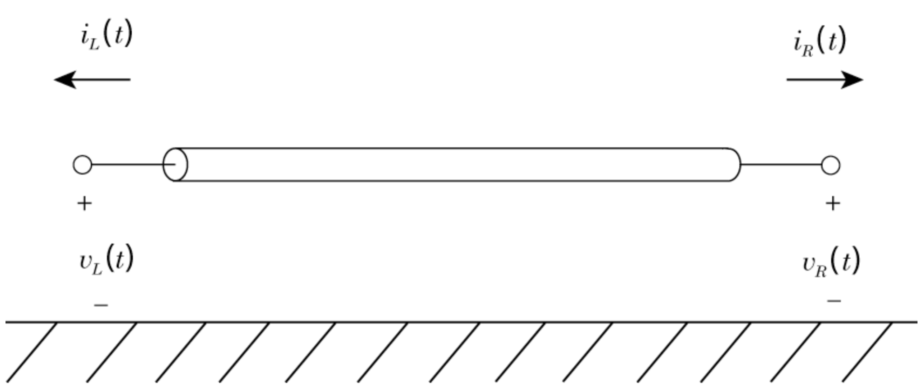

Figure A-3 Voltage and current reference directions.

$$v(x,\omega) = e^{-\gamma x} v^{+}(x_0,\omega) + e^{\gamma x} v^{-}(x_0,\omega) \tag{A.31}$$

For $x = 0$ and with $x_0 = 0$,

$$v(0,\omega) = v^{+}(0,\omega) + v^{-}(0,\omega) \tag{A.32}$$

Letting $v_L(\omega)$ denote $v(0,\omega)$ and expressing the previous equation in the time domain

$$v_L(t) = v_L^{+}(t) + v_L^{-}(t) \tag{A.33}$$

Similarly,

$$i_L(t) = i_L^{+}(t) + i_L^{-} \tag{A.34}$$

Now, from (A.29),

$$v(x,\omega) = Z_c e^{-\gamma x} i^{+}(x_0,\omega) - Z_c e^{\gamma x} i^{-}(x_0,\omega) \tag{A.35}$$

At $x = 0$ with $x_0 = 0$

$$v(0,\omega) = Z_c i^{+}(0,\omega) - Z_c i^{-}(0,\omega) \tag{A.36}$$

Letting $i_L(\omega)$ denote $i(0,\omega)$ and expressing the previous equation in the time domain.

$$v_L(t) = Z_c i_L^{+}(t) - Z_c i_L^{-}(t) \tag{A.37}$$

Solving for i_L^{-},

$$i_L^{-}(t) = -Z_c^{-1} v_L(t) + i_L^{+}(t) \tag{A.38}$$

Substituting (A.38) into (A.34) gives

$$i_L(t) = 2i_L^+(t) - Z_c^{-1}v_L(t) \tag{A.39}$$

Equation (A.38) relates the reflected component of current to the incident component of current and the voltage at the left end of the line. Equation (A.39) gives the total current flowing out of the left end in terms of the incident component of current and the voltage $v_L(t)$. It is important to observe that we have expressed the reflected component of current in terms of the incident component without having to define the reflection coefficient that, in general, is difficult to do unless the line is terminated with a fixed impedance.

Similar equations for the right=hand side of the line may be derived by selecting $x = 0$ at the right-hand side with x decreasing as we move left. In this case,

$$i_R^-(t) = -Z_c^{-1}v_R(t) + i_R^+(t) \tag{A.40}$$

$$i_R(t) = 2i_R^+ - Z_c^- v_R^{-1}(t) \tag{A.41}$$

It is important to observe that on the left side of the line the + or incident component corresponds to a left-going wave and on the right side, the incident component corresponds to a right-going wave. With this in mind, it follows that

$$i_L^+(\omega) = -e^{-\gamma d} i_R^-(\omega) \tag{A.42}$$

where $i_L^+(\omega)$ represents the incident component on the left side and $i_R^-(\omega)$ represents the reflected component on the right and d is the line length. Similarly,

$$i_R^+(\omega) = -e^{-\gamma d} i_L^-(\omega) \tag{A.43}$$

A block diagram of the transmission line dynamic representation is given in Fig. A-4. Therein, it should be noted that although $e^{-\gamma d}$ represents a frequency-domain operator, it would be implemented as a cascade connection of a pure time delay followed by appropriate attenuation. For example, $i_L^+ = -e^{-\gamma d} i_R^-$ would be implemented as

$$i_L^+(t) = -e^{-\alpha d} i_L^-(t - \tau) \tag{A.44}$$

where $\tau = \beta d$ is the propagation time of the transmission line. The time delay, in turn, can be implemented using a digital queue. Popular simulation tools such as Simulink include time-delay functions as part of their standard library of components. The remaining blocks in Fig. A-4 are algebraic. In Fig. A-4, it is assumed that the voltages on the left- and right-hand sides of the line are inputs while the currents are outputs. As noted earlier, other potential boundary conditions are possible. Using derivations similar to those given above, long-line models for the other potential boundary conditions may be established and are given in Figs. A-5 through A-7.

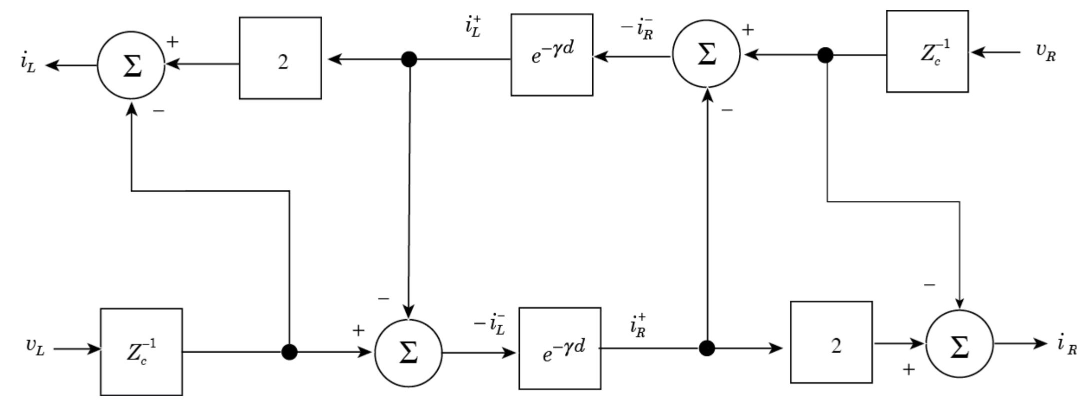

Figure A-4 Simulation block diagram with sending and receiving voltages as inputs.

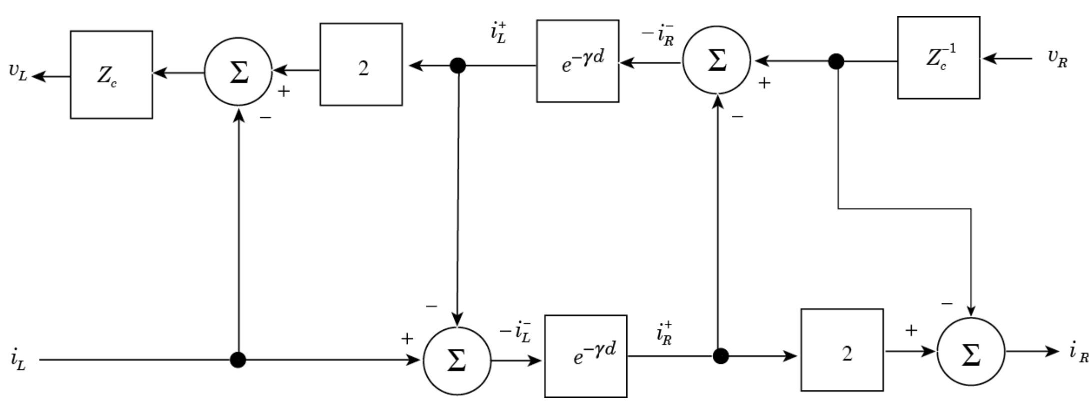

Figure A-5 Simulation block diagram with left-end current and right-end voltage as inputs.

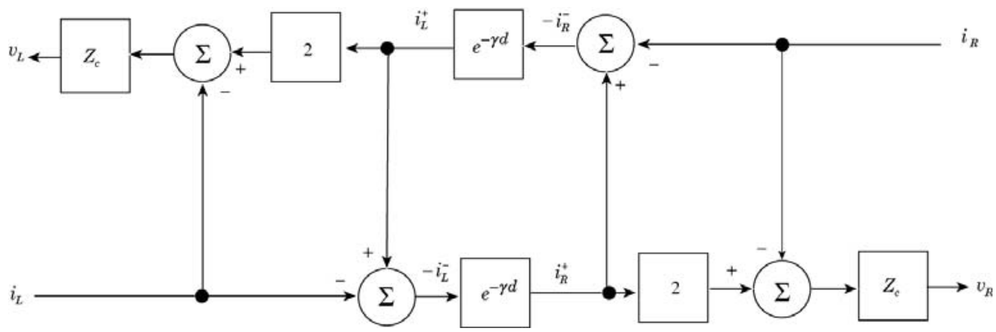

Figure A-6 Simulation block diagram with left- and right-end current as inputs.

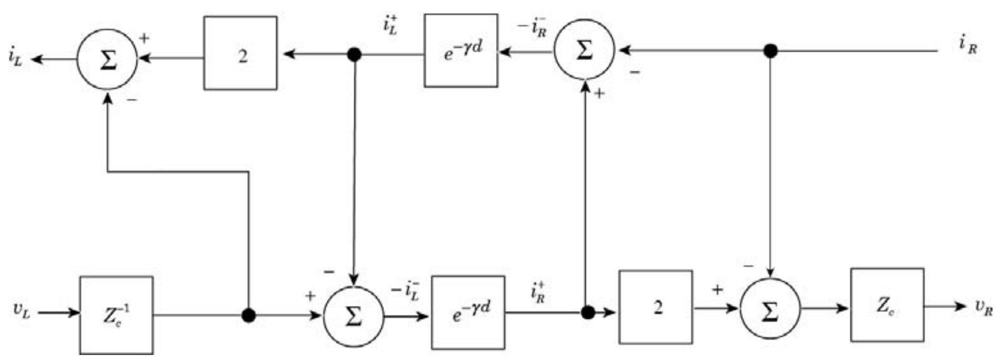

Figure A-7 Simulation block diagram with left-end voltage and right-end current as inputs.

It is worthwhile to review briefly the assumptions that were made in the derivation of these models. First, it was assumed that L and C are independent of frequency and that $LG = RC$. Under these assumptions, the solution of the transmission-line equations may be expressed in terms of a pair of left- and right-going traveling waves that travel at a constant velocity of $1/\sqrt{LC}$ and are attenuated by $e^{-\alpha d}$ (d = line length) as they propagate from one end of the line to the other. This approach is reasonable as long as the losses are small to begin with and provided that we are interested in a range of frequencies close to that which was assumed when calculating L and C. We can certainly establish a model that predicts which higher accuracy the behavior of the line over a wider range of frequencies by allowing parameters to vary as a function of frequency and removing the assumption of distortionless transmission ($LG = RC$). In the most general case, Z_c will vary with frequency and $e^{-\gamma d}$ cannot be implemented using a simple time-delay with attenuation. Rather, we must synthesize a set of state equations that are made to fit the calculated Z_c and $e^{-\gamma d}$ in the frequency domain [???].

Short-Line Modeling

The long-line models described in the previous sections are computationally efficient in the sense that only a few algebraic calculations are required per time step. Moreover, the time delay operator is easily implemented using a digital queue. However, they are not conducive to the study of long-term dynamics or simulation of short transmission lines since the time step must be smaller than the propagation time of the shortest line in the system. As an example, the propagation time for a 1-mile line is approximately $5.4\,\mu\text{s}$, which represents the maximum time step that can be taken when solving for the overall system response even after fast transients subside. For shorter lines, the maximum time step is proportionately smaller. Consequently, if longer-term transients are of interest or if the system contains an electrically short short line, it is desirable to replace the time-delay operator with a transfer-function such as the Padé approximant. The first-order Padé approximant of the frequency-domain time-delay operator $e^{-j\omega\tau}$ is given as

$$e^{-j\omega\tau} \approx \frac{1}{1+j\omega\tau} \tag{A.45}$$

which is accurate for $\omega\tau \ll 1$. If, for example, the propagation time $\tau = 5.4\,\mu\text{s}$, the Padé approximant is accurate for signals whose maximum frequency is sufficiently less than 60 kHz.

The main advantage of the first-order Padé approximant is that it can be implemented using the state-space model

$$\begin{aligned} \tau\frac{dx}{dt} &= -x+u \\ y &= x \end{aligned} \tag{A.46}$$

Even if the propagation time τ is small, the time step is not restricted to values smaller than τ and can be much larger provided that a stiffly-stable integration algorithm is used in the numerical solution of the state equations. The use of a Padé approximant for the time-delay operator is a relatively straightforward modification of the long-line models given in Figs. A-4 through A-7.

Another approach of modeling an electrically short transmission line is to use a lumped-parameter equivalent-circuit representation. In order to develop a lumped-parameter equivalent circuit, it is useful to reconsider (A.13) and (A.14), repeated here for convenience.

$$\frac{d^2}{dx^2}v(x,\omega) = Z(\omega)Y(\omega)v(x,\omega) \tag{A.47}$$

$$\frac{d^2}{dx^2}i(x,\omega) = Y(\omega)Z(\omega)i(x,\omega) \tag{A.48}$$

The solutions of these second-order ordinary differential equations may be expressed in the frequency domain as

$$v(x,\omega) = A_1 e^{\gamma x} + A_2 e^{-\gamma x} \tag{A.49}$$

$$i(x,\omega) = -\frac{A_1}{Z_c}e^{\gamma x} + \frac{A_2}{Z_c}e^{-\gamma x} \tag{A.50}$$

where

$$\gamma = \sqrt{YZ} \tag{A.51}$$

and

$$Z_c = \sqrt{\frac{Z}{Y}} \tag{A.52}$$

Defining

$$\cosh x = \frac{e^x + e^{-x}}{2} \tag{A.53}$$

and

$$\sinh x = \frac{e^x - e^{-x}}{2} \tag{A.54}$$

then the solutions to (A.49) and (A.50) may be expressed in equivalent forms

$$v(x,\omega) = v_L(\omega)\cosh\gamma x - i_L(\omega)Z_c \sinh\gamma x \tag{A.55}$$

$$i(x,\omega) = i_L(\omega)\cosh\gamma x - \frac{v_L(\omega)}{Z_c}\sinh\gamma x \tag{A.56}$$

Letting $x = d$,

$$v_R(\omega) = v_L(\omega)\cosh\gamma d - i_L(\omega)Z_c\sinh\gamma d \tag{A.57}$$

$$i_R(\omega) = i_L(\omega)\cosh\gamma d - \frac{v_L(\omega)}{Z_c}\sinh\gamma d \tag{A.58}$$

Equations (A.57) and (A.58) may also be deduced from the equivalent π circuit depicted in Fig. A-8.

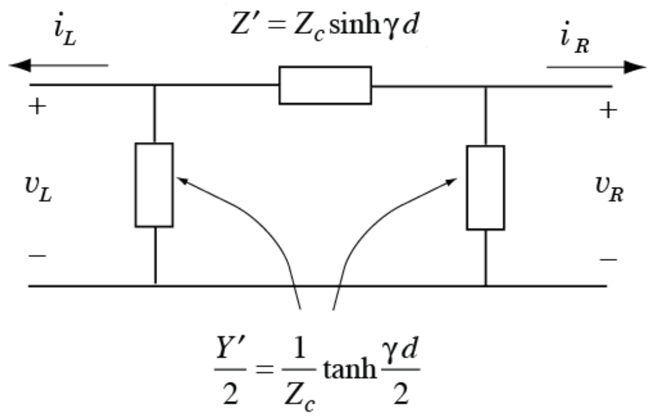

Fig. A-8 Equivalent π circuit of dc or single-phase ac transmission line.

A transmission line is considered electrically short if

$$|\gamma d| \ll 1 \tag{A.59}$$

If, momentarily, losses are neglected ($R = G = 0$), then

$$\sinh\gamma d \approx \gamma d \approx j\omega\sqrt{LC}d \approx j\omega\tau \tag{A.60}$$

where $\tau = d\sqrt{LC}$ is the propagation time of the transmission line. Additionally,

$$\tanh\frac{\gamma d}{2} \approx \frac{\gamma d}{2} \approx \frac{j\omega\tau}{2} \tag{A.61}$$

Thus, under the previous assumptions, Fig. A-8 can be approximated as shown in Fig. A-9 where

$$L_\pi = \tau Z_c \tag{A.62}$$

and

$$C_{\pi} = \tau Z_c^{-1} \tag{A.63}$$

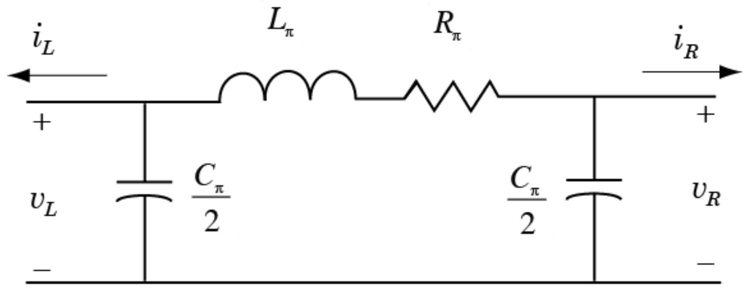

Figure A-9 Equivalent π circuit of electrically short transmission line.

In Fig. A-9, the series resistance $R_{\pi} = Rd$ was reintroduced to approximate the effects of line losses. In the case of a dc line, the series resistance would be taken as its dc value. In an ac line, the ac resistance should be used to account for skin effect.

It is useful to note that the same similar assumptions are made in the derivation of the long-line models with a Padé approximant to the time delay and in the equivalent π circuit of Fig. A-9. A potential advantage of the equivalent π circuit is that the shunt capacitance at one or both ends may be combined with the filter capacitance associated with the power converters that are connected to one or both ends of the line.

In a state-space implementation, the equivalent π circuit accepts currents as inputs and gives voltages as outputs. If the boundary conditions are such that voltages are specified while currents are to be established, the equivalent π circuit may be converted to an equivalent *T* circuit as shown in Fig. A-10. The corresponding state-space implementation accepts voltages as inputs and has currents as outputs. The choice of equivalent *T* or equivalent π circuit depends upon the inputs and outputs of the sources or loads to which the transmission line is connected.

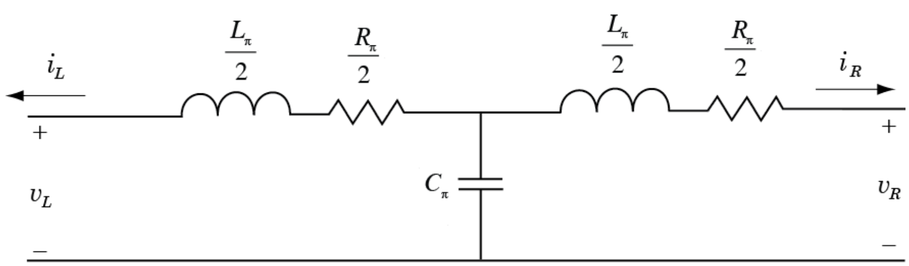

Figure A-10 Equivalent *T* circuit of electrically short transmission line.

Appendix B

Incorporating S-Parameter-Based Models in Power System Simulations

Proposed microgrids rely on power electronics to provide voltage at the levels and frequencies compatible with each load. Switching of power electronic devices introduces electromagnetic fields at wavelengths that will be less than the dimensions of the distribution system. Thus accurately predicting voltage stress on insulation systems, common-mode currents, and exploring the impacts of alternative grounding systems on voltage/common-mode current will likely require some use of distributed-parameter models.

The use of S-parameters is a relatively common means of modeling distributed parameter systems [28]. In an S-parameter model, the signal reflection and transmission of an N-port network is modeled in a form

$$\begin{bmatrix} b_1 \\ b_2 \\ \vdots \\ b_n \end{bmatrix} = \begin{bmatrix} S_{11} & S_{12} & \cdots & S_{1n} \\ S_{21} & S_{22} & \cdots & S_{2n} \\ \vdots & \vdots & \ddots & \vdots \\ S_{n1} & S_{n2} & \cdots & S_{nn} \end{bmatrix} \begin{bmatrix} a_1 \\ a_2 \\ \vdots \\ a_n \end{bmatrix} \tag{B.1}$$

where b_i are outgoing waves that are related to incoming waves a_i using the frequency-dependent coefficients S. Diagonal components S_{ii} are reflection coefficients and off-diagonal components S_{ij} are transmission coefficients. A diagram that is helpful in understanding the S-parameter approach is shown in Fig. B-1.

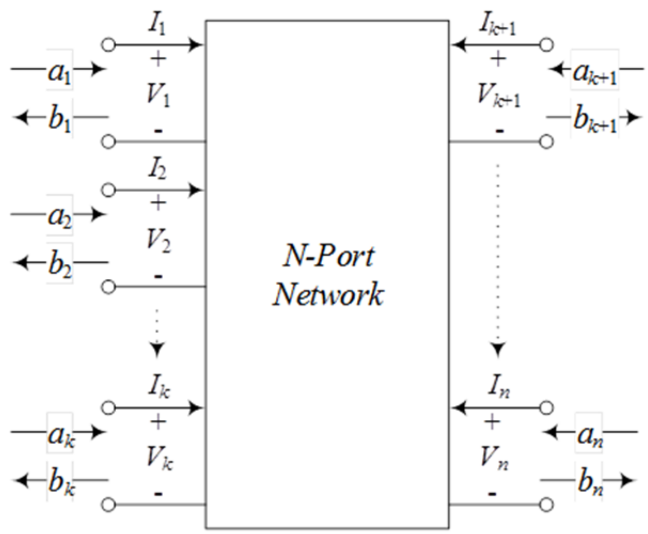

Figure B-1 S-parameter-based characterization.

An advantage of S-parameter-based models over admittance or impedance-based models is a more accurate characterization as frequency increases. Indeed, many wide-bandwidth network analyzers have integrated software/hardware to support S-parameter model development. An advantage of S-parameter-based models over analytical models is that one does not need to make assumptions regarding geometric layout, the ground return path, material properties, etc. A potential disadvantage of S-parameter-based models is that they are characterized in the frequency-domain. Therefore, integration of the models within a traditional time-domain power system simulation requires a conversion. The MATLAB RF toolbox does support this conversion, and indeed, researchers at Florida State have developed tools to automate the process [28].

In this research effort, a goal was to explore the effectiveness of S-parameter based models in time-domain power system simulations using PCKA's ASMG toolbox and the S-parameter tools developed by Florida State. In this effort, Florida State provided S-Parameter data on a 5 kV XLPE Power Cable, documented in [29] and detailed in Table B.1, and a prototype 2-port S-parameter block. Purdue then constructed a Simulink-based model of a DC power system consisting of a Thevenin source, the cable, and a 1 MΩ load. A block diagram of the model is shown in Fig. B-2.

Table B.1 – Power cable Π-model lumped parameters.

Length	26 m
Resistance	42 mΩ
Inductance	1.83 μH
Capacitance	3.17 nF

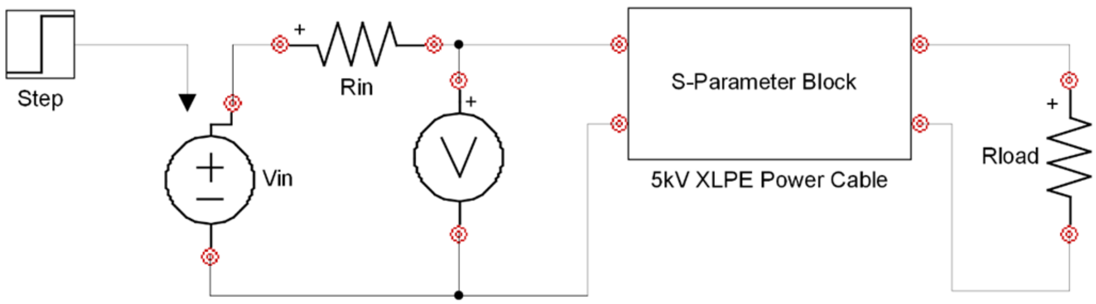

Figure B-2 S-parameter based transmission-line model.

Results of a step change in the source voltage are shown in Fig. B-3. From the response one can see that there is a delay in the time at which the voltage is received at the load, which is expected. However, it is interesting that at the source end, a voltage ripple consistent with a returning reflection is observed at the source at the same instant the voltage wave is received at the load. Upon reviewing the hardware construction, it was found that the cable was constructed by splicing two cables of roughly equal length together, creating a discontinuity at the midpoint of the transmission line. Thus, one would expect to receive a reflected wave at the source at the same instant as that received at the load.

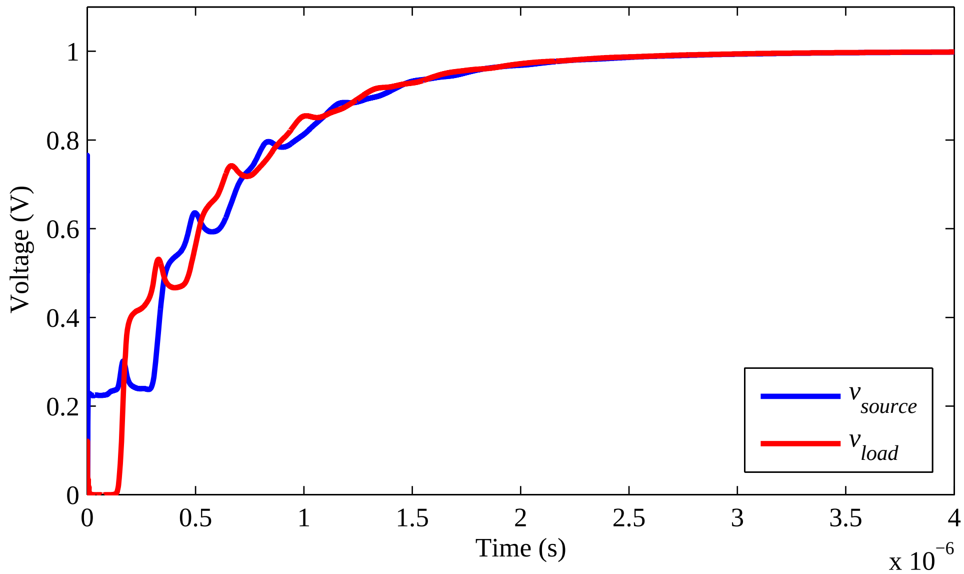

Figure B-3 Predicted voltage at source and load following step input to transmission line.

While this simple study demonstrates the power of S-parameters to readily incorporate the non-idealities of real systems, there are some complications regarding its implementation in power system simulations.

First, the prototype S-parameter block intended for used with circuit-based modeling toolboxes like ASMG or SimPower Systems suffers from numerical problems due to its generality. It was designed to be a simple, drop-in solution for modeling complex, linear systems. However, the generality of its architecture produces algebraic loops that make the block very sensitive to simulation parameters and boundary conditions, possibly precluding convergence altogether. Fortunately, this problem may be circumvented but at the cost of the generality of the modeling approach. Specifically, these algebraic loops are solved through knowledge of the boundary conditions at the S-parameter block interface, which drastically alters the form of the model. Figure B-4 displays the same system as Figure B-2 with algebraic loops eliminated.

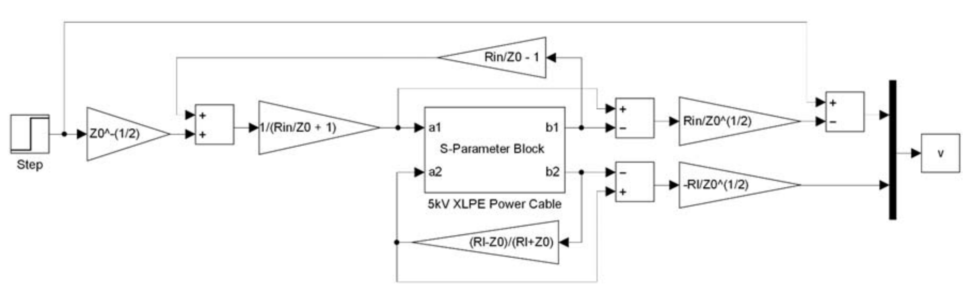

Figure B-4 S-parameter based transmission line model without algebraic loops.

While this second model is more complex, it does not necessarily negate the gains in accuracy provided by the S-parameter characterization approach. When convergence issues preclude the use of the prototype block, it is left to the system designer to determine whether the additional effort in model development is warranted by the desired level of detail.

A second challenge in using S-parameters for time-domain simulation involves the construction of the S-parameter transfer functions from measured data. The proposed method fits the measured S-parameters to a sum of low-order rational transfer functions that may include a direct feed-through term. If this direct feed through-term is included in any of the S-parameter transfer functions, an algebraic loop is created in the heart of the S-parameter model. This loop is an intrinsic feature of the measured S-parameter data. The system designer has some control in preventing the use of the direct feed-through term in the fitting process, but in systems where it is truly appropriate, disallowing it may introduce stiffness, trading one numerical convergence problem for another. For this reason, this second issue is a more serious obstacle to the use of S-parameters in power system simulations.

Taking the benefits and drawbacks together, S-parameter based modeling is a useful tool in the toolbox of the adept designer, but it may not be feasible for use without considerable knowledge on modeling and simulation techniques to break algebraic loops.

References

[1] D. P. Carrol, unpublished notes on DC Power Transmission, 1977.

[2] E. W. Kimbark, A New Look at Shunt Compensation, *IEEE Transactions on Power Apparatus and Systems*, Volume PAS-102, Issue: 1, 1983, pp. 212-218.

[3] J. W. Ballance, S. Goldberg, Subsynchronous Resonance in Series Compensated Transmission Lines, *IEEE Transactions on Power Apparatus and Systems*, Vol. PAS-92, 1973, pp. 1649- 1658.

[4] D. N. Walker C. E. J. Bowler R. L. Jackson, D. A. Hodges, “Result of Subsynchronous Resonance Tests at Mohave,” IEEE Transactions on Power Apparatus and Systems, Vol. PAS-94, Sept. Oct, 1975.

[5] N. G. Hingorani, B. Bhargava, G. F. Garrigue, G. D Rodriguez, “Prototype NGH Subsynchronous Resonance Damping Scheme Part I - Field Installation and Operating Experience,” IEEE Transactions on Power Systems, Vol. 2, 1987.

[6] H. Sugimoto, M. Goto, Kai Wu, Y. Yokomizu, T. Matsumura, “Comparative Studies of Subsynchronous Resonance Damping Schemes,” Proceedings International Conference on Power System Technology (PowerCon), 2002.

[7] B. C. Kuo, **Automatic Control Systems**, Prentice Hall, 1987.

[8] P. C. Krause, O. Wasynczuk, and S. D. Sudhoff, Analysis of Electric Machinery and Drive Systems, IEEE Press, Wiley Interscience, New York, 2002.

[9] MIL-STD-704F, Aircraft Electric Power Characteristics, U.S. Department of Defense, December 2008.

[10] ABB Corporation, Circuit Breakers for Direct Current Applications, Technical Application Paper, September 2007.

[11] Eaton Corporation, Panel Mounting Switches Product Guide IEC 60947-3.

[12] A. G. J. MacFarlane and I. Postlethwaite, “The Generalized Nyquist Stability Criterion And Multivariable Root Loci,” International Journal of Control, Vol. 25, Jan. 1977, pp. 81-127.

[13] B. Noble, J. W. Daniel, **Applied Linear Algebra**, Prentice Hall, 1977.

[14] M. Belkhayat, O. Wasynczuk “Stability Analysis of AC Power Systems with Regulated Electronic Loads,” Aerospace Power Systems Conference, Williamsburg, Virginia, April 21-23, 1998.

[15] B. Loop, N. Wu, "Integrated Simulation of Microgrid Component Models", PC Krause and Associates, status report submitted to Sandia under contract DOE-Sandia-PO1110460, Feb. 11, 2013.

[16] A. Cocconi, S. Cuk, R. D. Misslebrook, T. S. Key, “Design and Development of a 4-kW/20-kHz dc-Isolated Power Conditioner for Utility-Interactive Photovoltaic Applications, pg. 23-26, Sandia SAND87-0353.UC-63, Alburquerque, N.M., September 1987.

[17] Gilbert M. Masters, Renewable and Efficient Electric Power Systems, John Wiley and Sons, 2004, ISBN 0-471-28060-7.

[18] D. C. Aliprantis, S. A. Papathanassiou, M. P. Papadopoulos, and A. G. Kladas, "Modeling and control of a variable-speed wind turbine equipped with permanent magnet synchronous generator," ICEM'2000, Helsinki, Finland, August 2000, pp. 558-562.

[19] U.S. Canada Power System Outage Task Force, "Causes of the August Blackout in the United States and Canada," November 2003.

[20] P. A. Rusche, D. L.Hackett, D. H. Baker, G. E. Gareis, P. C. Krause, "Investigation of the Dynamic Oscillations of the Ludington Pumped Storage Plant," IEEE Transactions on Power Apparatus and Systems, Vol. 95, pp. 1854 - 1862, Nov./Dec. 1976.

[21] A. Engler, N. Soultanis, "Droop control in LV-Grids," Proceedings of the International Conference on Future Power Systems, pp. 6 -18, Nov. 2005.

[22] Energy Development and Power Generating Committee, "IEEE Recommended Practice for Excitation System Models for Power System Stability Studies," IEEE Standard 421.5, 1992.

[23] W. D. Stevenson, Elements of Power System Analysis, McGraw-Hill, New York, 1982.

[24] M. Gries, O. Wasynczuk, B. Selby, P. T. Lamm, "Designing for Large-Displacement Stability in Aircraft Power Systems, SAE Int. J. Aerospace, 2008.

[25] O. Wasynczuk, S. D. Sudhoff, T. D. Tran, P. H. Clayton, and H. J. Hegner, "A Voltage Control Strategy for Current-Regulated PWM Inverters," IEEE Transactions on Power Electronics, Vol. 11, No. 1r, Jan. 1996, pp. 7-15.

[26] P. C. Krause and K. Carlsen, "Analysis and hybrid computer simulation of multiconductor transmission systems," IEEE Transactions on Power Apparatus and Systems, Vol. 91, pp. 469-477, March/April 1972.

[27] H. W. Dommel, "Digital computer solution of electromagnetic transients in single and multiphase networks," IEEE Transactions on Power Apparatus and Systems, Vol. 88, pp. 388-399, April 1969.

[28] M. Kofler, Scattering Parameters for Transient Analysis of Shipboard Power Systems, MSc Thesis, FH Upper Austria, 2013.

[29] L. Graber, D. Infante, M. Steurer, W.W. Brey, "Model Validation for Shipboard Power Cables using Scattering Parameters," Journal of High Voltage Engineering, 37 (11), 2011.

General References

[30] S. D. Sudhoff, K. A. Corzine, S. F. Glover, H. J. Hegner, H. N. Robey, "DC link stabilized field oriented control of electric propulsion systems," IEEE Transactions on Energy Conversion, March 1998.

[31] R. D. Middlebrook, "Input filter considerations in design and application of switching regulators," IEEE Proceedings of IASAM, 1976.

[32] S. D. Sudhoff, S. F. Glover, P. T. Lamm, D. H. Schmucker, D. E. Delisle, "Admittance space stability analysis of power electronic systems," IEEE Transactions on Aerospace and Electronic Systems, 2000.

[33] O. Wasynczuk, L. J. Rashkin, S. D. Pekarek, R. R. Swanson, B. P. Loop, N. Wu, S. F. Glover and J. C. Neely, "Voltage and Frequency Regulation Strategies in Isolated AC Micro-Grids" IEEE International Conference on Cyber Technology in Automation, Control and Intelligent Systems, Bangkok, Thailand, May 27 – May 31, 2012.

[34] S. P. Hoffman, "NERC Interconnected Operations Services Policy Developments Related to Frequency control," Power Engineering Society Winter Power Meeting, pp. 580-583, 1999.

[35] R.H. Lasseter, "MicroGrids," IEEE 2002 Power Engineering Society Winter Meeting, Vol.1, pp. 305- 308, 2002.

[36] N. Hatziargyriou, H. Asano, R. Iravani, and C. Marnay, "MicroGrids: An Overview of Ongoing Research, Development, and Demonstration Projects, IEEE Power and Energy Magazine, July/August 2007.

[37] IEEE Standards Coordinating Committee 21, "IEEE Guide for Design, Operation, and Integration of Distributed Resource Island Systems with Electric Power," Systems, IEEE Standard 1547.4, 2011.

[38] F. Katiraei and M.R. Iravani, "Power Management Strategies for a Microgrid With Multiple Distributed Generation Units," IEEE Transactions on Power Systems, Vol. 21, No.4, pp.1821-1831, Nov. 2006.

[39] N. Jayawarna, X. Wu, Y. Zhang, N. Jenkins, and M. Barnes, "Stability of a MicroGrid," Proceedings of the 3rd IET International Conference on Power Electronics, Machines and Drives, pp. 316-320, Mar. 2006.

Sandia National Laboratories